Nikas, Dimitrios S., Ph.D., October, 2003 NUCLEAR PHYSICS

ULTRA-FAST DETECTION OF RELATIVISTIC CHARGED PARTICLE BEAM BUNCHES USING OPTICAL TECHNIQUES (148 pp.)

Director of Dissertation: Spyridon Margetis

The use of light as a carrier of information has been the subject of discussion for many scientific papers. This approach has some unique features which distinguish it from conventional electronics. These are realized in applications like telecommunications where the use of optical fibers and Electro-Optic sampling is the industry standard.

Electro-Optic sampling employs the "Pockels" or "Electro-Optic" effect. Pockels discovered that an electric field applied to some crystals changes the birefringence properties of the crystal, and hence the polarization of light that propagates through it. By placing the crystal between crossed polarizers, the transmitted light intensity changes as a function of the applied field.

We made the first Electro-Optical (EO) detection of a relativistic charged particle beam, applying its Lorentz contracted electric field on an EO $LiNbO_3$ crystal. The resulted intensity modulation was initially reconstructed using a fast photodiode and a digital oscilloscope. The signal rise time was bandwidth limited ($\sim$ 90ps) from the electronics used and a series of tests to establish our signal EO nature was performed. In particular, the amplitude of the EO modulation was found to increase linearly with the charge of the particle beam and decrease with the optical beam path distance from

the charged particle beam. Also the signal polarity changed sign when the direction of the applied electric field was reversed.

Next an optimized (for maximum modulation), zero bias, EO modulator was constructed for use with the limited dynamic range of the Streak Camera for the first non destructive, completely optical, detection of a charged particle beam. The observed signal may be an image of unexpected piezoelectrically generated sound waves that propagate at the X-axis of the $LiNbO_3$ crystal. In such a case, sound waves generated in the surface as well as inside the crystal, change the index of refraction of the crystal through the photoelastic effect and as a result a diffraction grating is created which in turn causes Bragg polarization effects.

The EO technology holds promise for detectors of greatly improved spatial and temporal resolution for single relativistic charged particles as well as particle beams.

ULTRA-FAST DETECTION OF RELATIVISTIC CHARGED PARTICLE BEAM BUNCHES USING OPTICAL TECHNIQUES

A dissertation submitted to
Kent State University in partial
fulfillment of the requirements for the
degree of Doctor of Philosophy

by

Dimitrios S. Nikas

October, 2003

Dissertation written by

Dimitrios S. Nikas

B.S., Aristotle University of Thessalonika, 1995

Ph.D., Kent State University, 2003

Approved by

_____ , Chair, Doctoral Dissertation Committee

_____ , Members, Doctoral Dissertation Committee

_____ ,

_____ ,

_____ ,

Accepted by

_____ , Chair, Department of Physics

_____ , Dean, College of Arts and Sciences

Table of Contents

List of Figures

List of Tables

Acknowledgments

Being a Ph.D. student is exciting because for the first time in your career you get to apply the accumulated knowledge of years of hard work. However, the road to completion of a Ph.D. thesis is not an easy one. I was blessed to be surrounded by many wonderful people who made my journey much easier.

First and foremost, i would like to thank my thesis advisor, Researcher Yannis K. Semertzidis. I have grown tremendously under his tutelage and inspired by his Physics motivation. I'll never forget his fast, back-of-the-envelope, calculations to unexpected problems.

Next i would like to thank my local (at Kent State Univ.) supervisor Spyridon Margetis. He provided the necessary conditions for me to focus to my thesis. He also guided me during my stay to Kent state University and thoroughly read the thesis for physics corrections and remarks. His support is invaluable to me and it would be difficult to replace him.

Thanks also go to the entire Accelerator Test Facility (located in BNL) staff. Without their help and collaboration our experiments would not be so successful. They not only provided experimental support but also encouragement. Many thanks to all of them.

Next i would like to thank Don Lazarus whose wisdom and experience helped the collaboration tremendously. Also Thomas Tsang with his extraordinary skills in optics and resourceful instant solutions to problems was an inspiration. Finally Triveni Srinivasan-Rao had always a amazing physics motivation and insight and she

is a great asset to the collaboration.

Special thanks go to my diploma thesis advisor, at Aristotle University of Thessalonika, Kostantin Ziouta who supported me at my efforts for a Ph.D. thesis. His physics motivation is an example that i tried to follow during the completion of my thesis.

Special thanks also go to my family and the Margetis family. Without their love and support this thesis would not be possible.

Chapter 1

Introduction

1.1 Experimental Techniques

In recent years the operation of many free electron lasers (FELs) and other accelerator-based light source experiments has required the production of increasingly short (picosecond and sub-picosecond) relativistic electron bunches and the concurrent development of beam diagnostics. Sub-picosecond charged particle beam diagnostics range from very simple, such as an inexpensive thermal detector, to very elaborate optical/electronic instruments, such as the most advanced Streak Cameras (SC). This section describes the most commonly used beam diagnostics and attempts a feature comparison of the Electro-Optic (EO) technique with the existing techniques.

1.2 Ultra-fast Beam Diagnostics

While there is a large number of excellent diagnostics to measure the shape and duration of ultra-short laser pulses, very few alternative measurement techniques exist for short charged particle pulses.

The most widely used technique employs the *coherent synchrotron radiation* (CSR) or the *coherent transition radiation* (CTR) exploiting the fact that short electron bunches radiate more coherent millimeter- and sub-millimeter-wave electromagnetic radiation than longer bunches. Thus the electron bunch length can be minimized in an accelerator simply by adjusting the beam injection parameters while monitoring

the power of the CSR or CTR radiation.

An electron radiates with a wide spectrum when it is bent through a dipole, the so-called synchrotron radiation (SR). When the bunch length of the radiating electron beam is short compared to SR wavelength, the individual electrons radiate in phase and the SR power becomes proportional to the square of the number of electrons per bunch (typical 10^6 to 10^{10}), the so-called coherent synchrotron radiation (CSR). The sensitive dependence of the CSR power on the bunch length can serve as the basis for a non-invasive bunch length monitor. The main shortcomings of such detector is that it can be installed only after a beam dipole and that they cannot measure the longitudinal profile directly. Therefore, the monitor needs to be calibrated against a precise measurement[1].

Transition radiation (TR) is emitted when charged particles pass through a boundary of two media with different dielectric constants. The sudden change of the particle boundary conditions cause them to radiate (TR) with the spectral power entirely dependent upon the degree of coherency, which strongly relates to the beam size. For radiation wavelengths long compared to the bunch length, the total field created by the particles of the bunch is coherent and the total spectral energy is amplified by the square of the number of particles in the bunch. Coherent transition radiation from bunched electrons passing through a metallic foil in vacuum has been observed at millimeter and sub-millimeter wavelengths. This can be done in the time domain with a streak camera but this technique suffers from losses of low-frequency fields which limits the accuracy of the bunch shape. With a Michelson interferometer (see Fig. 1), where the bunch length can be accurately measured but reconstruction of the particle distribution is not possible because the phase information is lost when

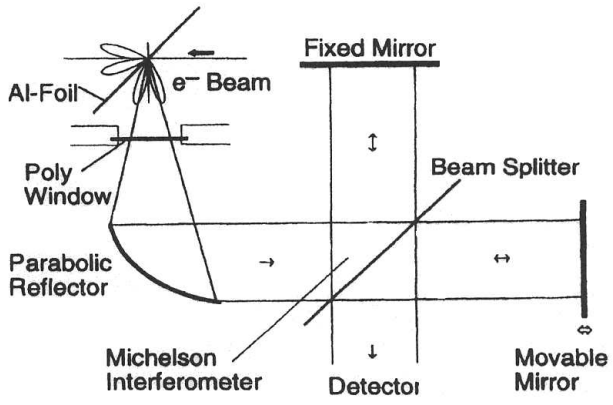

Figure 1: A setup for bunch length measurement using transition radiation and a Michelson interferometer.

the radiation intensity is measured[2]. Also for beams of a few picosecond in length, the bunch length information is being mostly carried in the long wavelengths which are strongly attenuated in the collection optics due to finite aperture and acceptance angles.

The spectrum and the angular distribution of CRT can analyzed in the frequency domain and by Fourier transforming it to time domain, we can obtain information not only about the longitudinal and transverse distributions of electrons in the bunch but also about the divergence of the bunch [3]. This invasive method (see Fig. 2) relies on the use of the Kramers-Kronig relations for the reconstruction process and requires an extrapolation of the measured spectrum to zero frequency. Furthermore, although an asymmetric pulse shape can be obtained, the method cannot distinguish between the leading edge and the trailing edge of the pulse.

Another method is the off-phase RF-acceleration which has been demonstrated

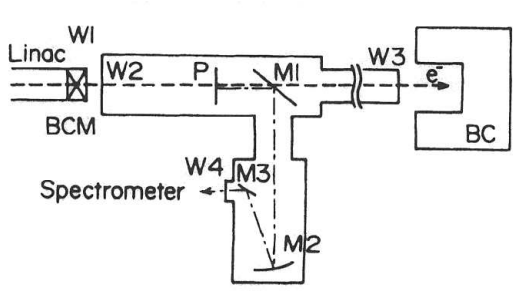

Figure 2: Schematic diagram of an experiment measuring CTR. W1,W2:Ti-foil window; W3:Al window; W4:quartz window; P:Al foil; M1: Al-foil mirror; M2:spherical mirror; M3:plane mirror; BCM:beam current monitor; BC:beam catcher. The trajectory of the beam is shown by the dashed line.

to measure the longitudinal density profile of relativistic electron bunches with subpicosecond time resolution [4]. The method requires that the last RF section is run off-phase so that the accelerating field is ramping up or down rapidly while a relativistic electron bunch passes through. Electrons entering the off-phase accelerator section receive an energy increment that varies in proportion to their time arrival. This transforms the beam's temporal distribution into an energy distribution which can be observed in an energy spectrometer. In practice, the initial energy spread of the beam ΔE_{beam} limits the time resolution of this technique to $\Delta t = \Delta E_{beam}/\alpha$,where α is the maximum available acceleration ramp (in keV/ps). However, with an additional beam transformation from a longitudinally dispersive magnet section such as a chicane, the effect of initial beam energy spread can be removed from the final measurement. Nevertheless, this extra step makes the measurement cumbersome and the off-phase RF section interferes with normal beam operation and can only measure the beam profile at one particular position in the beamline.

There are more facility-specific designs like a streak camera system which detects

the light pulses generated by the electrons at a chromox target screen complemented by the addition of optical transition radiation (OTR) and Ce-doped YAG single-crystal converters which was shown to have a limiting resolution of about 1.6 ps FWHM[5] but they are of limited use and capability.

1.3 Free-Space Electro-Optic Sampling as a Beam Diagnostic

All the methods above have succeeded in measuring sub-picosecond bunch lengths, but they are limited in their ability to observe the bunch shape and most of them are invasive techniques. On the other hand the electro-optic (EO) effect has all the features that one would like to have for use as a sub-picosecond charged particle beam diagnostic:

- it has an inherent femptosecond time resolution[6, 7],
- it is a non-invasive technique and one can construct a real-time feedback system,
- it has linear response to the applied electric field so one can also measure not only the amount of charge (that generates the electric field) but also it sign,
- it can be used in many beamline positions,
- as an optical technique it has all the advantages of such: low noise, small number of expensive read-out systems, excellent electromagnetic isolation, large frequency response, etc.

Since the pioneering experiments of Valdamanis[9, 10] the use of EO effect as a measuring technique for fast time-domain measurements of electric fields has been proven to be powerful, and the idea of electro-optic sampling (EOS) was introduced. Then free-space EOS was introduced for the detection of freely propagating terahertz (THz) beams[8] where time resolution of 20 fs was reported[7]. The use of EOS technique for accelerator related applications like the measurement of RF fields was

suggested[21] and performed[22] but not for the detection of charged particle beams. The idea of using the free-space EOS directly as a beam diagnostic was first suggested by Y. K. Semertzidis[11] and followed by others[12, 13]. The first free-space electro-optic detection of charged particle beam was reported by our group[14, 15] and we also studied it in detail[16].

Independently of our work, an international collaboration has used free-space electro-optic sampling to resolve the electric field of a free electron laser at the facility FELIX[17], to sample the electric field of the transition radiation from an electron beam exiting a beryllium window[18] and sample electron beam bunch in vacuum[19].

Another group from Rochester (NY) attempted to measure the electric fields induced when relativistic charged particles traverse a structure, because of the change in the boundary conditions of the electric field, using the electro-optic sampling technique[20] . These electric fields are unavoidable in accelerators and they are called wakefields.

In this dissertation, the theoretical background necessary for the study of electro-optic sampling will be set, next we describe the experimental setup, and finally we discuss the results along with a glimpse of the future of this technique as we expect it.

Chapter 2

Modulation of Optical Radiation

2.1 Introduction

In anisotropic media (materials whose optical properties depend on the direction of propagation of light as well as its polarization) the polarization ($\vec{P}$) induced by an external electric field ($\vec{E}$) and the field itself are not necessarily parallel. Therefore, instead of a simple scalar relation between $\vec{P}$ and $\vec{E}$ we have

$$P_x = \varepsilon_0(\chi_{11}\ E_x + \chi_{12}\ E_y + \chi_{13}\ E_z)$$

$$P_y = \varepsilon_0(\chi_{21}\ E_x + \chi_{22}\ E_y + \chi_{23}\ E_z) \tag{2.1}$$

$$P_z = \varepsilon_0(\chi_{31}\ E_x + \chi_{32}\ E_y + \chi_{33}\ E_z)$$

where the 3x3 array of the coefficients χ_{ij} is called the *electric susceptibility* tensor. Their magnitudes depend on the choice of the x, y and z axes relative to the crystal structure. Thus, it is always possible to choose x, y and z in such a way that the off-diagonal elements vanish, leaving

$$P_x = \varepsilon_0(\chi_{11}\ E_x), \quad P_y = \varepsilon_0(\chi_{22}\ E_y), \quad P_z = \varepsilon_0(\chi_{33}\ E_z) \tag{2.2}$$

These directions are called the *principal dielectric axes* of the crystal. The electric displacement vector $\vec{D}$ and the electric field $\vec{E}$ are related as follows[49]

$$\vec{D} = \varepsilon_0\vec{E} + \vec{P} \tag{2.3}$$

The above relation can be re-written using the Eq. 2.1 and the dielectric permittivity tensor, defined as $\varepsilon_{ij} = \varepsilon_0(1 + \chi_{ij})$, in tensor notation as

$$D_i = \varepsilon_{ij} E_j \tag{2.4}$$

where i, j are the Cartesian indices that run from 1 to 3. Each term is summed over all repeated indices according to the Einstein sum convention.

If we assume that the medium is homogeneous, non-absorbing and magnetically isotropic, the energy density of the stored electric field in the anisotropic medium is

$$U_e = \frac{1}{2}\vec{E} \cdot \vec{D} = \frac{1}{2} E_i \varepsilon_{ij} E_j$$

$$= \frac{1}{2}(\varepsilon_{xx}E_x^2 + \varepsilon_{yy}E_y^2 + \varepsilon_{zz}E_z^2 + 2\varepsilon_{yz}E_yE_z + 2\varepsilon_{xz}E_xE_z + 2\varepsilon_{xy}E_xE_y)$$

A principal axes transformation can be used to diagonalize the above equation to

$$2U_e = \varepsilon_{xx}E_x^2 + \varepsilon_{yy}E_y^2 + \varepsilon_{zz}E_z^2$$

where x, y, z symbols now refer to the principal dielectric axes. In this system the dielectric tensor is diagonal and the energy stored can be obtain using Eq. (2.4)

$$2U_e\varepsilon_0 = \frac{D_x^2}{\varepsilon_x} + \frac{D_y^2}{\varepsilon_y} + \frac{D_z^2}{\varepsilon_z} \tag{2.5}$$

where $\varepsilon_{x,y,z}$ the (relative) principle dielectric constants. Just looking at the above equation one can make the obvious remark that the constant energy surfaces in the $\vec{D}$ space are ellipsoids. If we replace $\vec{D}/\sqrt{2U_e\varepsilon_0}$ by $\vec{r}$ and define the principal indices of refraction as $n_i^2 = \varepsilon_i$ $(i = x, y, z)$ the last equation can be re-written:

$$\frac{x^2}{n_x^2} + \frac{y^2}{n_y^2} + \frac{z^2}{n_z^2} = 1 \tag{2.6}$$

assuming that *no* external electric field is applied.

The ellipsoid is known as the *index ellipsoid* or more rarely as the *optical indicatrix*. The index ellipsoid can be used to find the two indices of refraction associated with the two linearly and orthogonal polarized plane waves that propagate inside the birefringent medium in an arbitrary direction. In general the index ellipsoid is a triaxial ellipsoid but any central plane cross-section is an ellipse.

2.2 The Electro-Optic Effect

The Electro-Optic (EO) effect is a change in the optical dielectric properties of a medium in response to an applied electric field. The effect is realized as a change in the index of refraction that can cause changes in the dimensions and/or orientation of the index ellipsoid.

The electro-optic effect reflects the index of refraction dependence on the distribution of charges in the medium. The application of an electric field will result in a re-distribution of the bond charges and possibly a slight deformation of the ion lattice. These displacements create electric dipoles whose macroscopic manifestation is the electric polarization $\vec{P}$. The electro-optic coefficients are traditionally defined in terms of the impermeability tensor

$$\eta_{ij} = \varepsilon_{ij}^{-1}$$

by the following power series

$$\eta_{ij}(\vec{E}) - \eta_{ij}(0) = r_{ijk}\ E_k + s_{ijkl}\ E_k\ E_l \tag{2.7}$$

$$= f_{ijk}\ P_k + g_{ijkl}\ P_k\ P_l$$

where $\vec{E}$ is the applied electric field and $\vec{P}$ the polarization field vector. The constants r_{ijk} and f_{ijk} are the linear (or Pockels) electro-optic coefficients and the s_{ijkl}

and g_{ijkl} are the quadratic (or Kerr) coefficients. Higher order terms are neglected because they are too small for most applications. The quadratic effect was first discovered by J.Kerr, in 1875[24], and F.Pockels studied the linear electro-optic effect in 1893[25]. The linear Pockels effect exists only in crystals that do not possess inversion symmetry[26]. The electro-optic coefficients are related by the following

$$f_{ijk} = \frac{r_{ijk}}{\varepsilon_k - \varepsilon_0}$$

$$g_{ijkl} = \frac{s_{ijkl}}{(\varepsilon_k - \varepsilon_0)(\varepsilon_l - \varepsilon_0)}$$

where ε_k, ε_l are the principal optical dielectric constants.

In the presence of an electric field, the equation of the index ellipsoid becomes[23]

$$(\frac{1}{n^2})_1\ x^2 + (\frac{1}{n^2})_2\ y^2 + (\frac{1}{n^2})_3\ z^2 + 2(\frac{1}{n^2})_4\ yz + 2(\frac{1}{n^2})_5\ xz + 2(\frac{1}{n^2})_6\ xy = 1 \tag{2.8}$$

If we choose x, y and z to be parallel to the principal dielectric axes of the crystal then with zero applied field Eq. (2.8) must reduce to Eq. (2.6) and therefore

$$\left(\frac{1}{n^2}\right)_1\Bigg|_{E=0} = \frac{1}{n_x^2}, \quad \left(\frac{1}{n^2}\right)_2\Bigg|_{E=0} = \frac{1}{n_y^2}, \quad \left(\frac{1}{n^2}\right)_3\Bigg|_{E=0} = \frac{1}{n_z^2}$$

$$(\frac{1}{n^2})_4\Big|_{E=0} = (\frac{1}{n^2})_5\Big|_{E=0} = (\frac{1}{n^2})_6\Big|_{E=0}$$

In this form, the r_{ijk} coefficients have 27 components that correspond to the 27 components of the susceptibility tensor χ_{ijk}. From permutation relations it can be shown[27] that (ijk) is equivalent to (jik) and hence a reduced form of the electro-optic tensor, r_{ij}, can be used. This tensor contains 18 elements (6x3 matrix) of which many are usually equal or identically zero owing to crystal symmetry properties. This

allows us to rewrite the linear term of Eq. (2.7) in a matrix form as

$$\begin{vmatrix} \Delta(\frac{1}{n^2})_1 \\ \Delta(\frac{1}{n^2})_2 \\ \Delta(\frac{1}{n^2})_3 \\ \Delta(\frac{1}{n^2})_4 \\ \Delta(\frac{1}{n^2})_5 \\ \Delta(\frac{1}{n^2})_6 \end{vmatrix} = \begin{vmatrix} r_{11} & r_{12} & r_{13} \\ r_{21} & r_{22} & r_{23} \\ r_{31} & r_{32} & r_{33} \\ r_{41} & r_{42} & r_{43} \\ r_{51} & r_{52} & r_{53} \\ r_{61} & r_{62} & r_{63} \end{vmatrix} \begin{vmatrix} E_1 \\ E_2 \\ E_3 \end{vmatrix} \tag{2.9}$$

where using matrix multiplication one can find the impermeability tensor in the desired direction. For example

$$(\frac{1}{n^2})_1 = r_{11}\,E_1 + r_{12}\,E_2 + r_{13}\,E_3$$

This can be transformed to relate the change in index of refraction to the applied electric field as follows

$$r_{ij}\,E_j = \Delta(\frac{1}{n^2})_i = -\frac{2\Delta n_i}{n_i^3}$$

assuming $\Delta n_i \ll n_i$ as is usually the case. Thus we obtain the most common electro-optic relation

$$\Delta n_i = -\frac{1}{2} n_i^3\, r_{ij}\, E_j \tag{2.10}$$

Two values of r_{ij} are commonly specified. If the crystal is at constant stress, or "free", then the electro-optic coefficient is denoted with the superscript T, e.g r_{ij}^T.

The "free" condition is exemplified at low frequencies, below acoustic resonances, where the elasto-optic and piezo-optic effects can contribute (look Fig. 1). If the electro-optic coefficient is determined at constant strain, or "clamped", then it is written with the superscript S. r_{ij}^S is the value of the electro-optic coefficient obtained in the RF regime, ie. between the acoustic and lattice resonances.

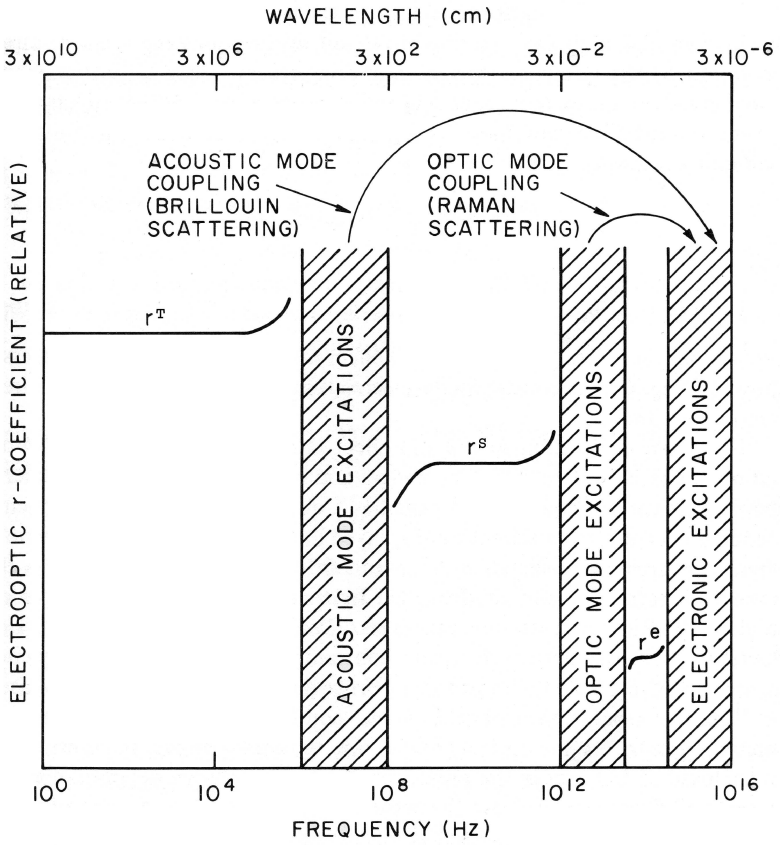

Figure 1: Schematic illustration of the various coupling processes producing the EO coefficients r^T, r^S, and r^e. In general these coefficients can have any combination of relative magnitude and signs. For $LiNbO_3$, r^e and r^T account for $\sim$10% of the total EO effect each [28].

2.3 Electro-Optic Retardation

In the previous sections we saw that the application of an electric field can change the index of refraction and hence the index ellipsoid of certain materials. Now we will see how this change of index ellipsoid can be used to rotate the polarization state of light waves.

Consider normal incidence of coherent light on an electro-optic crystal of length ℓ, as in Fig. 2. At the input plane (z=0) we can resolve the light into two orthogonal

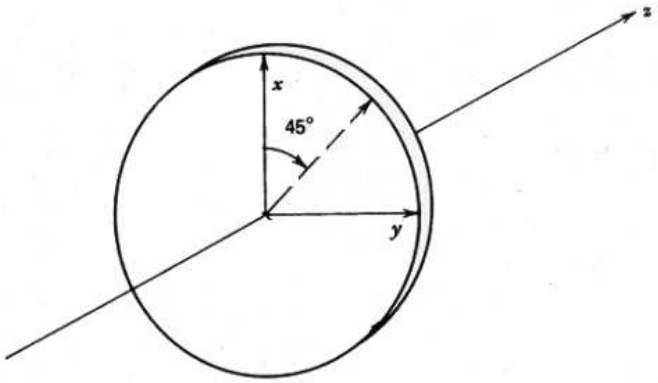

Figure 2: Light propagating at z-axis and polarization in 45^0 with respect the crystal axes.

components polarized along x and y. With the application of an external electric field on the crystal, the index of refraction of x or y or both will change according to Eq. (2.10). Thus, each component will acquire a different phase (ϕ) and the phase difference between the two components, at the output plane (z = ℓ), is called *retardation* (Γ) and is equal to[23]

$$\Gamma = \phi_x - \phi_y = \frac{\omega}{c}\,\Delta n \cdot \ell = \frac{2\pi}{\lambda}\,\Delta n \cdot \ell \tag{2.11}$$

where Δn is the field induced birefringence, ω the frequency of light and λ its wavelength. This way, the state of polarization is altered from the input unless the retardation is an integer multiple of 2π.

2.4 The Electro-Optic Effect in Uniaxial Crystals

In the general case where the three principal indices n_x, n_y, n_z are all different, there are two optical axes and the material is called biaxial. In many optical materials two of the principal indices are equal, in which case the Eq. (2.6) of the index ellipsoid

simplifies to

$$\frac{x^2}{n_0^2} + \frac{y^2}{n_0^2} + \frac{z^2}{n_e^2} = 1 \tag{2.12}$$

and the material is called uniaxial. The Eq. (2.12) is represented graphical in Fig. 3.

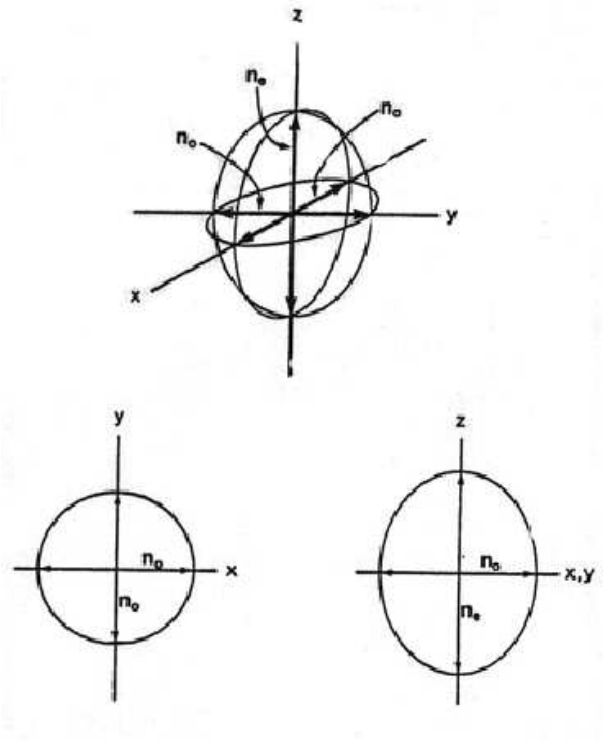

Figure 3: The index ellipsoid of a uniaxial material and its projections to z and x,y planes.

One of the most widely used uniaxial electro-optic materials is Lithium Niobate ($LiNbO_3$). This ferroelectric material has a triagonal crystal structure (point group 3m) and is characterized by large pyro-electric, piezo-electric, electro-optic and photo-elastic coefficients. It is a synthetic dielectric material that doesn't exist in nature.

Its electro-optic coefficient matrix for mirror plane perpendicular to x-axis ($m \perp x$)

is

$$r_{ij} = \begin{vmatrix} 0 & -r_{22} & r_{13} \\ 0 & r_{22} & r_{13} \\ 0 & 0 & r_{33} \\ 0 & r_{51} & 0 \\ r_{51} & 0 & 0 \\ -r_{22} & 0 & 0 \end{vmatrix} \tag{2.13}$$

where $r_{51} = r_{42}$, $r_{22} = -r_{12} = -r_{61}$, and $r_{13} = r_{23}$. Thus, the EO effect in lithium niobate can be described by four independent coefficients (r_{51}, r_{22}, r_{13} and r_{33}) whose values are listed in table 1:

Electro-Optical Coefficients of $LiNbO_3$ at 633nm, 25^0C (pm/V)	Indices of Refraction[29] at 1320nm	at 514nm	Pockels Coefficients at 633nm (pm/V)
$r_{33} = 28.8$	$n_0 = 2.24$	$n_0 = 2.337$	$n_e^3 r_{33} = 306.6$
$r_{13} = 7.7$	$n_e = 2.14$	$n_e = 2.239$	$n_0^3 r_{13} = 92.6$
$r_{22} = 3.4$	$\Delta n = 4.7\%$	$\Delta n = 4.4\%$	$n_0^3 r_{22} = 36.2$
$r_{51} = r_{42} = 18.2$	$\varepsilon_3 = 28$,	$\varepsilon_1 = \varepsilon_2 = 43$	$n_0^3 r_{51} = 218.85$

Table 1: The optical and electro-optical properties of $LiNbO_3$.

The index ellipsoid of $LiNbO_3$ in the general case of an applied electric field $\vec{E} = (E_x, E_y, E_z)$ is

$$\begin{aligned} [\frac{1}{n_x^2} - r_{22}\, E_y \;\; &+ \;\; r_{13}\, E_z]x^2 + [\frac{1}{n_y^2} + r_{22}\, E_y + r_{13}\, E_z]y^2 + [\frac{1}{n_z^2} + r_{33}\, E_z]z^2 \\ &+ \;\; 2yz\, r_{51}\, E_y + 2xz\, r_{51}\, E_x - 2xy\, r_{22}\, E_x = 1 \end{aligned} \tag{2.14}$$

The changes in orientation and length of the principal axes of the ellipsoid for all propagation directions of the optical beam and for all directions of applied electric field are summarized next and studied in detail in **Appendix A**.

2.4.1 Summary of Electro-optic properties of $LiNbO_3$

Direction of Light Prop.	Electric Field applied in the direction of $\hat{X}$-axis	Electric Field applied in the direction of $\hat{Y}$-axis	Electric Field applied in the direction of $\hat{Z}$-axis
$\hat{X}$-axis	$\Gamma = \emptyset$	$\Gamma^{(1)} = \pi\frac{E_r\ell_r}{\lambda\,\varepsilon_r}\cdot[\,2(n_e^3 + n_0^3)\,r_{51}\cdot\sin\phi + n_0^3\,r_{22}\,]$	$\Gamma = \pi\frac{E_r\ell_r}{\lambda\,\varepsilon_r}\cdot(n_e^3\,r_{33} - n_0^3\,r_{13})$
$\hat{Y}$-axis	$\Gamma^{(2)} = \pi\frac{E_r\ell_r}{\lambda\,\varepsilon_r}\cdot(n_e^3 + n_0^3)\,r_{51}\cdot\sin 2\phi$	$\Gamma^{(1)} = \pi\frac{E_r\ell_r}{\lambda\,\varepsilon_r}\cdot(n_0^3\,r_{22} - 2n_e^3\,r_{51}\cdot\sin\phi)$	$\Gamma = \pi\frac{E_r\ell_r}{\lambda\,\varepsilon_r}\cdot(n_e^3\,r_{33} - n_0^3\,r_{13})$
$\hat{Z}$-axis	$\Gamma^{(3)} = 2\pi\frac{E_r\ell_r}{\lambda\,\varepsilon_r}\cdot n_0^3\,r_{22}$	$\Gamma^{(1)} = 2\pi\frac{E_r\ell_r}{\lambda\,\varepsilon_r}\cdot n_0^3\,(r_{22} + r_{51}\cdot\sin\phi)$	$\Gamma = \emptyset$

Table 2: This table is a summary of the induced retardation by the electro-optic for all the cases of applied electric field and light propagation.

where ℓ_r is the effective optical path length in the crystal, λ the wavelength of the light, ε_r the EO crystal dielectric constant and E_r is the electric field or $E_r = \frac{V}{d}$ in the case of a transverse EO experiment in the lab where d is the plate distance in the electric field direction and V the applied voltage.

[1] The angle of rotation of the index ellipsoid around the $\hat{x}$-axis is: $tan2\phi = \frac{2r_{51}\,E_r}{\frac{1}{n_0^2}-\frac{1}{n_e^2}+r_{22}\,E_r}$

[2] The angle of rotation of the index ellipsoid around the $\hat{y}$-axis is: $tan2\phi = \frac{2r_{51}\,E_r}{\frac{1}{n_0^2}-\frac{1}{n_e^2}}$

[3] The angle of the index ellipsoid around the $\hat{z}$-axis is independent of the electric field and equal to: $\phi = 45^0$

2.5 Amplitude Modulation

In the previous sections we saw how the EO effect alters the polarization of the light. This change in polarization can be converted to an intensity change by placing the crystal between crossed linear polarizers as pictured at Fig. 4.

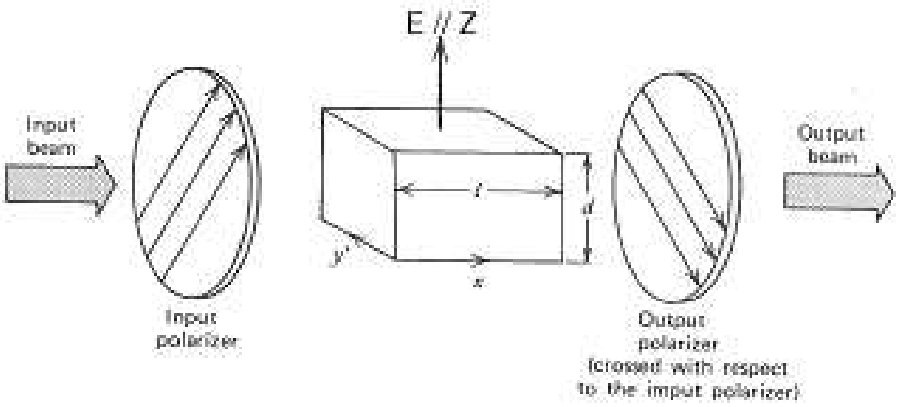

Figure 4: A typical electro-optic modulator.

Suppose an x-cut $LiNbO_3$ crystal is placed between the two crossed polarizers and the electric field applied to the direction of the z-axis. The polarization of the input light is at an angle with respect the axes of the crystal and assume for simplicity that the angle is 45^0. Then, at the input crystal yz surface (at x=0) light will be analyzed into two equal and in-phase components along y and z axes. If there is no electric field applied then a static retardation will be acquired because the two axes naturally have different indices of refraction. This is realized as a DC light coming out of the crossed polarizer which would normally block all the light. But as we saw at section 2.3.1, for the time the electric field is applied at z-axis, a field induced retardation is acquired by the light. So, upon emerging from the output face $x = \ell$, the y and z components have a relative phase shift (retardation) of Γ radians, as shown at Eq.

(A.3) on page 122, and we may describe them as

$$\begin{aligned} E_y(\ell) &= A \\ E_z(\ell) &= A\, e^{-i\Gamma} \end{aligned}$$

The total field emerging from the output of the crossed polarizer (analyzer) is the sum of the 45^0 components of E_y and E_z

$$E_{45^0} = \frac{A}{\sqrt{2}}(e^{-i\Gamma} - 1)$$

that corresponds to an output intensity

$$\begin{aligned} I &= E_{45^0} \cdot E^*_{45^0} \\ &= \frac{A^2}{2}[(e^{-i\Gamma} - 1)(e^{i\Gamma} - 1)] = 2A^2 \sin^2 \frac{\Gamma}{2} \end{aligned}$$

The transmission factor (ratio of the output intensity to the input I/I_0) is

$$\frac{I}{I_0} = \sin^2 \frac{\Gamma}{2} \tag{2.15}$$

and is plotted in Fig. 5.

In the general case where the polarization of light is inserted with an angle θ with respect the axes of the crystal, the transmission factor of a EO setup between crossed polarizers is

$$\frac{I}{I_0} = \sin^2(2\theta) \cdot \sin^2 \frac{\Gamma}{2} \tag{2.16}$$

Usually the retardation is small, on the order of a few mrad, and we can safely assume that $\sin^2 \frac{\Gamma}{2} \approx (\frac{\Gamma}{2})^2$ resulting a non-linear dependence of our signal, to the electric field. Introducing a small misalignment angle α between the polarizer and the analyzer it amplifies the signal

$$\frac{I}{I_0} = \alpha^2 + \Gamma^2 \cdot \sin^2 \theta \cdot (\alpha \sin \theta + \cos \theta)^2 \tag{2.17}$$

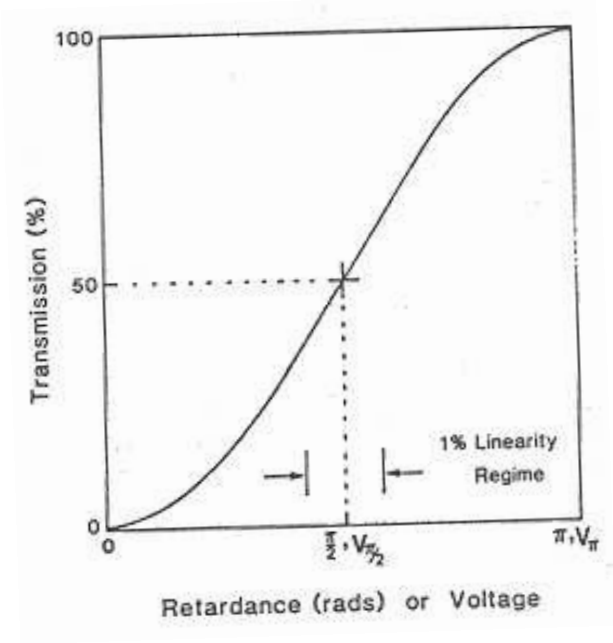

Figure 5: Transmission factor of a crossed polarized electro-optic modulator as a function of applied voltage and retardance. A modulator is biased at 50% intensity transmission point when $\Gamma_0 = \frac{\pi}{2}$.

but again the signal is not linear. To deduce the equation above one needs to make use of *Jones Matrices*, and is done analytically in **Appendix B**.

In order to linearize our signal, we need to introduce a bias to the EO setup. A modulator is usually biased either by applying a DC voltage to the crystal or using a naturally birefringent crystal to introduce a phase difference Γ_0 (retardation) between the two components. For example, using a quarter wave plate (known also as QWP or $\Gamma_0 = \frac{\pi}{2}$) with its axes parallel to the crystal axis (0^0 degrees misalignment) the transmission factor becomes

$$\begin{aligned} \frac{I}{I_0} &= \alpha^2 + (\Gamma + \Gamma_0)^2 \cdot \sin^2\theta \cdot (\alpha \sin\theta + \cos\theta)^2 \\ &= \sigma^2 + \alpha^2 + (\Gamma^2 + \frac{\pi^2}{4} + \Gamma\pi) \cdot \sin^2\theta \cdot (\alpha \sin\theta + \cos\theta)^2 \end{aligned} \tag{2.18}$$

and the last linear term of Eq. (2.18) dominates the signal. The equation above was derived from Eq. 2.17 taking into account that the QWP introduces a bias of $\Gamma_0 = \frac{\pi}{2}$. The same result can also be derived using Jones matrices but this is more straightforward.

In bibliography there are two favorable operation points for using a modulator:

• $\Gamma_0 = \frac{\pi}{2}$ bias is called the 50% intensity transmission point. As can be seen in Fiq. 5, it relocates the output at the linear region (within ∼1%) of the transmission curve. This is usually accomplished with the use of a $\frac{\lambda}{4}$-plate (QWP) whose function is to introduce an additional 90^0 phase retardation in one of the components of the beam so that in the absence of the electric field, the laser beam polarization will be changed from linear to circular. The circularly polarized laser beam will then be split by the analyzing polarizer into two beams with equal intensity which is half the intensity of the input beam. This puts the operating point at 50% optical bias.

• $\Gamma_0 \approx 0$ bias is called the near zero transmission point. As the name suggests, the output (Fiq. 5) is located at the beginning of the transmission curve which is also linear for a much smaller region (compared with the case above).

The optimal bias point depend on the application alone. If the intense background produced when working on the 50% bias point is not an issue, then it is preferred because of the big signal amplitude although the *Modulation* (the ratio of AC to DC light) is very small. When the detection scheme requires minimal background light or an optimized modulation, then the use of near zero point bias is preferred.

2.5.1 Amplitude Modulation at 50% Intensity Transmission Point

In order to bring our mathematical constructions closer to a real experiment, we must consider the effect of incomplete extinction ratio for the crossed polarizers as is

often the experimental case. We define the extinction ratio (σ^2) as the ratio of the minimum over the maximum transmitted light after the analyzer

$$\sigma^2 = \frac{I_{min}}{I_{max}} \tag{2.19}$$

When working in the 50% bias point, one uses an x or y-cut $LiNbO_3$ crystal with the light polarization at $\theta = 45^0$ with respect the z and x or y axis of the crystal so we will focus at this case. For $\theta = 45^0$, Eq. 2.18 becomes

$$\begin{aligned} I &= I_0 \left[\sigma^2 + \alpha^2 + (\Gamma^2 + \frac{\pi^2}{4} + \Gamma\pi) \cdot \frac{(\alpha+1)^2}{4}\right] \\ &\simeq I_0 \left[\sigma^2 + \alpha^2 + (\frac{\pi}{4} + \Gamma) \cdot \frac{\pi\,(\alpha+1)^2}{4}\right] \end{aligned} \tag{2.20}$$

taking into account that Γ is only a few tenths of mrad ($\Gamma \ll 1$) so we can safely ignore the very small Γ^2 terms.

First find the DC light exiting the analyzer when there is no applied electric field ($\Gamma = 0$)

$$I_{DC} = I_0\,(\sigma^2 + \alpha^2 + \frac{\pi^2}{16} \cdot (\alpha+1)^2) \tag{2.21}$$

and then the signal intensity (AC), the term that depends on the retardation and thus on the applied electric field is

$$I_{AC} = I_0\,\Gamma\,\frac{\pi\,(\alpha+1)^2}{4} \tag{2.22}$$

The modulation (MD) is the ratio of the AC over the DC intensity, and in this case is

$$MD = \frac{I_{AC}}{I_{DC}} = \frac{\Gamma}{4}\,\frac{\pi\,(\alpha+1)^2}{\sigma^2 + \alpha^2 + \frac{\pi^2}{16} \cdot (\alpha+1)^2} \tag{2.23}$$

In order to find the maximum modulation we have to find first the misalignment α for which the modulation takes its maximum value:

$$\frac{\partial(MD)}{\partial\alpha} = \frac{\pi\,\Gamma\,(\alpha+1)}{4}\cdot\frac{\alpha-2\,\sigma^2}{(\sigma^2+\alpha^2+\frac{\pi^2}{16}\cdot(\alpha+1)^2)^2} = 0$$

$$\Rightarrow\ \alpha_{max} = 2\,\sigma^2 \tag{2.24}$$

and the maximum modulation value for this case is

$$MD_{max} = \frac{\Gamma}{4}\,\frac{\pi\,(2\sigma^2+1)^2}{\sigma^2+4\sigma^4+\frac{\pi^2}{16}\cdot(2\sigma^2+1)^2} \tag{2.25}$$

while the typical value for the extinction ratio (σ) in this case is

$$\sigma\sim\frac{1}{100}\sim 10^{-2}\ll 1 \tag{2.26}$$

much smaller than one and it can be safely ignored to give an approximate maximum modulation of

$$MD_{max} = \frac{\Gamma}{4}\,\frac{\pi}{\frac{\pi^2}{16}}\simeq\Gamma\ \Rightarrow\ MD_{max}\sim 10^{-2}\ \ (at\ \alpha_{max}\sim 1^0) \tag{2.27}$$

since the retardation is typically a few tenths of mrad as we saw in the case of $LiNbO_3$(Table 1 on page 124). Thus the maximum modulation is indeed very small in the case of 50% intensity transmission, as was pointed out earlier. However, the signal magnitude is the biggest one can possibly have, and this method is preferred if the big background that accompanies the signal is not an issue.

2.5.2 Amplitude Modulation at Near Zero Optical Bias Point

Taking into account the incomplete extinction ratio, the intensity of the light exiting the analyzer, Eq. (2.15), becomes

$$I = I_0\,[\sigma^2+\sin^2(\Gamma_0+\Gamma)] \tag{2.28}$$

where Γ_0 is the bias we introduce to linearize the effect and Γ is the electro-optically induced retardation.

• If the bias is small, we know that the retardation is small so we can use the approximation

$$\sin^2(\Gamma_0 + \Gamma) \approx (\Gamma_0 + \Gamma)^2 = \Gamma_0^2 + \Gamma^2 + 2\Gamma_0\Gamma \tag{2.29}$$

and the equation (2.28) becomes

$$I = I_0 \left[\sigma^2 + \Gamma_0^2 + \Gamma^2 + 2\Gamma_0\Gamma\right] \tag{2.30}$$

The DC level is the light intensity exiting the analyzer when there no applied electric field ($\Gamma = 0$). In this case it is

$$I_{DC} = I_0 \left(\sigma^2 + \Gamma_0^2\right) \tag{2.31}$$

and the signal intensity is

$$I_{AC} = I_0 \left(\Gamma^2 + 2\Gamma_0\Gamma\right) \tag{2.32}$$

The modulation (MD) in this case is

$$MD = \frac{\Gamma^2 + 2\Gamma_0\Gamma}{\sigma^2 + \Gamma_0^2} \tag{2.33}$$

It is clear that there is an optimum point to the above equation and we find it by taking the derivative of MD with respect to Γ_0.

In general, the induced retardation is small and we can ignore the second order term. Thus, we have:

$$\frac{\partial(MD)}{\partial\Gamma_0} = \frac{2\Gamma(\sigma^2 - \Gamma_0^2)}{(\sigma^2 + \Gamma_0^2)^2} = 0 \Rightarrow \Gamma_{0(max)} = +\sqrt{\sigma^2} \tag{2.34}$$

and the modulation is maximum when the bias is equal to the square root of the extinction ratio. Therefore, the maximum modulation value is:

$$MD_{max} = \frac{\Gamma}{\sqrt{\sigma^2}} \tag{2.35}$$

The remarkable result of the above equation is that the maximum modulation depends linearly with the retardation (just like in the case of 50% bias) but in this case we have an inverse square root dependence with extinction ratio which makes all the difference. What it means is that in an optical setup with very low extinction ratio, we could actually amplify our maximum modulation.

In our analysis of the retardation expected from $LiNbO_3$ for different optical setups, we found that the maximum retardation is provided by a x,y-cut crystal when the electric field is applied at z-axis where we get (from Table 1 on page 124) Γ =133mrad. Using this crystal orientation in an optical setup, the intrinsic (static) birefringence created from the difference of the index of refraction between x,y and z axis gives a high extinction ratio on the order of $\sim 3 - 4 \cdot 10^{-3}$. Now looking at the case of a z-cut crystal with the electric field applied on x,y axis, we see from Table 6, on page 132, that we expect a retardation about ∼4 times smaller than the previous case, but now we avoid the intrinsic birefringence since the two axes x and y don't have any difference in the index of refraction. Implemented in an optical setup, one typically gets a very low extinction ratio in the order of a few $\sim 3 - 4 \cdot 10^{-4}$.

Using these numbers in Eq. 2.35, we find for the case of a z-cut crystal with electric field on x,y axis, the maximum modulation

$$MD_{max} = \frac{\Gamma}{\sqrt{\sigma^2}} \simeq \frac{3 - 4 \cdot 10^{-3}}{\sqrt{3 - 4 \cdot 10^{-4}}} \Rightarrow MD_{max} \sim 10^{-1} \; (at \; \Gamma_{0(max)} \sim 1^0) \tag{2.36}$$

which is about 1 order of magnitude bigger than the case of 50% bias. That of course

is possible only using the appropriate setup of very low extinction ratio.

• In order to study the case of a non-negligible bias, we need a more general approximation than Eq. (2.29). For that we will make use of trigonometric identities to conclude:

$$\sin^2(\Gamma_0+\Gamma) = \frac{1}{2} - \frac{1}{2}\cos 2(\Gamma_0+\Gamma) = \frac{1}{2}(1 - \cos 2\Gamma_0 \cdot \cos 2\Gamma + \sin 2\Gamma_0 \cdot \sin 2\Gamma) \tag{2.37}$$

When the retardation is small, we can replace the sine and cosine with the series

$$\sin\Gamma = \Gamma - \frac{\Gamma^3}{3!} + \frac{\Gamma^5}{5!} + ...$$
$$\cos\Gamma = 1 - \frac{\Gamma^2}{2!} + \frac{\Gamma^4}{4!} + ...$$

and Eq. (2.37) becomes

$$\begin{aligned} \sin^2(\Gamma_0+\Gamma) &= \frac{1}{2} - \frac{1}{2}\cos 2\Gamma_0 + \Gamma^2\cos 2\Gamma_0 - \frac{1}{3}\Gamma^4\cos 2\Gamma_0 \\ &+ \Gamma\sin 2\Gamma_0 - \frac{2}{3}\Gamma^3\sin 2\Gamma_0 + \frac{2}{15}\Gamma^5\sin 2\Gamma_0 \end{aligned} \tag{2.38}$$

The DC light that exits the analyzer in this case is:

$$I_{DC} = I_0(\sigma^2 + \sin^2\Gamma_0) \tag{2.39}$$

and the signal intensity is:

$$\begin{aligned} I_{AC} &= I_0\Gamma^2\cos 2\Gamma_0 - \frac{I_0}{3}\Gamma^4\cos 2\Gamma_0 + I_0\Gamma\sin 2\Gamma_0 \\ &- \frac{2I_0}{3}\Gamma^3\sin 2\Gamma_0 + \frac{2I_0}{15}\Gamma^5\sin 2\Gamma_0 \end{aligned} \tag{2.40}$$

The modulation (MD) in this case is:

$$MD = \frac{\Gamma^2\cos 2\Gamma_0 - \frac{1}{3}\Gamma^4\cos 2\Gamma_0 + \Gamma\sin 2\Gamma_0 - \frac{2}{3}\Gamma^3\sin 2\Gamma_0 + \frac{2}{15}\Gamma^5\sin 2\Gamma_0}{\sigma^2 + \sin^2\Gamma_0}$$

where the optimum modulation point is not so obvious. Taking again the derivative of the MD with respect to Γ_0, and ignoring the higher-order terms of retardation, we find that

$$\Gamma_{0(max)} \approx \cos[\frac{1+4\sigma^2-2\Gamma\sigma\sqrt{1+\sigma^2}}{2+8\sigma^2}] \tag{2.41}$$

A simulation of the modulation percentage for different extinction ratios and bias can be seen in Fig. 6 for a retardation of $\Gamma = 1mrad$.

2.6 Acousto-Optics

Seventy one years have passed since Debye and Sears[30] and Lucas and Biquard[31] observed diffraction of light by an ultrasonic wave propagating in an interaction medium. These were the first experimental verifications of the light-sound interaction phenomenon predicted by Brillouin[32]. Since then, a great number of theoretical and experimental studies have been performed to understand the phenomenon. The most useful theoretical treatment dating from the early stage of work appeared in a series of papers written by Raman and Nath[32]. The simple phase-grating theory developed by them explained well the multi-order diffraction phenomenon, contrary to Brillouin's expectation. This phenomenon is observed in the low-acoustic-frequency region. However it should be noted that the Raman-Nath theory can be applied only to the case where the sound intensity is not so strong and the interaction length is not so long, such that at most ten orders of diffraction are observed.

It was also observed that when the frequency of the acoustic wave is raised, the diffraction to higher orders is eliminated and, at certain angles of light incidence, energy exchange between zeroth- and first-order light beams become predominant. This type of diffraction, exactly the one predicted by Brillouin, was first observed

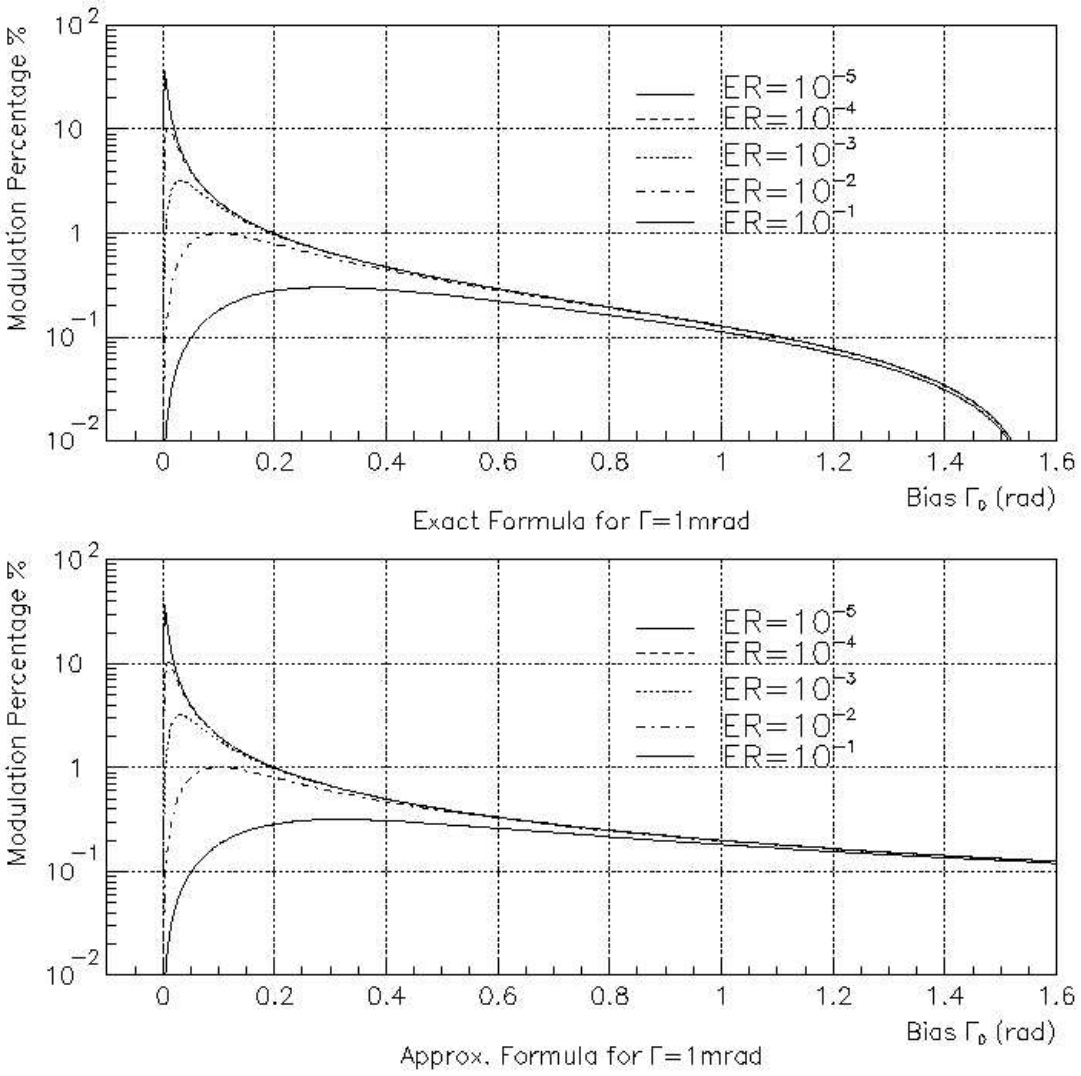

Figure 6: Using an retardation of $\Gamma = 1mrad$, the expected modulation was simulated for both small values approximation (see Eq. 2.33) (top plot) and exact solution (see Eq. 2.41) (bottom plot). With different lines are the same calculations for different extinction ratio.

by Rytow[33]. This phenomenon is closely analogous to X-ray (Bragg) diffraction in crystals where the atomic planes cause multiple reflections of the incident electromagnetic radiation that interfere constructively for certain critical angles. In acoustic diffraction, the role of the atomic planes is assumed by planes of compression and rarefaction, induced by ultrasonic waves.

2.6.1 Theory

The interaction between the light and the ultrasound can be treated by resolving the diffracted light into a series of plane waves. These ideal plane waves are subject to "spread functions" which are characteristic of the optical system. A general treatment of the problem of ultrasonic diffraction is discussed elsewhere[34] and only a brief outline will be given here[35].

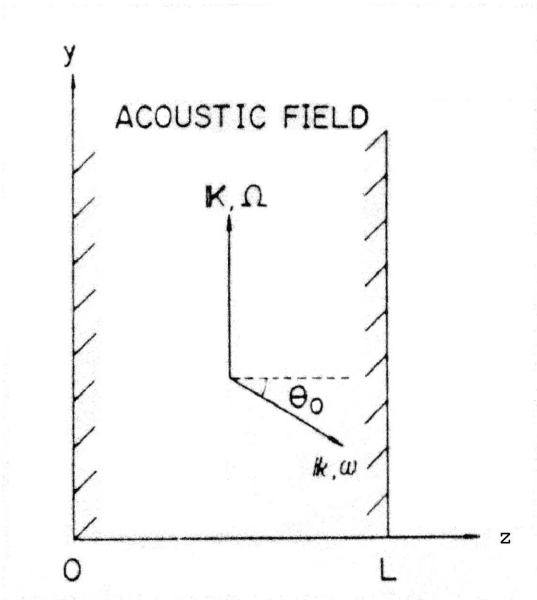

Figure 7: Geometry of the light-sound interaction.

Assume an acoustical wave is propagating in an optical medium in the y-axis

direction and an optical wave is traversing the same medium in the z-axis direction, as depicted in Fig. 7. The optical wave equation which describes the propagation of the electric intensity can be written

$$\nabla^2 E \;=\; \frac{[n(y,t)]^2}{c^2}\,\frac{\partial^2 E}{\partial t^2} \tag{2.42}$$

where c is the speed of light in free space and $n(y,t)$ is the refractive index in the region of interaction. We assume for simplicity that the acoustic wave is a planar traveling wave with sinusoidal vibration $n(y,t)$ given by

$$n(y,t) \;=\; n + \Delta n\,\sin(\Omega t - Ky) \tag{2.43}$$

where n is the average refractive index of the medium and Δn is the amplitude of the index change. The perturbed optical field is periodic in time and space with the acoustic field, and it can be expanded into the Fourier series

$$E \;=\; \sum_{m=-\infty}^{\infty} E_m(z)\; exp[\,j\{(\omega \;+\; m\Omega)t \;-\; \mathbf{k_m}\cdot\mathbf{r}\}\,] \tag{2.44}$$

where

$$\mathbf{k_m}\cdot\mathbf{r} \;=\; k\,(z\,\cos\theta_0 \;-\; y\,\sin\theta_0) \;+\; mKy \tag{2.45}$$

and $E_m(z)$ represents the amplitude of the mth diffracted light with frequency of $\omega + m\Omega$. Substituting Eq. (2.43- 2.45) into Eq. (2.42) and neglecting second order terms, we obtain a set of equations

$$\frac{dE_m}{dz} \;+\; \frac{\alpha}{2L}(E_{m+1} - E_{m-1}) \;=\; -j\frac{mK}{\cos\theta_0}(\sin\theta_0 \;-\; m\,\sin\theta_B)E_m \tag{2.46}$$

where

$$\alpha \;=\; -\frac{k_f\,\Delta n\,L}{\cos\theta_0} \tag{2.47}$$

and

$$\sin\theta_B \;=\; \frac{K}{2k} \tag{2.48}$$

Here k_f is the free space optical wave number and θ_B is the Bragg angle in the medium. The Bragg angle definition Eq. (2.48) implies a momentum conservation relation in which the frequency shift of the diffracted light beam is neglected[58].

Looking at the second term of Eq. (2.46) left-hand side (lhs), an amount of energy can only be transferred between the mth and next or previous mode and that amount depends on the coupling coefficient α. This is a consequence of the assumed sinusoidal form of the sound field and not a general result. Thus for sinusoidal sound fields, an appreciable amount of light can be transferred out of the zeroth order only if either or both the coefficients of the right-hand side (rhs) of Eq. (2.46) are small for $m = \pm 1$. This can be accomplished in either of the two ways:

- by working at or near normal incidence and having K or f small, or
- by working at angles of incidence corresponding to θ_B with large f or K.

The former allows the light to be transferred not only from the zeroth to the first orders, but also from the first to the second and so on. On the other hand, for large frequencies of the acoustic wave f, light is transferred only to the first order (Bragg diffraction).

2.6.2 Case I:Raman-Nath Diffraction

In the first extreme case where the acoustic frequency is low , the term $m \sin\theta_B$ in the rhs of Eq. (2.46) is neglected and we obtain the solution

$$E_m(z) \;=\; exp\left(-\frac{1}{2}jm\,K\,z\,tan\theta_0\right)\; J_m\left[\alpha\frac{\sin(K\,z\,tan\theta_0/2)}{K\,L\,tan\theta_0/2}\right] \tag{2.49}$$

where J_m is the Bessel function of order m. The normalized intensity of the mth diffracted light at L is given by

$$I_m = E_m(L)\, E_m^*(L) = J_m^2\left(\alpha\frac{\sin\chi}{\chi}\right) \tag{2.50}$$

where

$$\chi = K\, L\, tan\frac{\theta_0}{2} \tag{2.51}$$

and E_m^* is the complex conjugate of E_m. The light intensities of the first few diffraction orders are shown in Fig. 8

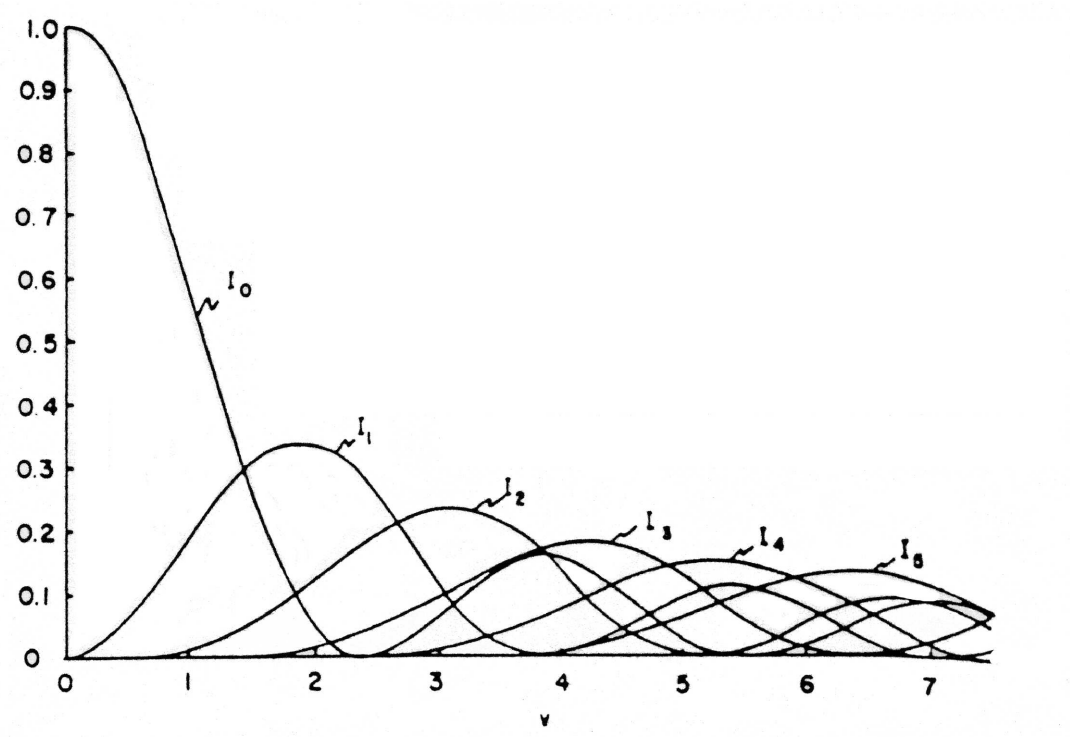

Figure 8: Light Intensities of several Fraunhofer orders versus the variable v=$k\, n\, L$ under Raman-Nath conditions. In the absence of modulation (v=0) 100% of the incident light is found concentrated in the zeroth order, which is completely quenched for v=2.4.

2.6.3 Case II:Bragg Diffraction

When the acoustic frequency is raised and $\theta_0 \simeq \pm\theta_B$, higher order diffraction is eliminated, and only two light beams, zeroth and first order, become predominant. In this case, for θ_0 close to $+\theta_B$, Eq. (2.46) reduces to

$$\frac{dE_0}{dz} = -\frac{\alpha}{2L}E_1 \tag{2.52}$$

and

$$\frac{dE_1}{dz} + j\frac{2\zeta}{L}E_1 = \frac{\alpha}{2L}E_0 \tag{2.53}$$

where

$$\zeta = K\,L\,(\sin\theta_0 - \sin\theta_B)/2\,\cos\theta_0 \tag{2.54}$$

Using the boundary conditions $E_0(0) = 1$ and $E_1(0) = 0$ the normalized intensities at z=L are

$$I_1 = 1 - I_0 = \left(\frac{\alpha}{2\sigma}\right)^2 \sin^2\sigma \tag{2.55}$$

where

$$\sigma^2 = \zeta^2 + \left(\frac{\alpha}{2}\right)^2 \tag{2.56}$$

When $\zeta = 0$, the incident light beam satisfies the Bragg condition and Eq. (2.55) reduces to a simple form

$$I_1 = \sin^2\left(\frac{\alpha}{2}\right) = \sin^2\left(\frac{k_f\,\Delta n\,L}{2\cos\theta_0}\right) \tag{2.57}$$

In the interests of historical accuracy the light intensities of the zeroth and first orders are plotted versus Q=$\frac{K^2L}{nk}$ at Fig. 9. The value of $\alpha = \pi$ was chosen, in which case the solutions predict that all light lies in the first order.

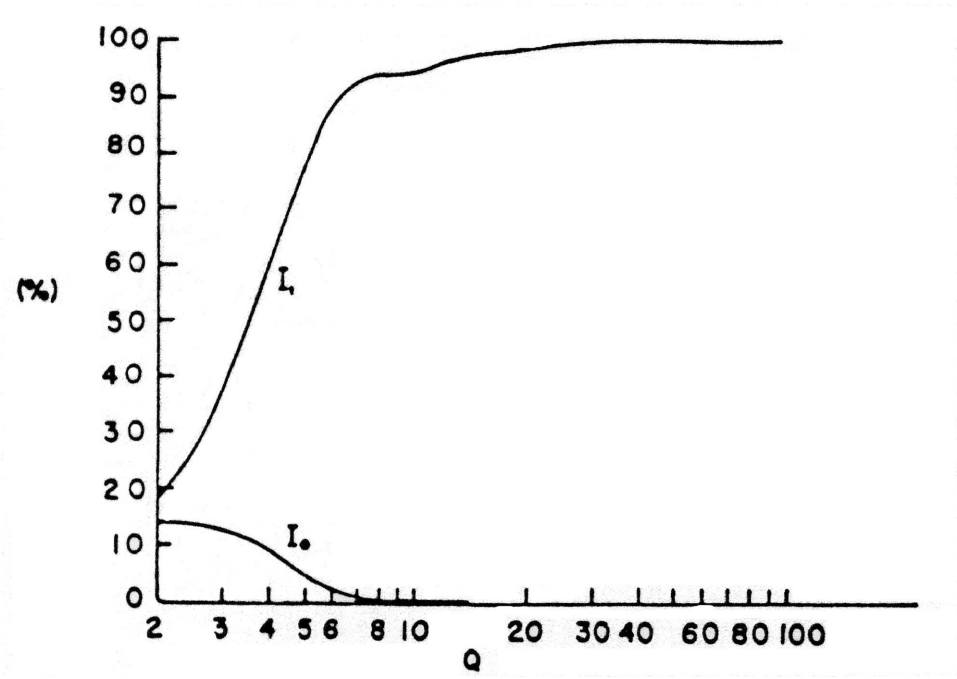

Figure 9: Zeroth and first order light intensities versus Q at Bragg incidence for $\alpha = \pi$.

2.7 Elasticity Theory

Under the influence of external forces, the distances separating the different material points in a medium become modified. It is then said that it has undergone a "deformation". Internal forces known as stresses will develop opposing the deformation of the solid body, and will tend to make it return to its initial shape and volume. A material is said to be elastic when, as the stresses reduce to zero, so does the deformation, which, in this case, constitutes a reversible state in the solid body.

A material can be elastic up to a certain value of strain, and cease to be so beyond that point. The relationship between stresses and strains for a given medium inside the elastic limit can differ according to the intensity of the strain. When the strains are weak enough, each component of a stress tensor is linear and homogeneous

function of all the components of the strain tensor. The set of all these relations are written compactly in tensor notation as follows:

$$T_{ij} = c_{ijkl} S_{kl} \tag{2.58}$$

This constitutes what is known as the generalized Hooke's law, which is an extension of the simple Hooke's law $T = E\,\partial u/\partial x$ with E being Young's modulus. The set c_{ijkl} constitutes a tensor of rank 4 known as the stiffness tensor. If u is the displacement from equilibrium of the particle, the equation of motion of each material particle is

$$\frac{\partial T_{ij}}{\partial x_j} = \rho \frac{\partial^2 u_i}{\partial t^2} \tag{2.59}$$

The combination of the two equations above brings us to the set

$$\rho \frac{\partial^2 u_i}{\partial t^2} = c_{ijlm} \frac{\partial}{\partial x_j} \left(\frac{\partial u_l}{\partial x_m} \right) \tag{2.60}$$

Thus a set of differential equations is obtained, which only involve the derivatives, and which governs the propagation of elastic waves which are also known as *acoustic waves*.

There are two kinds of strains propagating in an elastic medium. The so-called *extensional* or *longitudinal* or *compressional* strain for which its polarization is along the direction of propagation causing a displacement, $\hat{u} = \cos(\omega_a t - k_a y)\hat{y}$, along the direction of propagation (Fig. 10(b)) and the *shear* strain, for which polarization is normal to the direction of propagation, causes a displacement $\hat{u} = \cos(\omega_a t - k_a y)\hat{x}$ in that direction. Since there are two axes normal to the propagation axis, there are two shear strains available (Fig. 10(a),(c)).

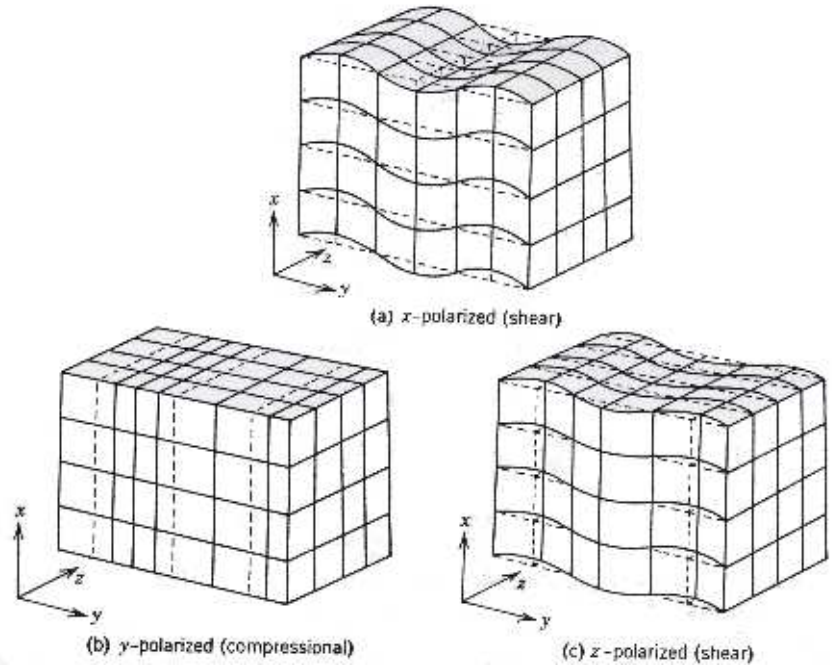

Figure 10: Grid diagrams for extensional(b) and shear(a,c) acoustic waves propagating along Y-axis.

2.8 Piezoelectricity

To describe generation and propagation of piezoelectrically induced acoustic waves the set of wave equations (2.60) needs to include the piezoelectric source

$$\rho\frac{\partial^2 u_i}{\partial t^2} - c'_{ijlm}\frac{\partial}{\partial x_j}\left(\frac{\partial u_l}{\partial x_m}\right) = -\frac{\partial}{\partial x_j}(e_{kij}E_k) \tag{2.61}$$

where u_i and E_k are the displacement and the driving electric field components, ρ is the material density, and e_{kij} and c'_{ijlm} are the components of the piezoelectric and the piezoelectrically stiffened elastic tensors, respectively. As far as the piezoelectric stiffening is concerned, it takes into account the electro-mechanical coupling between the acoustic and electric waves.

The source terms on the right side of equations (2.61) are given as the gradient

of the piezoelectrically induced stresses. Due to the sharp drop of these stresses at the boundary of the sample it follows that significant sources of acoustic waves are on the plane faces of the crystal sample. However, the electric field affects the crystal as a whole and bulk sound waves will also be created inside the crystal with the application of the electric field. In fact to create only surface waves, one needs to apply the electric field in specific resonance frequencies of the medium.

In a non-piezoelectric medium, the stress depends on the strain through the elastic tensor as shown in Eq. (2.58). In piezoelectric media, there appear supplementary stress components and the constitutive equations of piezoelectricity are written

$$T_{ij} = c_{ijkl}S_{kl} - e_{kij}E_k \tag{2.62}$$

$$D_i = e_{ikl}S_{kl} + e_{ik}E_k \tag{2.63}$$

The electric field E and the induction vector D must also satisfy Maxwell's equations. Given that the acoustic velocities are much slower than the velocity of electromagnetic waves, the quasi-static approximation may be used, where the magnetic quantities are considered as zero

$$\nabla \times \mathbf{E} = 0 \tag{2.64}$$

$$\nabla \cdot \mathbf{D} = 0 \tag{2.65}$$

which for a plane wave are written

$$\mathbf{E} \times \mathbf{s} = 0 \tag{2.66}$$

$$\mathbf{D} \cdot \mathbf{s} = 0 \tag{2.67}$$

where $\mathbf{s}$ is a vector in the direction of the wave propagation. Applying the equations

above to Eq. (2.63) one can define

$$c'_{ijkl} = c_{ijkl} + \frac{e_{mij}\, e_{nkl}\, s_m\, s_n}{\epsilon_{pq}\, s_p\, s_q} \tag{2.68}$$

where c'_{ijlm} is the piezoelectric stiffening tensor that in piezoelectric media couples stress and strain as follows:

$$T_{ij} = c'_{ijkl}\, S_{kl} \tag{2.69}$$

This leads to a very interesting expression that couples the electric field with the strain in the following way

$$\mathbf{E} = -\mathbf{s}\frac{e_{mkl}\, s_m\, S_{kl}}{\epsilon_{pq}\, s_p\, s_q} \tag{2.70}$$

Considering the plane boundary conditions, plane-wave solutions are assumed. With $j = m = 1, 2$ or 3, three independent sets of one-dimensional, coupled wave equations, representing waves that are generated on three pairs of opposite crystal faces, are derived. From the plane-wave solutions, the components of the strain tensor are calculated[37]

$$S_{lm} = \frac{1}{2}\left(\frac{\partial u_l}{\partial x_m} + \frac{\partial u_m}{\partial x_l}\right) \tag{2.71}$$

where $\partial u_m/\partial x_l$ is the gradient in the direction x_l of the displacement u_m projected along the direction x_m.

2.9 Photoelastic Effect

Suppose that a solid body undergoes a strain with components S_{kl} when under the effect of stress, which results in a change of the refractive index. The effect that couples the mechanical strain to the optical index of refraction is called *photoelastic*.

This change of index of refraction can be described in a tensor notation, analogous with the electro-optical description as follows

$$\Delta\left(\frac{1}{n^2}\right)_{ij} = p_{ijkl}S_{kl} \tag{2.72}$$

where $\Delta(1/n^2)_{ij}$ is the change in the optical impermeability tensor and S_{kl} is the strain tensor. Just like the EO effect, there are higher order terms involving higher powers of the strain tensor S_{kl} which are neglected, because these are small compare with the linear term which, unlike the EO effect, is always present and typically in the order of $\sim 10^{-5}$.

Since both $\Delta(1/n^2)_{ij}$ and S_{kl} are symmetric tensors, the indices i and j as well as k and l can be permuted. The permutation symmetry of the strain-optic tensor, p_{ijkl} is identical to that of the quadratic electro-optic tensor and the abbreviated notation S_j is derived from S_{kl} by the following rules:

$$\begin{aligned} S_{11} &= S_1 \\ S_{22} &= S_2 \\ S_{33} &= S_3 \\ 2S_{23} &= S_4 \\ 2S_{31} &= S_5 \\ 2S_{12} &= S_6 \end{aligned}$$

Notice the additional factor 2 in the abbreviation of what are often called "shear strains" $S_4 \rightarrow S_6$. Equation (2.72) then becomes

$$\Delta\left(\frac{1}{n^2}\right)_{i} = p_{ij}S_j \tag{2.73}$$

It has been shown by Nelson and Lax[38] that the formulation (2.73) is not sufficiently general to describe all acousto-optical phenomena. Specifically the case of shear waves in anisotropic media is not covered by the conventional description but since that case is not part of this study, the conventional description is going to be used.

The form, but not the magnitude, of the strain-optic coefficients p_{ij} can be derived from the symmetry of the crystal and for the case of $LiNbO_3$ it takes the form

$$p_{ij} = \begin{pmatrix} p_{11} & p_{12} & p_{13} & p_{14} & 0 & 0 \\ p_{12} & p_{11} & p_{13} & -p_{14} & 0 & 0 \\ p_{13} & p_{13} & p_{33} & 0 & 0 & 0 \\ p_{41} & -p_{41} & 0 & p_{44} & 0 & 0 \\ 0 & 0 & 0 & 0 & p_{44} & p_{41} \\ 0 & 0 & 0 & 0 & p_{14} & \frac{1}{2}(p_{11} - p_{12}) \end{pmatrix} \tag{2.74}$$

The equation of the index ellipsoid in the presence of a strain field for a $LiNbO_3$ crystal can now be written

$$\begin{aligned} x^2(\frac{1}{n_0^2} + p_{11}S_1 + p_{12}S_2 + p_{13}S_3 + p_{14}S_4) &+ y^2(\frac{1}{n_0^2} + p_{12}S_1 + p_{11}S_2 + p_{13}S_3 - p_{14}S_4) \\ + z^2(\frac{1}{n_e^2} + p_{13}S_1 + p_{13}S_2 + p_{33}S_3) &+ 2yz(p_{41}S_1 - p_{41}S_2 + p_{44}S_4) \\ + 2zx(p_{44}S_5 + p_{41}S_6) &+ 2xy(p_{14}S_5 + \frac{1}{2}(p_{11} - p_{12})S_6) = 1 \end{aligned}$$

2.10 Action of an Electric Field

In an optical medium that is both electro-optic and piezoelectric, like most electro-optic media are, the change in the index of refraction caused by the electric field is

$$\Delta\left(\frac{1}{n^2}\right)_i = p_{ij}S_j + r_{ij}E_j \tag{2.75}$$

But we also know that in piezoelectric media, for certain directions $\mathbf{s}$, there is a simultaneous propagation of a plane wave of deformation and of a longitudinal electric

field. The relation between the strain S_j and the electric field (Eq. 2.70) can be re-written as follows

$$\mathbf{E} = -\mathbf{s}\frac{e_{kj}\, s_k\, S_j}{\epsilon_{pq}\, s_p\, s_q} \tag{2.76}$$

If we substitute the E by the above expression to Eq. (2.75) we have

$$\Delta\left(\frac{1}{n^2}\right)_i = p'_{ij}\, S_j \tag{2.77}$$

where p'_{ij} is the photoelastic coefficients modified by the electro-optic effect and it is given by

$$p'_{ij} = p_{ij} - \frac{r_{ijk}\, s_k\, e_{mk}\, s_m}{\epsilon_{pq}\, s_p\, s_q} \tag{2.78}$$

What Eq. (2.77) implies is that when a sound wave propagates inside a photoelastic medium, then a change in the index of refraction of the medium occurs. As can be seen in Fig. 11, the passage of the sound wave in the medium produces an effect reminiscent of a diffraction grating.

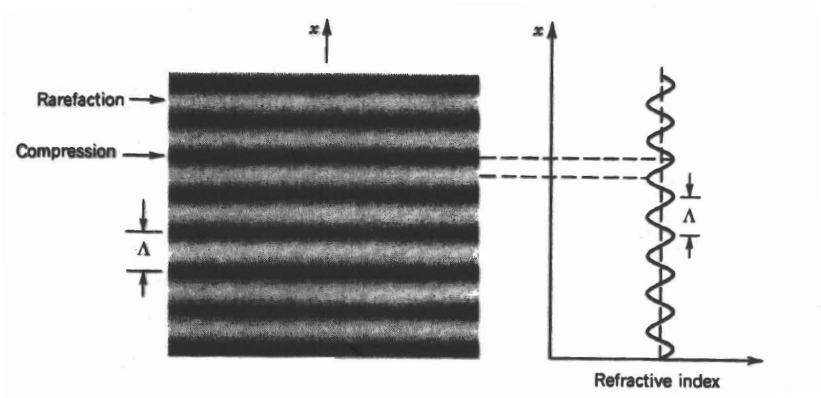

Figure 11: Index of refraction profile in a medium where a sound wave propagates. As can be seen, the sound wave produces an effect reminiscent of a diffraction grating in the medium.

2.11 Piezoelectric Generated Acoustic Waves in $LiNbO_3$

Since $LiNbO_3$ is both a piezoelectric and an electro-optic medium, the elastic tensor components are piezoelectrically stiffened (described at section 2.8) and the photoelastic coefficients are modified by the electro-optic effect (described at section 2.10). That makes analytical calculations cumbersome and the use of software simulations by a PC is preferred.

Optic-axes $LiNbO_3$ light modulator cuts, i.e. light propagating along the optic axis of the sample, are preferred to others because in this case, the light propagation is not affected by the natural birefringence. However, light modulation in optic-axis cuts (z-cut) may be considerably influenced by the strain-optic effect of a variety of acoustic waves generated piezoelectrically by electrical driving and this is the case of study in this section.

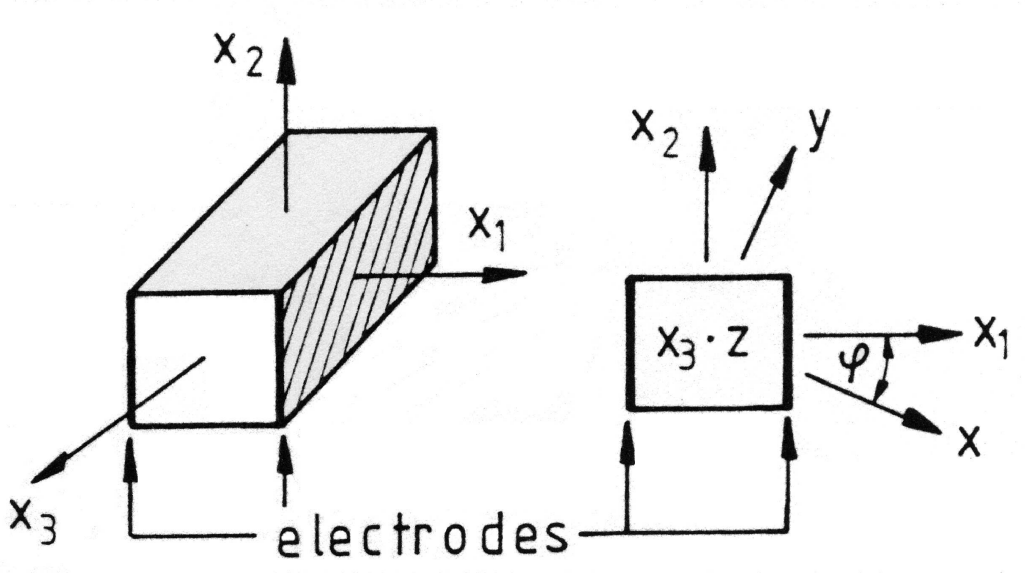

Figure 12: Acousto-Optic setup for generation and propagation of acoustic waves.

For a transversally driven optic-axis $LiNbO_3$ setup, like the one shown in Fig.

12, the only degree of freedom is the orientation of the electric field relative to the lateral faces. For that reason the angle ϕ was defined as the angle between the crystallographic x-axis and the electric field vector, **E**. A numerical analysis was performed[39] taking into account the piezoelectric stiffening of the elastic tensor components and electro-optic correction of the elasto-optic coefficients according to the actual propagation direction.

The results, presented in Fig. 13, show that for each pair of faces three plane acoustic waves, one extensional (C) and two shear (S_1 and S_2) can be generated with orientation-dependent amplitudes and velocities. Their velocities and induced birefringence are plotted in 2^0 steps and the graphs marked with DIRECT:1,2,3 represent the electroded (X_1), the lateral (X_2) and the aperture ($X_3 \equiv Z$) faces, respectively. Since the optic-axis of the $LiNbO_3$ crystal is an axis of threefold symmetry, the orientation dependence is given in the (0-120^0) range.

The bulk acoustic waves generated on the aperture (z-axis) faces is not of interest for diffraction modulation because the refractive index grating would be developed along the light propagation direction and can only cause a phase modulation. The highest birefringence which can cause amplitude modulation in an optic-axis cut is the S_1 shear wave on the x-axis at $\phi = 90^0$ which corresponds to applying the electric field to the y-axis.

As one can see in Fig. 13, for $\phi = 0^0$ the extensional acoustic waves of both x and y-axis do not induce any birefringence and so does the S_1' shear wave of y-axis. In this case, the small contribution of S_2 shear wave can be ignored and one need consider only contributions from S_1 and S_2'.

The velocity and induced birefringence for all 9 piezoelectrically induced acoustic

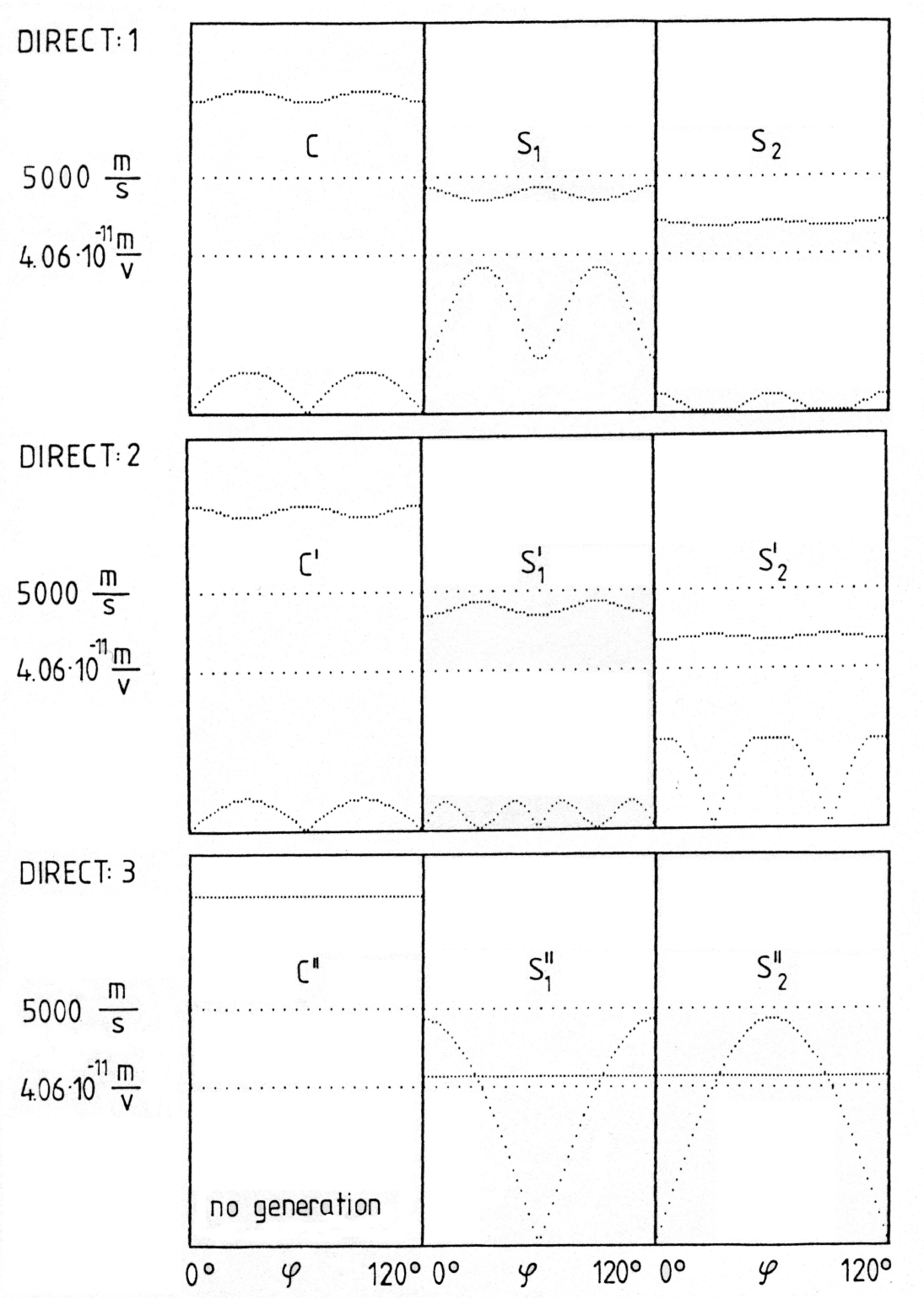

Figure 13: Two shear (S1,S2) and one extensional (C) acoustic waves can be piezoelectrically generated for each crystallographic axis in $LiNbO_3$ [39].

Cut and Acoustic Wave Mode	Velocity[39] (m/s)	Velocity[40] (m/s)±1%	Induced Birefringence at $\phi = 0^0$ ($10^{-11}\frac{m}{V}$)
X-E	6577	6572	0
X-Fast Shear	4782	4793	1.42
X-Slow Shear	4027	4079	0.41
Y-E	6800	6854	0
Y-Fast Shear	4500	4458	0
Y-Slow Shear	3967	3995	2.23
Z-E	7333	7316	0
Z-Shear	3583	3573	5.79
Z-Shear	3583	3573	0

Table 3: Acoustic wave velocities and induced photoelastic birefringence in $LiNbO_3$.

waves are presented in table 3, cited from various publications.

2.12 Bragg Polarization Effect

Standing-wave diffraction modulators based on the piezoelectrically induced strain-optic effect (PESO) have been known and implemented for a long time [41]. Various researchers[41, 43] have demonstrated orders of magnitude reduction of the half-wave voltage of an electro-optic modulator when driven at piezoelectric resonant frequency of the crystal. In contrast to the conventional acousto-optic modulators, the crystal of such a PESO modulator serves as both the transducer and the resonance body of acoustic waves. However, these modulators have not been used as practical devices probably due to their non-uniform transmission and the modulation at discrete and relatively low frequencies in the kHz range.

It is generally known[44] that Bragg diffraction from a transverse acoustic wave propagating in an anisotropic medium, has the property that the diffracted light is polarized at right angles to the polarization of the incident light. However, in Bragg diffraction there are two diffracted light beams (one up-shifted and one down-shifted

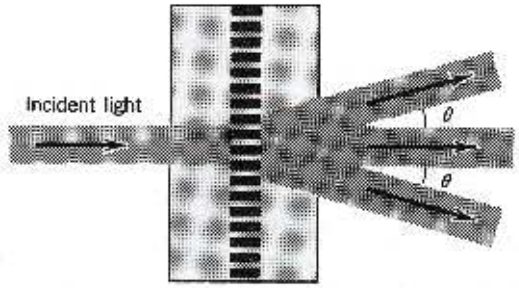

Figure 14: Bragg diffraction from transverse acoustic waves.

in frequency), as can be seen in Fig. 14, and these two are in anti-phase[48] their polarization is mutually canceled. In that case, if the phase of the carrier (undiffracted light) is changed by 90^0 with respect of that of the side bands, then amplitude modulation occurs since the polarization doesn't cancel any more. Specifically, a quarter-wave plate oriented with one of its principal axes parallel to the polarization of the incident light, will cause the desired 90^0 differential phase delay. For a complete intensity modulation setup, an analyzer follows which transmits a common polarization component and final demodulation takes place in a subsequent photodetector (see Fig. 15).

Under certain conditions[45, 47], this may happen even in optically isotropic media when $p_{11} \neq p_{12}$. A typical experiment which exhibits this "orthogonal" diffraction in an isotropic medium is shown in Fig. 15. A longitudinal sound wave (S_1) travels in the X direction and the light is incident in approximately the Z direction (assume the Bragg angle to be very small in this experiment). It is polarized in the X′ direction at 45^0 to the X and Y axes.

Considering the components E_x and E_y, it is clear that different strain optic coefficients must be applied to their respective interactions. For example in a $LiNbO_3$

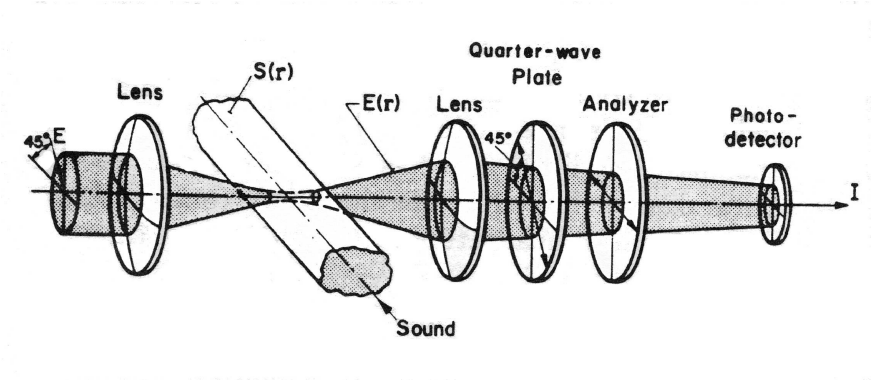

Figure 15: Arrangement for demodulation of the sampling light beam by means of a quarter-wave plate and an analyzer.

medium, from Eq. (2.75) it is readily seen that p_{11} applies to E_x ($\Delta n_x = \frac{1}{2} n_0^3 p_{11} S_1$), and p_{12} applies to E_y ($\Delta n_y = \frac{1}{2} n_0^3 p_{12} S_1$). Assuming weak Bragg diffraction we find, from Eq. (2.57), that diffracted light components are

$$\begin{aligned} E'_y &\simeq \frac{1}{4} j\, k_f\, S^*\, E_y\, n_0^2\, p_{12}\, L \\ E'_x &\simeq \frac{1}{4} j\, k_f\, S^*\, E_x\, n_0^2\, p_{11}\, L \end{aligned}$$

where we assume that the interaction is sufficiently weak that the sine function may be replaced by its argument. It is seen readily that, with respect to the Y′ and X′ axes, the components of the scattering light $\mathrm{E}_{x'}$ and $\mathrm{E}_{y'}$ depend on $p_{12} + p_{11}$ ($\Delta n_{x'} = \frac{1}{4} n_0^3 (p_{12} + p_{11}) S_1$) and $p_{12} - p_{11}$ ($\Delta n_{y'} = \frac{1}{4} n_0^3 (p_{12} - p_{11}) S_1$), respectively.

$$\begin{aligned} E'_{y'} &\simeq \frac{1}{8} j\, k_f\, S^*\, E_0\, n_0^2\, (p_{12} + p_{11})\, L \\ E'_{x'} &\simeq \frac{1}{8} j\, k_f\, S^*\, E_0\, n_0^2\, (p_{12} - p_{11})\, L \end{aligned}$$

so the diffracted light has both polarization components present.

However, if a shear wave is used, the ordinary component may be eliminated. Thus if in Fig. 16 the sound is in the form of a shear wave with particle motion

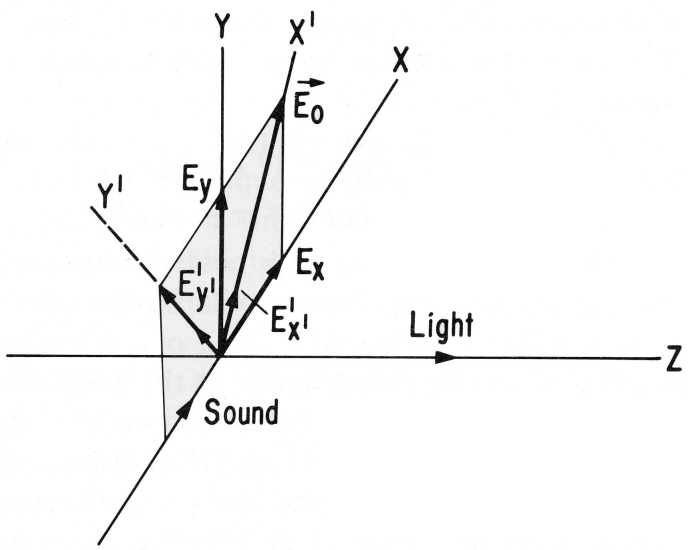

Figure 16: Coordinate system used in calculation of orthogonal diffraction. The incident light E_0 is polarized along X′ and the light propagation is along Z. The sound wave propagation is along X.

(polarization) in the Y direction (S_6) then, according to Eq. (2.75), the indicatrix changes from a sphere to an ellipsoid with axes along X′, Y′ and Z. Specifically the index ellipsoid is

$$\frac{x^2}{n_0^2} + \frac{y^2}{n_0^2} + xy(p_{11} - p_{12})S_6 = 1$$

In order to make this an ellipse again we need to apply a rotation of $\phi = 45^0$ about the Z axis and we find that

$$\begin{aligned} \Delta n_{x'} &= \frac{1}{4} n_0^3 [p_{11} - p_{12}] S_6 \\ \Delta n_{y'} &= -\frac{1}{4} n_0^3 [p_{11} - p_{12}] S_6 \end{aligned} \tag{2.79}$$

It is now clear that incident light with polarization along X′, such as shown in Fig. 16, will not give rise to cross polarization terms. However, if the incident light is polarized in the X or Y direction, the situation as regards orthogonal diffraction is analogous

to the longitudinal wave with the light polarized along X′. We find, however, one important difference. Due to the opposite sign of the coefficients in equations (2.79) the diffracted light with polarization along X cancels and we are left with polarization only along Y.

To summarize the above argument, in the case of a shear wave (S_6) propagating along the Y axis and incident light propagating along the Z axis, with polarization along the X axis, a diffracted light beam is produced which propagates also along the Z axis, with polarization along the Y axis (90^0 to the undiffracted light). So even in an isotropic medium one can have "orthogonal" diffraction if $p_{11} \neq p_{12}$ which is the case of a z-cut $LiNbO_3$ crystal.

Thus, using a z-cut $LiNbO_3$ in a setup like the one shown in Fig. 15 the polarization effects will cause amplitude modulation. The total light intensity arriving at the photodiode is[48]

$$I = \frac{\pi\, C\, e\, \eta}{h\, c} \int S(\mathbf{r})\, I_0(\mathbf{r})\, \mathrm{d}\tau_{\mathbf{r}} \tag{2.80}$$

where $C = n^2 p$ is a strain-optic constant, η is the photodiode quantum efficiency, e is the electron charge, h is Planc's constant, and $\mathbf{r}$ is the point of light diffraction in the crystal. It is interesting to note from Eq. (2.80) that the current I is a measure of the total integrated peak change of stored electromagnetic energy within the interaction region. In other words the sound field is sampled, in amplitude and phase, with a "probing" function $I_0(\mathbf{r})$. Thus, the current, I, represents a moving amplitude image of the sound field within the probed area.

An experimental verification of the above was performed[48] using the arrangement described in Fig. 15. Eight PZT transducers were arranged in a linear way operating at 40MHz and the light beam was tightly focused to much less than the

sound wavelength. Thus, to scan the sound field, the acousto-optic modulator was mechanically moving along the optic axis of the crystal. As can be seen in Fig. 17, the sound field was successfully scanned with high resolution. The triple-peaked appearance of each sound beam was attributed to a near-field characteristic in the region of the focused light beam.

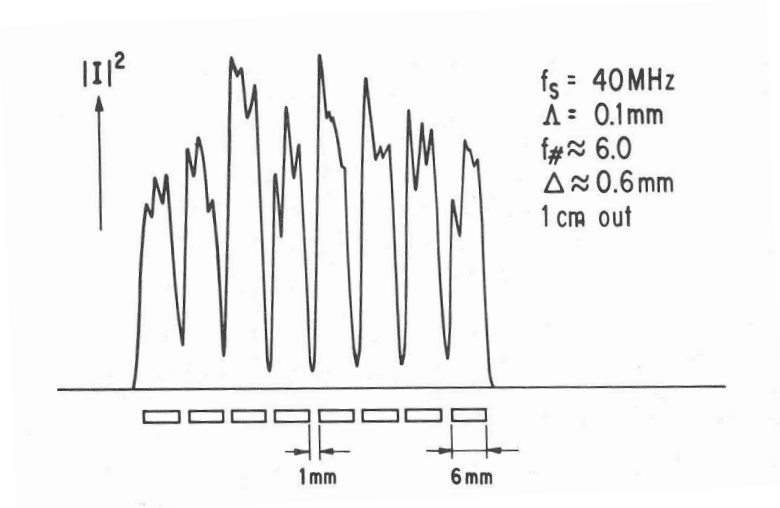

Figure 17: Experimentally determined sound field distribution within the acousto-optic modulator.

In conclusion, the experiment described above corroborates the theoretical predictions expressed in Eq. 2.80.

2.13 Attenuation of Acoustic Waves in $LiNbO_3$

The most general way of introducing acoustic loss into the piezoelectric elastic equations is to derive a perturbation formula, in which the viscosity tensor η_{ijkl} is considered as a perturbation of the elastic tensor and the dielectric losses tensor ϵ''_{ij}

is considered as a perturbation of the dielectric tensor in the following way

$$\begin{aligned} c'_{ijkl} &= c_{ijkl} + j\omega\eta_{ijkl} \\ \epsilon'_{ij} &= \epsilon_{ij} - j\epsilon''_{ij} \end{aligned}$$

A general expression for the attenuation constant is then derived[40]

$$\alpha_M = \frac{\omega^2}{2\,\rho\,v_p^3}\left(U^M n : \eta : nU^M + \frac{n\cdot\epsilon''\cdot n(n\cdot e : nU^M)^2}{\omega(n\cdot\epsilon'\cdot n)^2}\right) \tag{2.81}$$

where the first term is the component of effective viscosity tensor η_{eff} arising from elastic losses due to interactions of acoustic and thermal phonons. The second term represents dielectric losses via the piezoelectric coupling but this term is small compared with acoustic losses.

The viscosity tensor, η, has the same symmetry as the elastic tensor, c, so it has six independent constants for the crystal class 3m where $LiNbO_3$ belongs.

	i=1	2	3	4	5	6
j=1	0.6547	0.2275	0.2499	-0.0687	0	0
j=2	0.2275	0.6547	0.2499	0.0687	0	0
j=3	0.2499	0.2499	0.3377	0	0	0
j=4	-0.0687	0.0687	0	0.1765	0	0
j=5	0	0	0	0	0.1765	-0.0687
j=6	0	0	0	0	-0.0687	0.2136

Table 4: The viscosity tensor of lithium niobate in units of $10^{-3} N\,m^{-2}\,s$

When the values of effective viscosity η_{eff}, presented in table 4, are substituted in Eq. (2.81) along with the mode displacements U^M, we find its values along with the attenuation constant for each acoustic wave.

Cut and Acoustic Wave Mode	Equation for η_{eff}	η_{eff} $(10^{-3} N\, m^{-2}\, s)$	α_0 (dB/cm)±8% at 1 GHz
X-E	η_{11}	0.6760	0.8789
X-Fast Shear	$-0.9904\eta_{14} + 0.5689\eta_{44} + 0.4311\eta_{66}$	0.2467	0.8169
X-Slow Shear	$0.9904\eta_{14} + 0.4311\eta_{44} + 0.5689\eta_{66}$	0.1229	0.6610
Y-E	$0.9864\eta_{11} - 0.2316\eta_{14} + 0.0136\eta_{44}$	0.6399	0.7255
Y-Fast Shear	$0.0136\eta_{11} + 0.2316\eta_{14} + 0.9864\eta_{44}$	0.1802	0.7416
Y-Slow Shear	η_{66}	0.2196	1.2546
Z-E	η_{33}	0.3455	0.3220

Table 5: Equation and calculation for the effective viscosity η_{eff} and the attenuation constant for each acoustic wave generated in $LiNbO_3$ X and Z-axis.

These are posted in table 5, where the attenuation constant is given at $f = 1GHz$ but since their dependence is quadratic in f ($\alpha_o \sim f^2$), one can scale it to any frequency. Using that information, one can calculate the presence of each wave in the crystal from the moment of creation. For example, let us calculate the time of presence for the X-axis fast shear wave inside a $LiNbO_3$ crystal. From table 5 we find that the attenuation of that wave is

$$0.8169 \cdot f^2 \, \frac{dB}{cm} \tag{2.82}$$

where dB is the decibel which is defined as

$$dB \;=\; 20 \log \left(\frac{I_{max}}{I_{min}} \right)$$

For a signal of dynamic range 20:1 (or 2000% modulation) Eq. 2.82 becomes

$$0.8169 \cdot 26.02 \, \frac{f^2}{cm} = 21.26 \, \frac{f^2}{cm}$$

and multiplying the above with the X-FS sound wave speed, found in table 3, to transform space to time we get

$$21.26 \cdot 4793 \frac{m}{sec} \, \frac{f^2}{cm} \Rightarrow 10188100 \, f^2 \, \frac{1}{sec} \Rightarrow \frac{9.82\, 10^{-8}}{f^2} sec \tag{2.83}$$

which translates to 425ps signal duration for a 15.2GHz sound wave. Of course we have to take into account the errors in the measurement of the attenuation of speed, which the authors estimate about 10%, so that a sound wave of that frequency will have a presence time in the range of 383-467ps.

Chapter 3

Use of the Electro-Optic Effect to Detect Charge Particle Beams

3.1 Introduction

When a charged particle is at rest then the electric field is isotropically distributed around the particle, as pictured in Fig. 1, but when the charged particle is in relativistic motion, then the electric field contracts, producing an anisotropically directed radial field, orthogonal to the charged particle propagation direction[49].

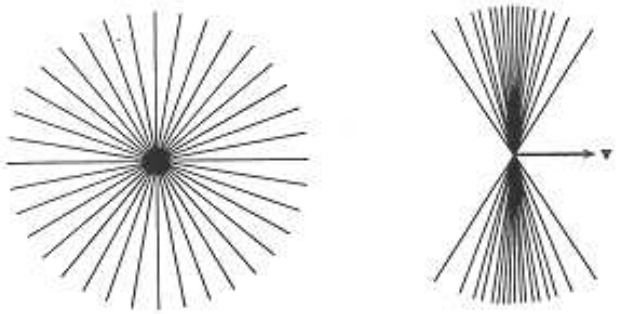

Figure 1: Lines of electric field for a particle at rest and in relativistic motion.

At relativistic speeds, when $\gamma \gg 1$, the transverse electric field becomes equal to γ times its non-relativistic value. However, its duration is decreased, by the same factor, and the charged particle electric field exists only for a time

$$\Delta t \simeq \frac{r}{\gamma v} \tag{3.1}$$

where **r** is the transverse distance from the charged particle path to the position of measurement of the electric field, v is the particle velocity and γ its relativistic

kinematic factor. So as γ increases, the amplitude of the field increases in proportion, but its duration decreases by the same proportion. The time integral of the fields times v is independent of velocity as one can see at Fig. 2 .

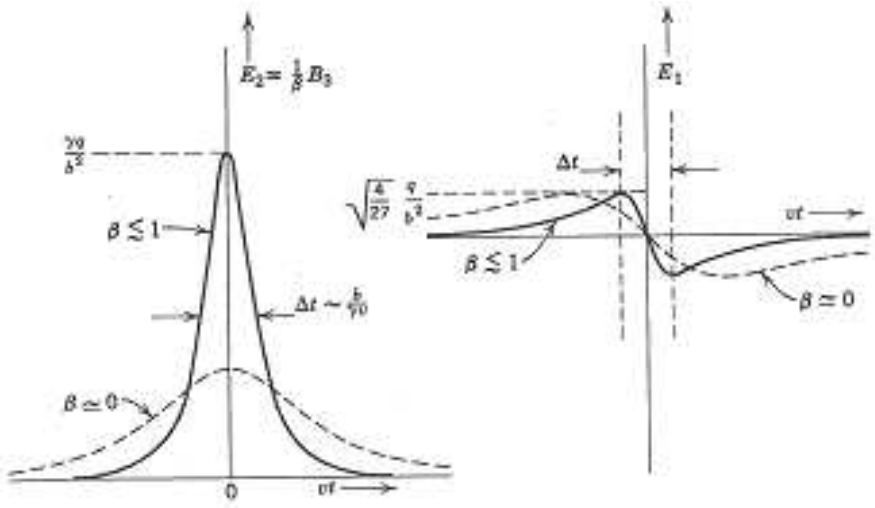

Figure 2: The transverse and longitudinal electric field of a relativistic moving charged particle. The longitudinal electric field has a zero time integral.

3.2 Detection of Relativistic Charged Particles using the Electro-Optic Effect

In the previous chapter we saw how we can use the electric field to change the index of refraction of an EO crystal and thus the polarization of light. In the same way the electric field of a relativistic charged particle can be used as means of detection of a particle and time-resolved measurements of charged particle beam bunches. The retardation in this case would be

$$\Gamma_i(t) = \frac{\omega}{c} \Delta n_i(t) \cdot \ell = \frac{2\pi}{\lambda} \Delta n_i(t) \cdot \ell \tag{3.2}$$

where ℓ is the length of the crystal in the direction of the laser beam path , λ is the wavelength of the laser beam and $\Delta n_i(t)$ is the time-dependent change of index of

refraction in the i-th direction and is equal to

$$\Delta n_i(t) = -\frac{1}{2}\, n_i^3\, r_{ij}\, E_j(t) \tag{3.3}$$

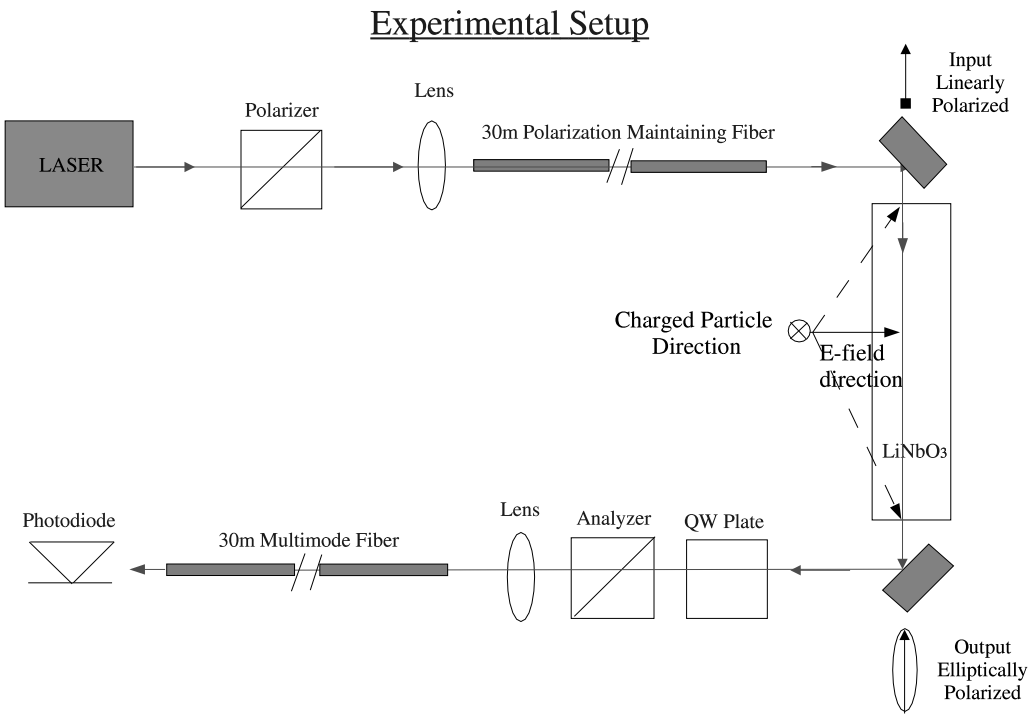

Figure 3: An detection scheme for charged particles. It employs the transverse EO effect and the charged particle propagates normal to the crystal and the laser light path.

A detection scheme using the EO effect can be employed as shown in Fig. 3 shows. The laser light goes through a polarizer to ensure that the light is linear polarized and then it is coupled to a Polarization Maintaining (PM) fiber (see **Appendix C** for more details). This way the light can be safely and easily directed on the EO crystal which is placed underneath or above the charged particle path. This

arrangement implements what is called transverse EO effect where the electric field from the charged particles is applied normal to the crystal and the direction of laser light propagation. Then, according to Eq. 3.2, when the particle passes it introduces to the light a retardation which is converted to intensity modulation by an ellipsometer placed right after the crystal. Then the light is coupled into another PM fiber to be delivered to a photodiode. The waveform is recorded using a waveform digitizer.

There are many variations of the above charged particle detection scheme that one could employ like, for example, having many of them in series to monitor the particle trajectory or coupling the light into the EO crystal using only lenses. One should choose the appropriate detection scheme, evaluating the pros and cons in relation to the goals of the experimental setup.

Only by looking at equation (3.2), which describes the EO induced retardation at the crystal (from the charged particle), one can see some of the advantages of this method over the conventional method described in section 1.2:

• The detection is not destructive to the charged particle. The particle passes at a distance **r** from the EO crystal. As a result, a real time monitor and feedback system can be constructed. Of course, the electric field magnitude also depends on the distance and it drops very fast ($\sim \frac{1}{r^2}$) so one needs to design the experimental setup carefully.

• The dependence of the retardation on the electric field is linear so both the sign and the magnitude of the charge of a particle can be detected or if the charge is known, then its radial distance **r** can be found.

• It is an all-optical method, which means low noise (using a laser with noise suppression circuit), and a low number of expensive electronic read-out systems, since

each signal can be delayed using a low dispersion optical fiber (eg. single mode), large frequency response, etc.

3.3 Measuring Temporal Profile of Charged Particle Beam Bunches

The electric field induced inside the crystal by a charged particle beam, in the approximation of small beam dimensions compared with distance from the crystal, is

$$E_i(t) \simeq \gamma \frac{1}{4\pi\varepsilon_r \varepsilon_0} \frac{Nq}{r^2} T(t) \tag{3.4}$$

where γ is the relativistic Lorentz factor, N the number of charged particles in the beam, q the particle charge, T(t) the temporal charge distribution, ε_0 the permittivity of free space, ε_r the dielectric constant of the EO crystal in the direction the electric field is applied, and r the radial distance of the charged particle beam from the optical beam.

Since the Coulomb field of a relativistic charged particle beam is directed perpendicular to the beam trajectory, an electro-optic sensor can be constructed to measure its temporal profile. As pictured in Fig. 4, an EO crystal is located between an ellipsometer (this is the name given to a combination of a polarizer, quarter-wave plate and analyzer) making a transverse EO modulator where the sensor (EO crystal) is perpendicular both to the charged particle beam path and the laser beam path.

But this electric field is present only for a limited time Δt (Eq. 3.1) and we know that the retardation is induced only in the presence of the electric field, therefore, instead of the length ℓ (in Eq. 3.2) we should use whatever is smaller:

- The physical length (ℓ) of the crystal in the direction of laser beam path or
- The effective length (ℓ_{eff}) which is the distance light travels inside the crystal

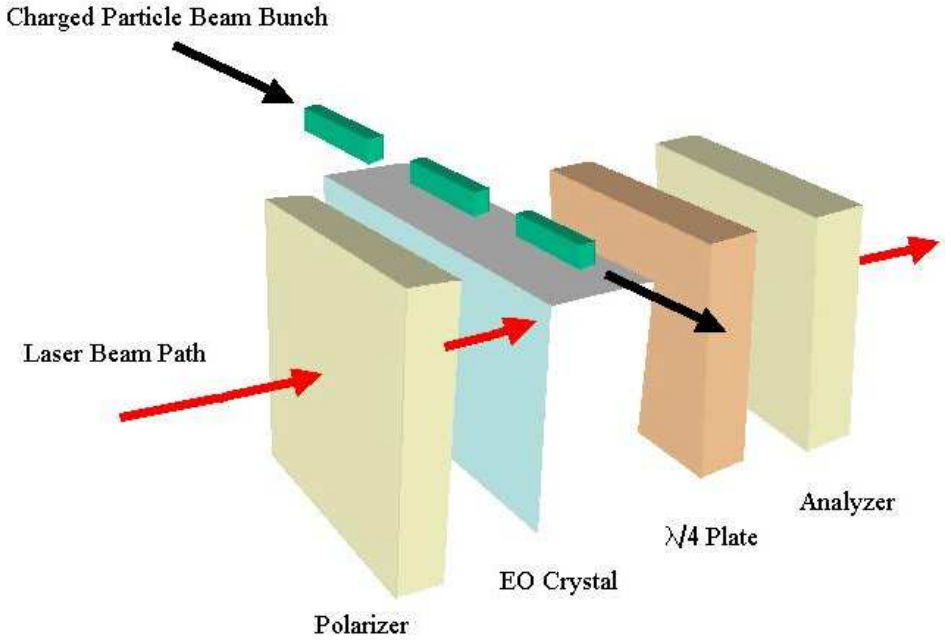

Figure 4: The charged particle beams pass above an EO sensor consisted from a polarizer, EO Crystal, quarter wave plate and an analyzer.

during the time Δt the field is present and is given by

$$\ell_{eff} = \Delta t \times \frac{c}{n_k} \simeq \frac{r}{\gamma n_k} \tag{3.5}$$

where n_k is the index of refraction of the crystal in the direction of laser beam propagation and at the laser wavelength in use.

Substituting (3.5), (3.4) and (3.3) to Eq. (3.2) gives

$$\begin{aligned} \Gamma(t) &= \frac{2\pi}{\lambda}\frac{1}{2} n_i^3 r_{ij} E(t)\,\ell \simeq \frac{\pi}{\lambda} n_i^3 r_{ij} \frac{1}{4\pi\varepsilon_0}\frac{\gamma N_e q T(t)}{\varepsilon_r r^2}\frac{r}{\gamma n_k} \\ &\simeq \frac{\pi}{4\lambda\varepsilon_0\varepsilon_r n_k}\frac{Q T(t)}{r} n_i^3 r_{ij} \end{aligned} \tag{3.6}$$

where n_i is the index of refraction in the direction of the applied electric field.

Now it is interesting to take a moment to notice that in the equation above:

• There is no γ dependence in the final induced retardation. Although the electric field of relativistic charged particles increases by the relativistic kinematic factor (γ), its time duration decreases by the same factor and they cancel each other.

• The linear dependence of our signal with the beam charge Q. This makes possible the detection of the sign of the particle beam charge along with its magnitude.

• The induced retardation has a $\frac{1}{r}$ dependence and not the $\frac{1}{r^2}$ dependence of the Coulomb field.

• The $\frac{1}{\varepsilon_r}$ dependence favors the use of EO materials with small dielectric constant (for example EO polymers).

As we discussed in Chapter 2 (section 2.5 on p. 17) the induced retardation (Eq. 3.6) needs to be converted to an intensity modulation which can be easily measured, for example, by a photodiode and a waveform digitizer. Looking at Eq. 2.16, on page 18, we realize that in order to obtain the highest intensity modulation, the polarization has to be at 45^0 with respect the axes of the crystal. Then we realized that there are two methods to choose from: the electro-optic amplitude modulation at 50% intensity transmission point and the near zero optical bias point. Depending on the detection scheme, only one of the above methods is the optimum.

For example a 0.5nC electron beam, 2mm away from a $LiNbO_3$ crystal, will induce a retardation which depends on the orientation of the crystal axes.

• For a x or y-cut $LiNbO_3$ crystal with the electric field applied on the z-axis and using a 514nm laser

$$\Gamma(t) = \pi \left(n_e^3 \, r_{33} - n_0^3 \, r_{13}\right) \frac{Q \, T(t)}{4 \, \varepsilon_0 \, \varepsilon_r \, n \, r \, \lambda} = 49.2 mrad \tag{3.7}$$

• For a z-cut $LiNbO_3$ crystal with the electric field applied on the x-axis and using

a 514nm laser

$$\Gamma(t) = 2\pi\,(n_0^3\,r_{22})\,\frac{Q\,T(t)}{4\,\varepsilon_0\,\varepsilon_r\,n\,r\,\lambda} = 19mrad \tag{3.8}$$

The expected retardation is bigger when the electric field is applied on the z-axis but the external field doesn't rotate the index ellipsoid so we have to rotate the input polarization 45^0 with respect the axes of the crystal. In that case the residual birefringence of $LiNbO_3$ degrades the polarization purity down to about $\sim 5 \cdot 10^{-3}$ so that the use of near zero optical bias point is not the optimum. On the other hand, the 50% intensity modulation method, which is discussed in detail in section 2.5.1 on page 20, gives in this case a maximum modulation in the order of $\sim 10^{-2}$ (look at Eq. 2.27 on page 22). When the detection scheme is a photodiode with an oscilloscope, then the biggest signal is wanted and the huge dc that the signal is riding can be ignored and applying the field on the z-axis is the optimum case. But when using instruments with limited dynamic range like CCD camera or Streak Camera (SC), then one is looking for the biggest modulation and applying the field on the z-axis is not favored.

Applying the external electric field on the x-axis of the $LiNbO_3$ crystal causes a rotation of the index ellipsoid by 45^0 for the x and y axes (as proved in section A.3 (Eq. A.32) on page 132) so the input polarization needs to be aligned with one of the crystal axes before the electric field is applied. In that case, there is no residual birefringence since both axes have the same index of refraction and the polarization purity is high (about $5 \cdot 10^{-4}$) and the 50% intensity modulation method is not the optimum. This time, the case of near zero optical bias point, discussed in detail in section 2.5.2, is the optimum and the maximum modulation is on the order of $\sim 10^{-1}$ (see Eq. 2.36 on page 24) which is about one order of magnitude bigger modulation

than the first method. That is the optimum case for limited dynamic range detection schemes like CCD camera or Streak Camera.

The appropriate choice of crystal orientation depends solely on the experimental goals.

3.4 The Accelerator Test Facility at BNL.

The experiment used a 45 MeV electron beam provided by the Accelerator Test Facility (ATF) located at Brookhaven National Laboratory (BNL). A drawing of the ATF layout and its beam lines is shown in Fig. 5.

A 5 MeV electron beam from a rf photocathode gun was injected into a linac to boost its energy to 45 MeV. The final beam contained up to 0.8nC charge in a focused diameter of about 0.5mm in about 15ps duration at a repetition rate of 1.5Hz.

3.5 Proof of Principle

In order to demonstrate the simplicity of our method and establish the proof of principle, we used a commercially available $LiNbO_3$ electro-optic modulator from Uniphase Telecommunications Products (UTP). As can be seen in Fig. 6(a), the $LiNbO_3$ electro-optic modulator is coupled to polarization maintaining fibers of 4 microns diameter designed to maintain and propagate the polarization of infrared light. In order for the EO modulator to be used in the high vacuum environment of the ATF facility to detect electron beam bunches, we had to minimally modify its housing. First we opened the case (Fig. 6(b-c)) and then we opened a small passage of about $\sim$ 1mm to the left of the crystal (Fig. 6(d)) for the beam to pass without hitting the housing. Then the modulator was mounted on an aluminum bar and the fibers were locally stripped and epoxied on a standard $2\frac{3}{4}$ inch vacuum flange to create

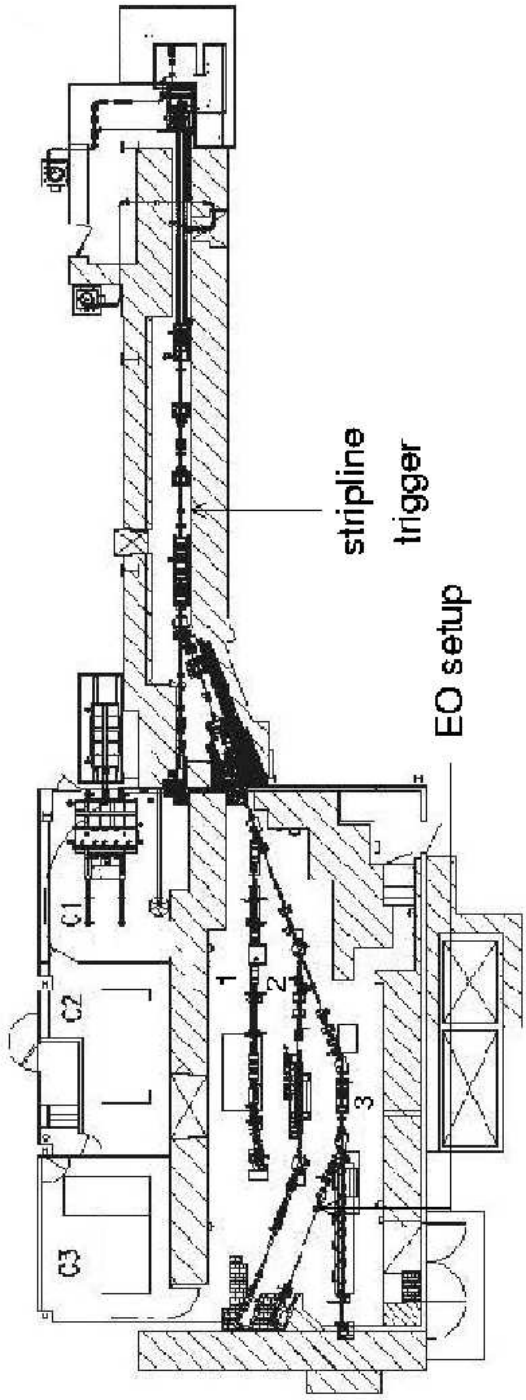

Figure 5: The layout of Accelerator Test Facility (ATF). The experiment was located at beamline 3A (angled branch of beamline 3) and the stripline trigger was upstream.

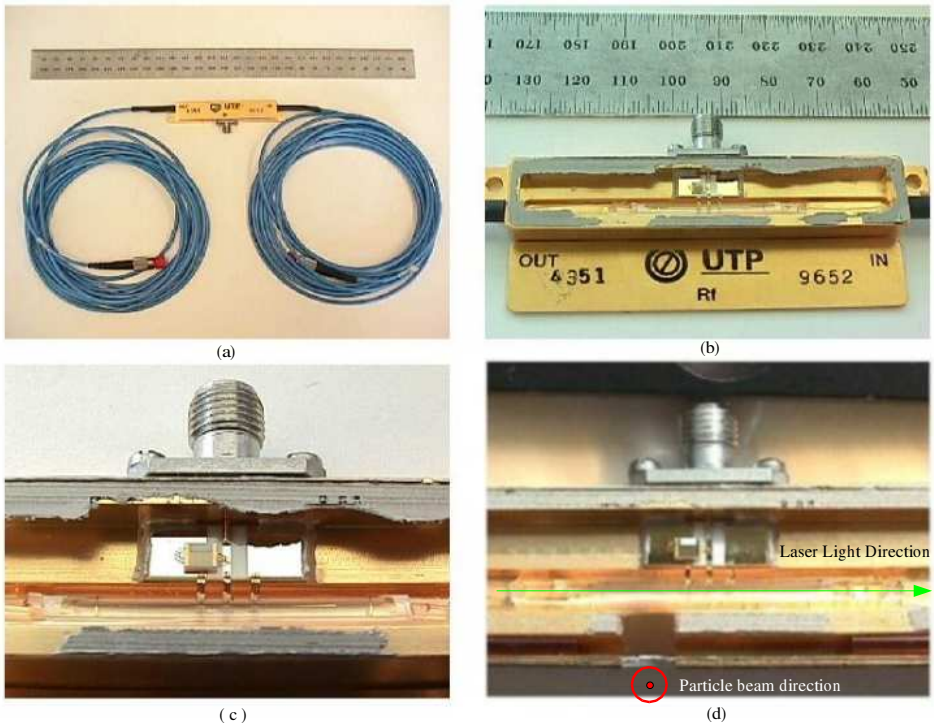

(a) (b) (c) (d)

Figure 6: The UTP EO modulator: (a) as received, (b)-(c) opened, (d) minimally modified to allow the passage of charged particle beams.

a high vacuum fiber feedthrough not available commercially. Then the modulator was installed on a six-way vacuum cross, located on beamline 3(a)(see Fig. 5) of the ATF facility which provided 45 MeV electron beam bunches of $\sim$ 15ps and $\sim$ 1nC of charge. The electron beam direction was normal to the crystal and the laser light propagation direction creating a transverse EO sensor (Fig. 6(d)).

For light source we used a continuous wave (CW) infrared laser from AMOCO at 1320nm, capable of 20mW output power but during our experiment the maximum output power was 10mW. The laser was located at the control room of ATF but using a 35m polarization maintaining fiber the light was transferred into the experimental hall. The polarization of the light exiting the AMOCO laser was very well defined (

extinction ratio was less than 5 10^{-4}) and no polarizer was needed to further linearize the polarization (see Fig. 3). The light exiting the UTP modulator was transferred out of the experimental hall using another 35m polarization maintaining fiber and then with the help of lenses it passed through a quarter-wave ($\lambda/4$) plate and a analyzer to translate the induced retardation to intensity modulation (see section 2.5). The polarization purity after the light passage through the $LiNbO_3$ crystal degraded to about 5 10^{-3} due to residual birefringence. Finally the light was coupled to a 45GHz photodiode (New Focus, Model 1015) and pre-amplifier. Then the signals were digitized in a 7GHz oscilloscope (Tektronix SCD5000) and stored in memory.

The maximum modulation of the light intensity (displayed in Fig. 7) was about $\sim 9\%$ of its DC level [14, 15]. The electron beam was about $\sim$ 5mm away from the crystal with a charge of about 1nC. The rise time of the signal is about $\sim$ 120ps limited possibly not by the electronics but from the capacitance of the metallic housing where strong electric fields (wakefields) are created from the passage of the electron beam and the sudden change of the electric field boundary conditions. That is probably also the reason for the long tail that follows the EO signal.

Using the same UTP EO modulator at the LEAF Facility (located also at Brookhaven National Lab) we were able to reproduce the results but this time not in a high vacuum environment but in air. LEAF provided a $\sim$ 10MeV electron beam containing up to 2nC charge in about $\sim$ 30ps bunches in $\sim$ 4mm diameter and with a repetition rate of 10Hz.

The experimental setup is similar to the one used at the ATF facility. For light source we used the same AMOCO laser (cw, $\sim$10mW @ 1320nm) and a 20m polarization maintaining fiber transfered the light to the UTP modulator inside the

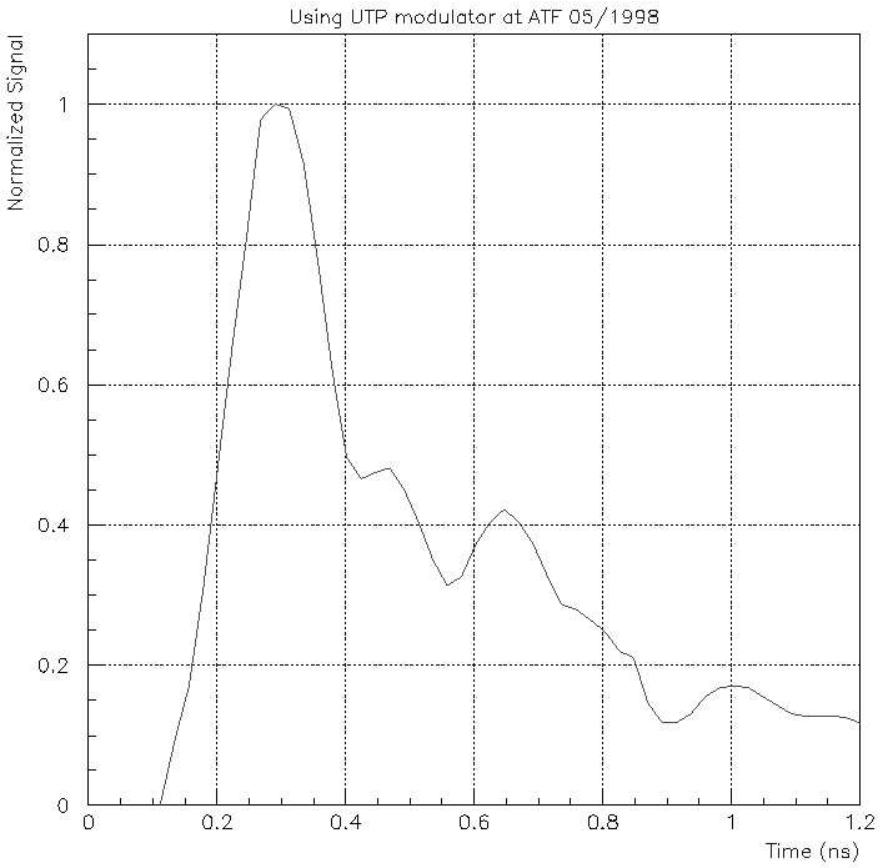

Figure 7: A single shot Electro-optic signal from the May 1998 run at the ATF (BNL) facility. The electron beam was about $\sim$ 5mm away from the crystal.

experimental hall. Since we were in the air, 3 step motors were used to give x, y and ϕ translation to the modulator for more accurate measurements. As can be seen in Fig. 8, the electron beam propagation was normal to the crystal and the laser light propagation was just like in the ATF. Finally the light was transferred with another 20m PM fiber to the control room, where using lenses the light passed through a quarter-wave ($\lambda/4$) plate and an analyzer to end in the 1GHz photodiode(New Focus model 1611) and 20GHz amplifier (New Focus model 1422).

The signal was digitized in the 7GHz oscilloscope (Tektronix SCD5000) and is

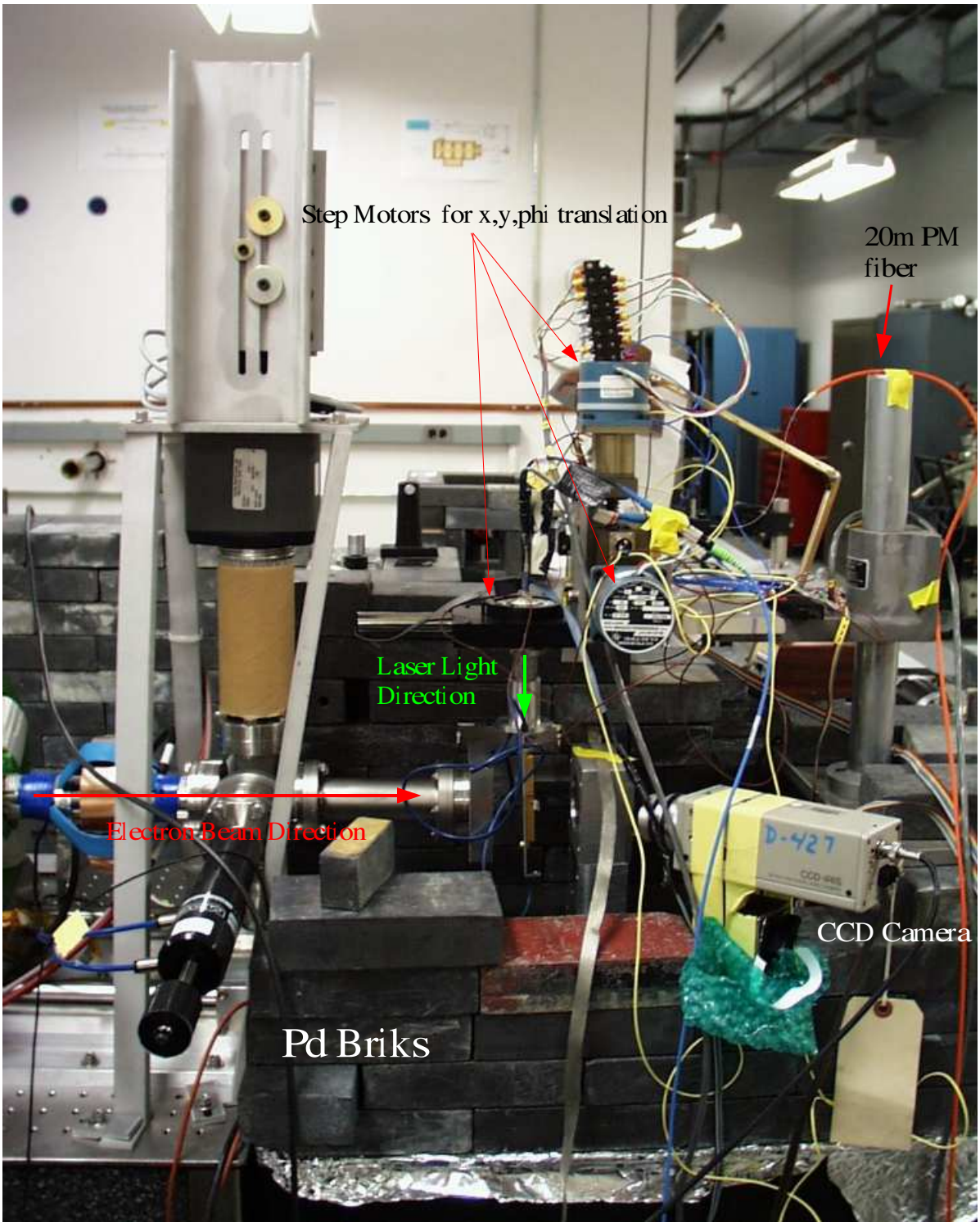

Figure 8: The UTP electro-optic modulator setup at LEAF (BNL) facility. In addition to previous similar measurements x,y and ϕ translators were installed.

Figure 9: The EO signal obtained at LEAF facility (08/1999) using a 1GHz photodiode, 20GHz amplifier and a 7GHz oscilloscope. The electron beam was about 10mm away from the crystal.

displayed in Fig. 9. It has similar structure and risetime to the ATF observed signal but is inverted because of the amplifier.

3.6 Free-Space Electro-optic Sensor

It was realized previously that if the electro-optic crystal has any metallic housing it induces wakefields which affect and limit our measurement. Thus a custom electro-optic sensor had to be constructed which is not available commercially.

A high vacuum compatible electro-optic modulator setup was constructed using discrete optical components mounted on a aluminum bar anchored to a standard $2\frac{3}{4}$

inch O.D. vacuum flange, see Fig. 10. Two polarization maintaining fiber collimators were used to transfer the light in and out of the vacuum. The collimators are commercial products that provided a beam diameter of 0.5mm at the position of the crystal with small divergence ($< 0.3^0$ full angle) and insertion losses ($< 0.5dB$). As one can see in figure 10, the fibers were stripped locally and epoxied on a standard $2\frac{3}{4}$ inch vacuum flange to make a high vacuum fiber feedthrough which is not commercially available. After the input collimator, where the polarization was physically rotated 45^0 to the azimuthal, is a z-cut $LiNbO_3$ crystal which is sitting on a ceramic base with a 6.35mm clearance hole at the center for the electron beam to pass through. The ceramic base allowed us to avoid any induced wakefields in the vicinity of the sensor.

The 45^0 facet of the base is covered with fluorescent material for guiding the electron beam through the clearance hole. A CCD camera viewed the fluorescence due to the electron beam from directly above the setup. After the crystal, a Quarter Wave Plate (QWP) and an analyzer were installed and finally the light was coupled to a PM fiber collimator to transfer the light outside the vacuum.

A 45^0 pop-up flag with the same fluorescent material was located 23 cm down stream of the EO sensor setup and a CCD camera directly above the flag was connected to a computer frame grabber for precise electron beam location and profile measurements. A 35m polarization maintaining fiber was used to transfer the light outside the experimental hall, to the control room, where light was directed to a photodiode connected to an oscilloscope. The light source was a fiber-coupled, diode pumped, solid state, Nd:Yag laser (Coherent Laser Inc.), emitting a maximum of 250mW of continuous wave (CW) optical power at a wavelength of 1319nm. The

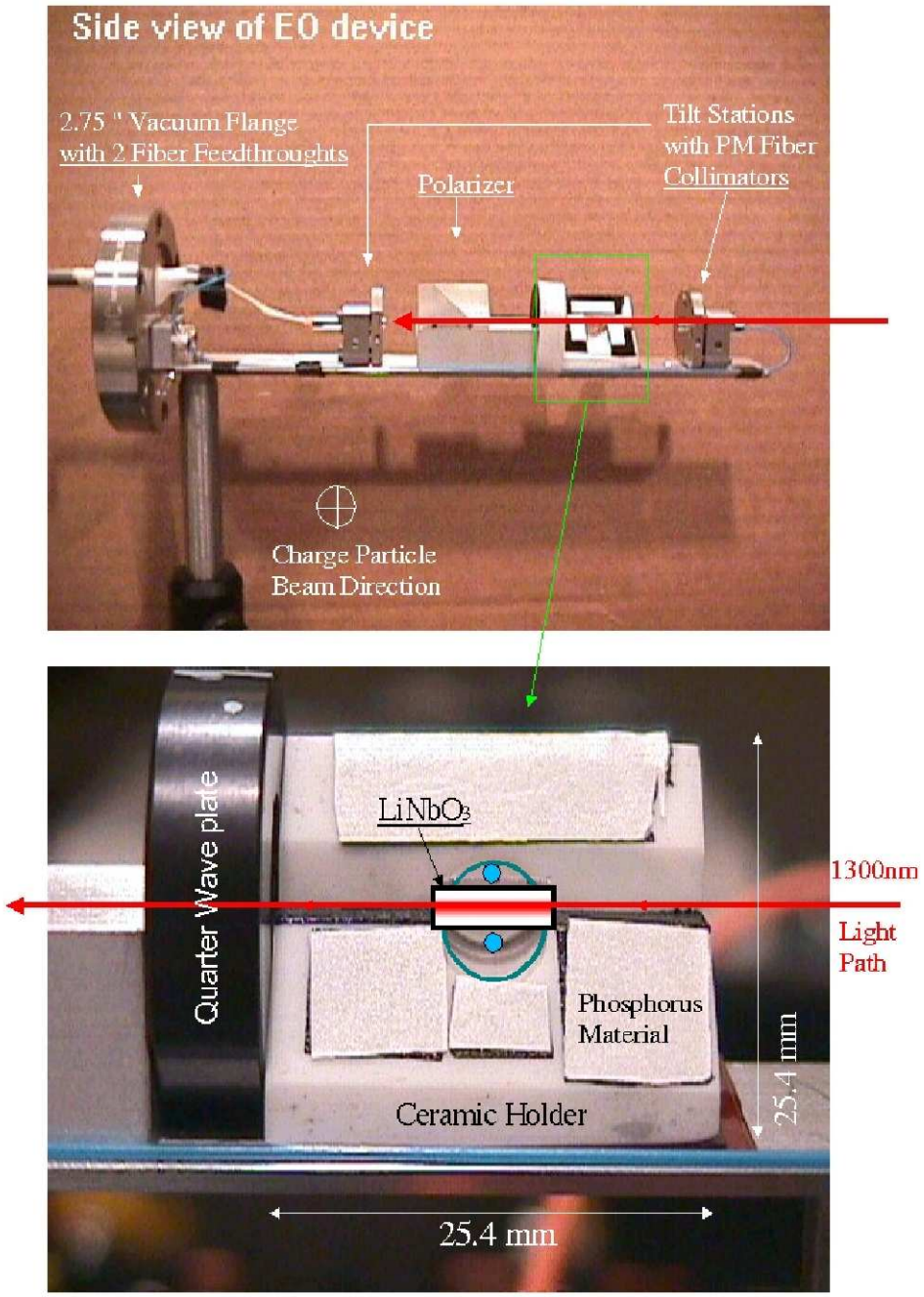

Figure 10: The First compact, high vacuum compatible, electro-optical beam sensor. The complete setup was designed to fit into a conventional 1.37 inch I.D. 6-way cross.

laser incorporated active noise suppression electronics to remove the relaxation oscillation noise. As can be seen in Fig. 11, at 1MHz the laser noise reaches already

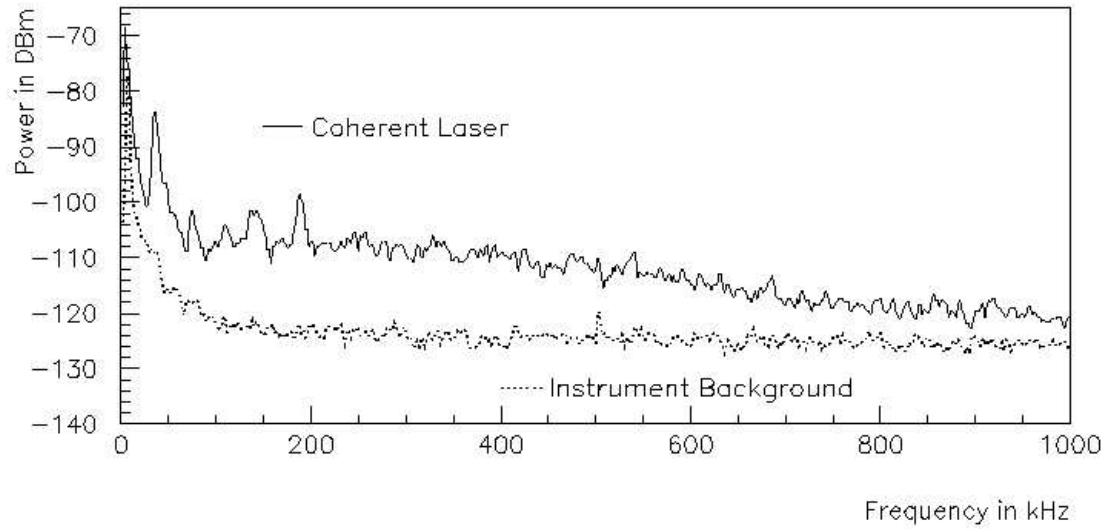

Figure 11: The laser noise of the diode pumped, Nd:Yag, laser at 1319nm from Coherent Laser Inc. A 7.1GHz spectrum analyzer was used along with a 12GHz photodiode.

close to the shot-noise limit, and beyond 5 MHz the laser noise was 1dB above the shot-noise. The polarization purity of the light source had an extinction ratio of $< 10^{-4}$ at the output end of the Polarization Maintaining (PM) fiber. With the light polarization going at 45^0 inside the crystal, the extinction ratio dropped to $\sim 10^{-2}$ because of the residual birefringence. The size of the lithium niobate crystal was (X $\times$ Y $\times$ Z) = 1 $\times$ 6.5 $\times$ 2.2 mm with z-axis (extraordinary) being aligned azimuthally, the x-axis parallel to the electron beam propagation direction, and the y-axis being the direction of laser beam propagation (see Fig. 12). In other words, the described EO sensor exploits the transverse electro-optic effect with the electric field applied at the z-axis where the biggest signal is expected. To linearize the modulation and

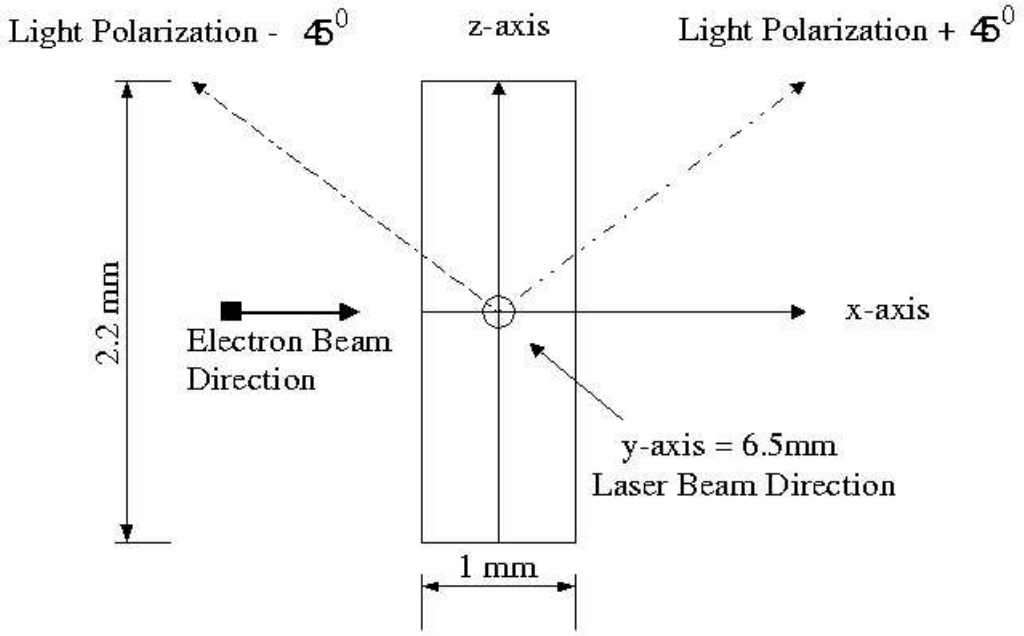

Figure 12: The $LiNbO_3$ installation orientation. The electric field from the charged particle beam is applied to the z-axis. Light propagates along the y-axis.

balance the residual birefringence of the $LiNbO_3$ crystal, the $\frac{\lambda}{4}$ waveplate was adjusted so that the EO system was optically biased at the quadrature point (50 % transmission point). Therefore, the resulting electric-field-induced signal constantly rode on a large dc light level. The analyzer was crossed polarized with respect to the input polarization. The total light transmission of the EO setup was about 12%, with typically 5mW of optical power reaching the photodiode.

3.7 Results

The very first action was to confirm the electron beam induced EO signal by a series of control experiments:

(1) No photons with wavelengths other than the input laser were received by the photoreceiver. Such photons may originate from nonlinear optical processes as well

as transition or Cerenkov radiation.

(2) The EO signal vanished in the absence of either the electron beam or the laser beam.

(3) The signal polarity changed sign when the direction of the electron field was reversed by moving the beam above and below the EO crystal, and

(4) when the input laser polarization was rotated by 90^0, as indicated in Fig. 12 , using a 90^0 keyed fiber-optic coupler.

An electron beam that is steered in symmetric positions of 1mm above and below the EO crystal produces an electric field that is of the same magnitude but opposite direction. Because of the linear dependence of the EO effect with the electric field one expects that reversing the field would result in reversal of the signal polarity which is illustrated in Fig. 13(a) and was observed in Fig. 14(a). Also one expects a similar polarity flip when the input polarization was changed from $+45^0$ to -45^0 because the operating point in the transmission curve changes as Fig. 13(b) shows. Specifically, when the EO modulator is operated on the positive slope of its response function, the polarity of the modulated signal follows the input polarity. However, when the operation moves to the negative slope of its response function, that is equivalent to switching the input polarization from $+45^0$ to -45^0, as shown at Fig. 13(b), the polarity of the modulated signal becomes opposite to the input. That is also what was observed experimentally, as can be seen in Fig. 14(b) when the input polarization was changed from $+45^0$ to -45^0 by using the 90^0 keyed fiber-optic coupler. The polarity reversal provides conclusive evidence of the signal being electro-optical in origin.

Next the EO signal dependence on the electron beam charge was investigated. The electron beam charge was varied by adjusting the UV intensity irradiating the

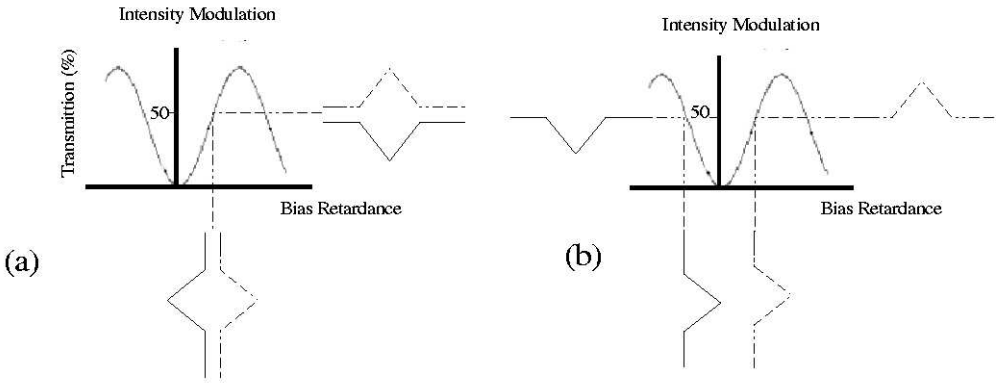

Figure 13: (a) Polarity flip due to change of the polarity of the signal and (b) Polarity flip when the input polarization is rotated by 90^0 from $+45^0$ to -45^0.

photocathode of the 5 MeV rf electron gun. The actual charge was measured by a Faraday cup located before the linac and also by a stripline detector after the linac (as shown in Fig. 5). For each charge value, 6 EO traces were collected and their averages are shown in Fig. 15 for the total of 5 different charge values. The electron beam position was locked at 1.17 mm away from the laser beam path and it clearly passed below the EO crystal unobstructed.

Then the maximum amplitude of the averaged trace for every charge value is plotted in Fig. 16 and each vertical error bar is the standard deviation for the set of six traces, while each horizontal error bar is the fluctuation of the charge readout from the Faraday cup and the stripline. The straight solid line is the χ-square linear fit which takes into account the errors in both coordinates and gives a reasonable integral probability of 38.6% which means that our linear fitting function is a good approximation to the parent function. .

But we should stop and ask whether the fitting procedure to the data is justified and whether, indeed, there exists a linear relationship between the measured charge

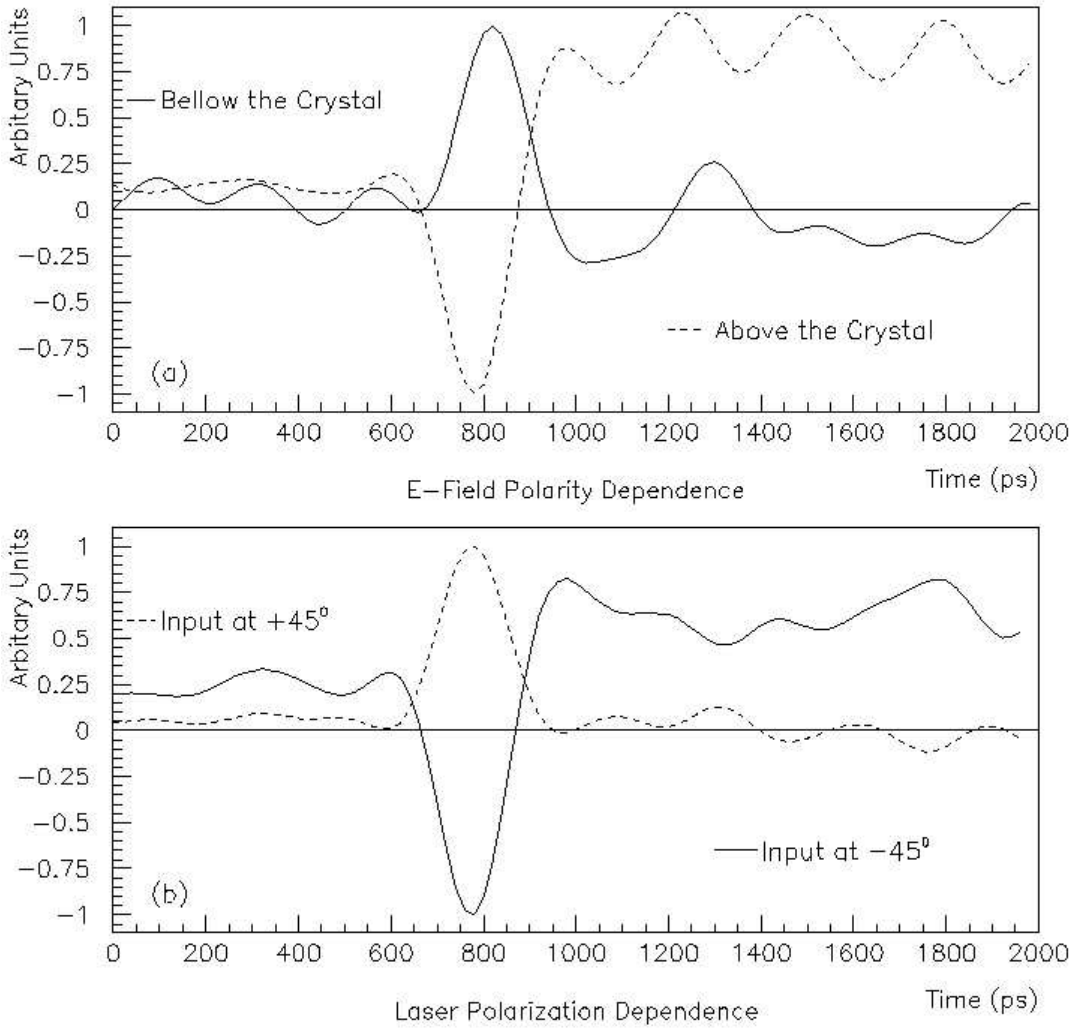

Figure 14: (a) EO signal polarity reversal due to electric field direction reversal when the charged particle beam is steered above or bellow the crystal and (b) EO signal polarity flip due to 90^0 rotation of the input laser beam polarization and the subsequent change of operation point in the transmission curve.

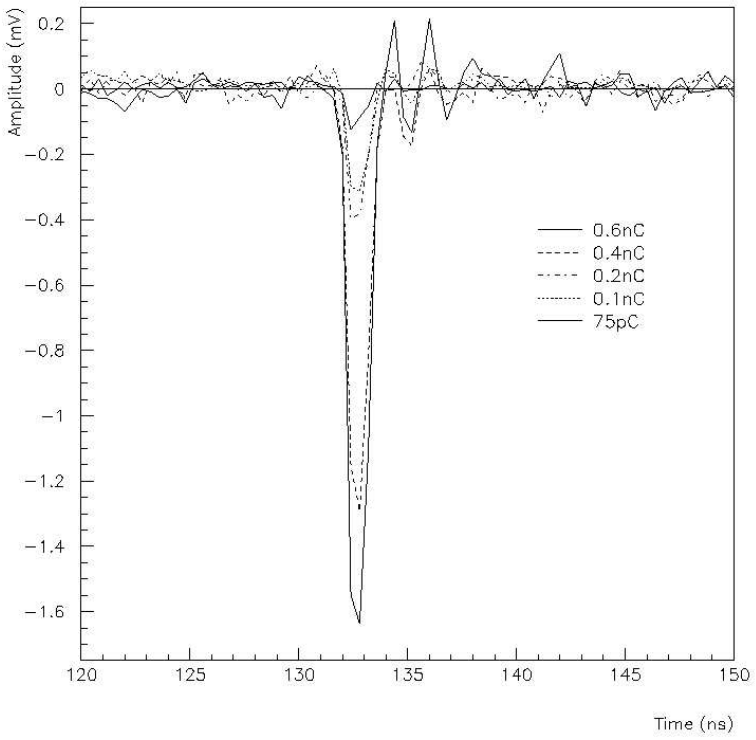

Figure 15: The average of 6 electro-optical traces is plotted for each electron beam charge. where each vertical error bar displayed is the standard deviation of the 6 signal traces and each horizontal error bar is the fluctuation of the charge in each position as measured by the Faraday cup and the pickup electrode combined. The electron beam position was locked at 1.17 mm away from the laser beam path and it clearly passed below the EO crystal unobstructed.

and the measured EO signal amplitude. To answer that question the linear-correlation coefficient r can be used for a quantitative measure of the degree of correlation or the probability that a linear relationship exists[50]. The value of r ranges from 0, when there is no correlation, to ± 1, when there is complete correlation. For the data shown in Fig. 16 the linear-correlation coefficient is $r = 0.9916$ and the probability that any random sample of uncorrelated experimental data points would yield an experimental linear-correlation coefficient like this is 0.1%. Thus a linear dependence of the EO signal with beam charge was established.

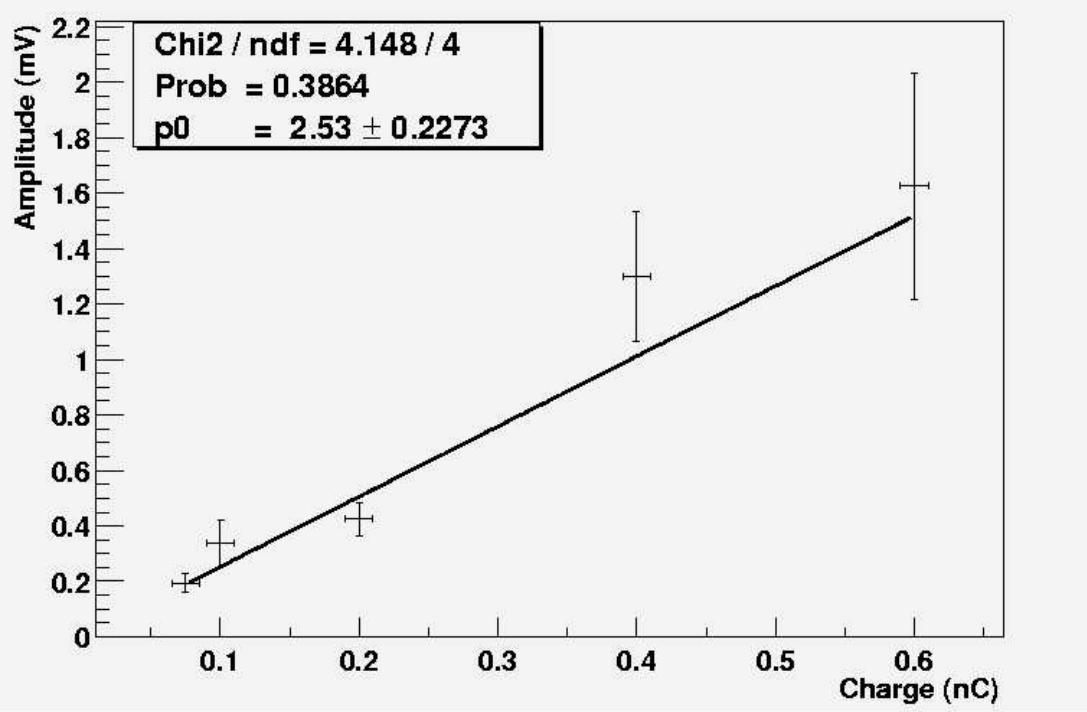

Figure 16: The electro-optical signal dependence on electron beam charge. The solid line is the fit performed.

The EO signal dependence on the electron beam position was also investigated. The electron beam was steered vertically, in the direction of the z-axis of the crystal, toward the crystal (from bellow) but not traversing it. In Fig. 17 you can see the electron beam profiles as viewed at the calibrated pop-up flag located 23cm behind the EO sensor. The center of the laser beam path was set at z=0mm because it is the distance of the electron beam from the laser beam path that goes into the EO equation 3.6. The laser propagated at the y-axis direction and the electron beam propagated at the x-axis direction of the crystal axis.

Taking advantage of the 6.35mm diameter clearance hole (black circle in Fig. 17) we collected a set of 5 traces at each electron beam position, ranging from 2.78mm to

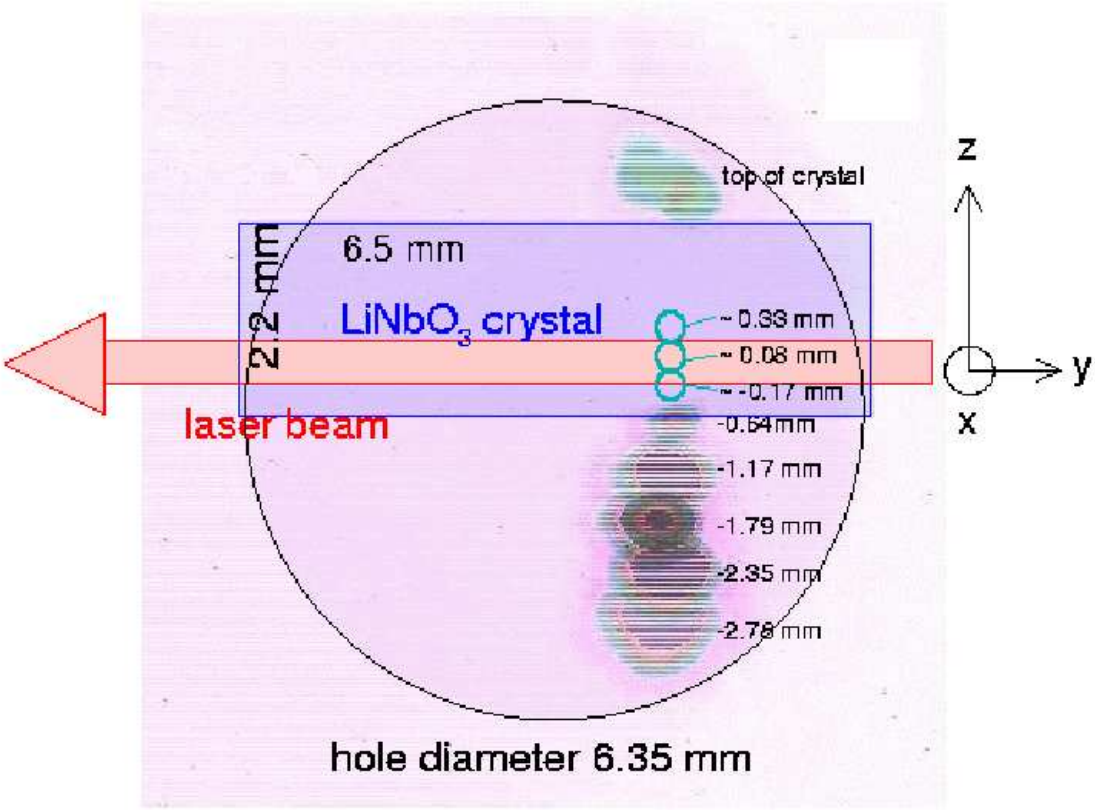

Figure 17: Schematic drawing of the $LiNbO_3$ crystal setup. The laser beam propagates in the direction of the y-axis of the crystal and the electron beam propagates in the direction of the x-axis of the crystal. The beam was moved along the z-axis of the crystal to study the dependence of the signal to the distance from the electron beam path. Several representative electron beam profiles and their location with respect to the laser beam position, assumed at z=0mm, are overlaid to show the maneuver of the beam relative to the crystal as view from a calibrated pop-up flag 23cm behind the EO sensor. Three electron beam positions were blocked by the EO crystal did not show up clearly on the pop-up flag but are illustrated in the figure by their beam positions relative to the laser beam path. Their approximate positions were determined by the pitching current of the dipole magnet.

0.64mm in steps of about 0.5mm for a total of 5 positions. The maximum amplitude of the average of all 5 traces collected for each position is plotted in Fig. 18 against the measured distance from the center of the laser path. The vertical error bars are the standard deviation for the set of 5 traces.

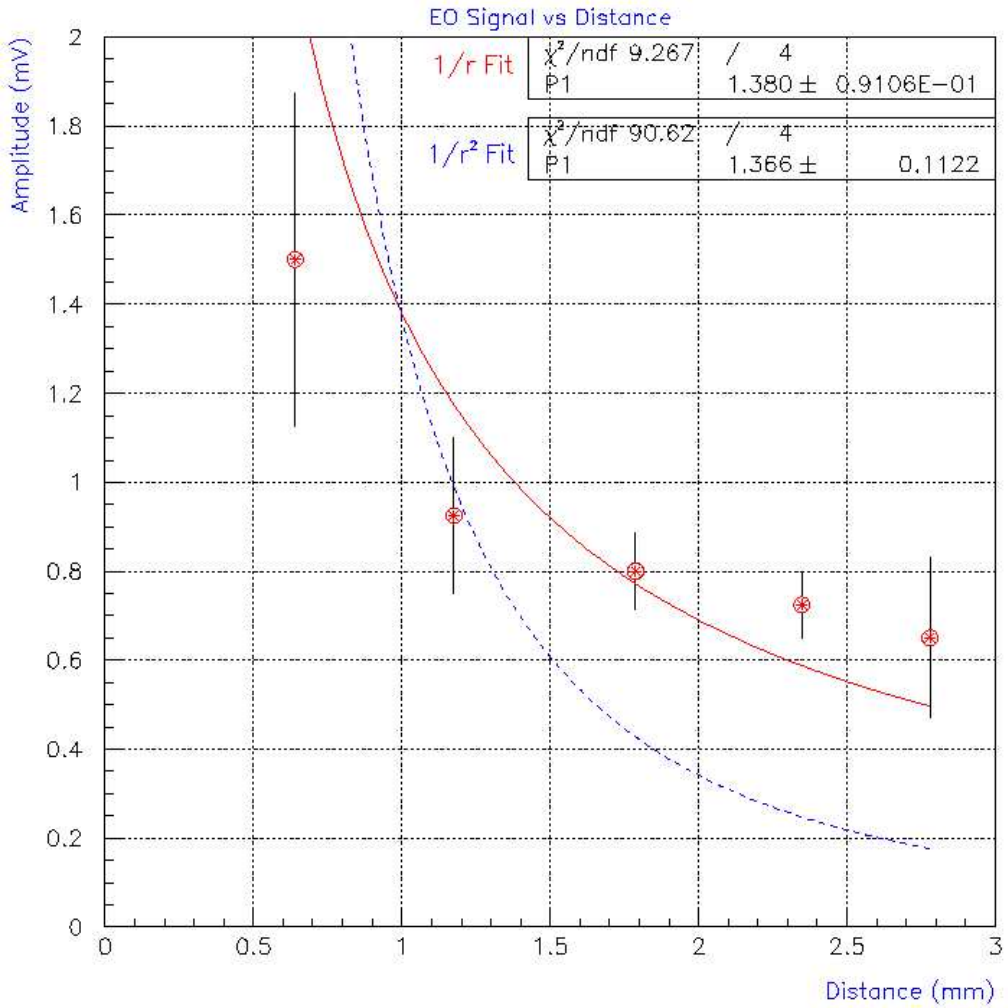

Figure 18: The maximum amplitude of the average is plotted with respect the distance from the center of the laser beam path. The solid line is a $\frac{1}{r}$ χ-square fit and the dashed line is a $\frac{1}{r^2}$ χ-square fit.

The solid line in Fig. 18 is a $\frac{1}{r}$ χ-square fit which has the relative high but still

acceptable χ-square per degree of freedom of $\chi_\nu = 2.3$ and for a sample with 4 degrees of freedom the probability of such a χ_ν is 5.5%, while the dashed line is an attempted $\frac{1}{r^2}$ χ-square fit which although it converged it has an unacceptable χ-square per degree of freedom of $\chi_\nu = 22.6$ which has the extremely low probability of 10^{-16}% for a sample with 4 degrees of freedom[51]. As a result the $\frac{1}{r}$ fitting function is a much better approximation to the parent function than the $\frac{1}{r^2}$ function and it verifies the dependence predicted by Eq. 3.6.

During the scanning it was observed that when the electron beam was close to the EO crystal so that the beam was partially impinging on the crystal, a distinctive positive signal with a long decay time of ∼100ns superimposed on the negative EO signal. To examine this further, the electron beam was steered to impinge on the EO crystal and traverse the optical beam path completely as the schematic drawing of Fig. 17 shows. As the electron beam approached the optical path traversing the EO crystal, the strength of the positive signal increased and when the beam passed the optical path, then the superimposed signal became negative. Their traces are plotted in Fig. 19 along with a trace recorded when the electron beam passed clearly unobstructed by the crystal for comparison.

It is conceivable that when the electron beam hits the $LiNbO_3$ crystal it ionizes it to the point that it creates electron-hole pairs. Since the mobility of ions is small compared to the electrons, a transient ion field remains which produces an electro-optical signal opposite to that due to the electron beam field. In that case its decay time will be dictated by the electron-hole recombination time which is characteristic of the material[52]. Because of the electro-optic nature of this slow signal its polarity changes when the electron beam is steered from bellow (-0.17mm) to above (0.33mm)

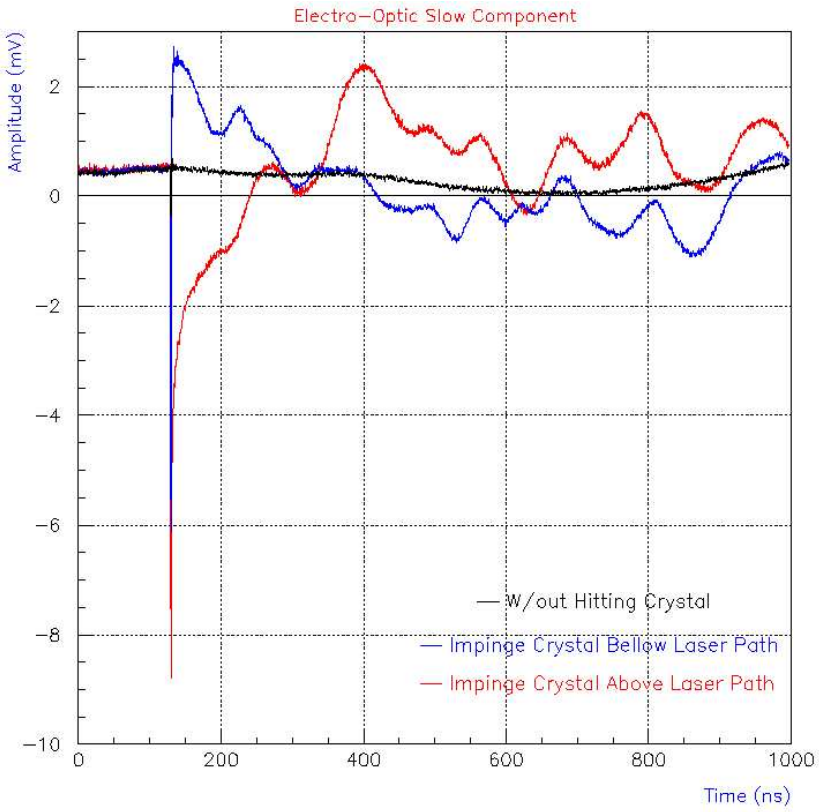

Figure 19: Blue signal: electron beam was hitting the crystal bellow the laser path, Red signal: electron beam was hitting the crystal above the laser path, Black signal: electron beam path was away from the EO crystal.

the laser path. This characteristic provides a unique method to locate the exact electron beam position with respect the laser beam path. This signal is ideal for calibration of the sensor since its timing is the same as the EO signal and the signal to noise ratio is much bigger. However, this ion field disappears and the electron beam field prevails when the electron beam clears the path of the EO crystal.

Now that the electro-optic nature of our signal is established, the focus is turned to the measurement of the temporal profile of the electron beam which is the goal of the experiment. Since the optical modulation is of EO origin which has a inherent

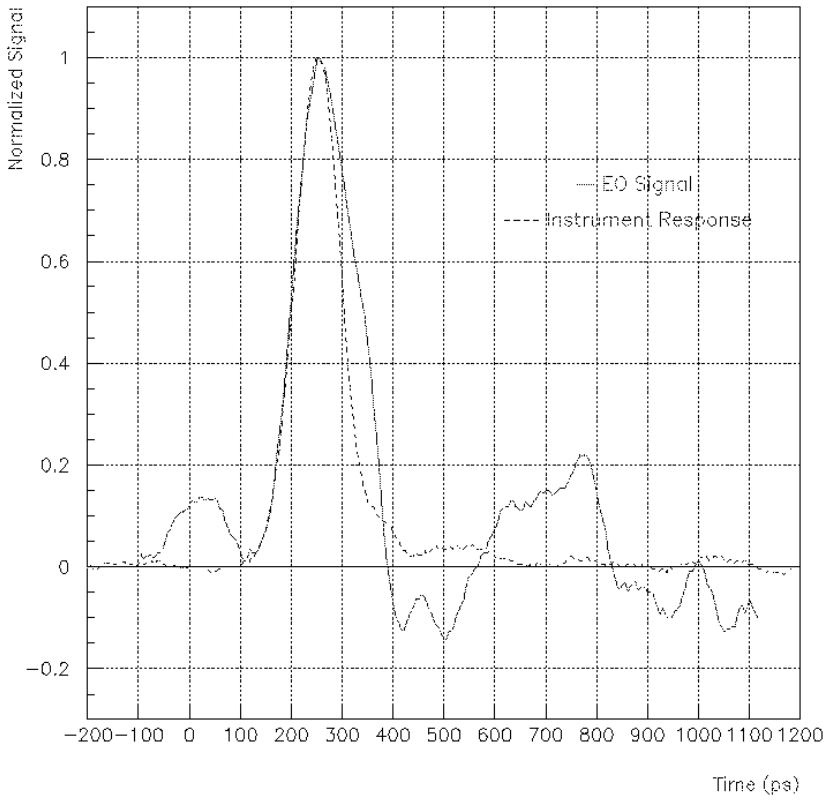

Figure 20: Solid line: electro-optic trace recorded by a 12GHz photoreceiver and a 7GHz digital oscilloscope. Dashed line: instrument response of the detecting system to a ∼15ps IR laser pulse.

response much faster than the ATF electron pulse duration, the measured temporal duration is then limited mostly by the bandwidth of the measurement system and the modal dispersion of the 35m long outgoing graded-index multimode fiber (see **Appendix D** for more details). Lab measurements showed that the modal dispersion of the fibers used, have negligible temporal broadening on the time scale of interest in this experiment. To test the limitations of our detecting system an ∼15ps mode-locked IR laser pulse was used on the same 12GHz optical receiver and 7GHz oscilloscope that were used in the experiment and the recorded pulse rise time was ∼70ps as you

can see in Fig. 20. The rise time of the EO signal is comparable to the one recorded in the lab which proves that the ∼70ps rise time reported is limited by the electronics used for the detection of the pulse.

During the ATF experiment the DC level of the light entering the photodiode was monitored as one can see in Fig. 21. The presence of the DC drift phenomenon is

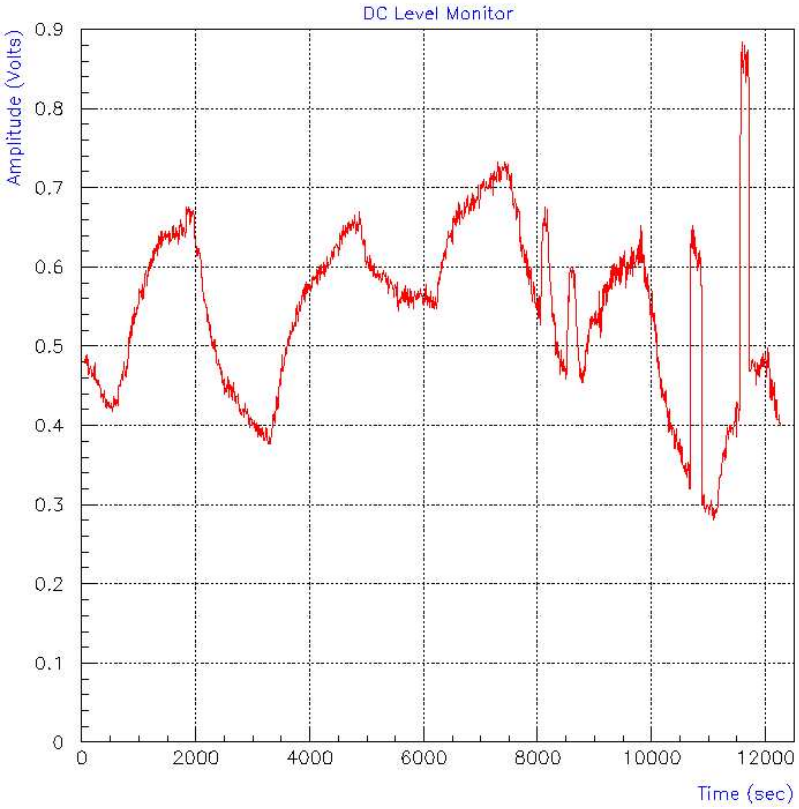

Figure 21: DC level of light arriving at the photodiode as monitored during ATF experiments. The sudden peaks after the 8000 seconds are when the electron beam hits the $LiNbO_3$ crystal. As you can see the crystal returns to its previous state at the moment the electron beam is moved millimeters away from the crystal.

confirmed with a 50 minute period. This drift is caused by a change of the "effective" electric field inside the crystal due to the generation and motion of charge carriers which are mainly electrons [53]. But in $LiNbO_3$ crystals, trap levels are offered by

defects associated with non-stoichiometric composition, oxygen vacancies and metal impurities. Therefore, part of the drifting carriers are trapped in various levels in the forbidden band, and thus built up numerous local fields that cause a refractive index change[54]. In $LiNbO_3$ the light itself is likely to become a generation source of moving carriers and this effect is called photorefractive. The magnitude and time constants of the described behavior depends mainly on the crystal cut and quality.

Although this electro-optic sensor was successfully in the establishment of the EO nature of the detected signal and confirm the predicted dependences, its EO modulation was only 1% of its dc level. The reasons for this relatively small modulation are:

• Bandwidth: The limited bandwidth of the detection system which is limited by the 7GHz oscilloscope. This decreases the modulation of the observed EO signal by a factor of $\sim$10

• Method: The use of the 50% transmittion point technique for conversion of retardation to intensity modulation always gives the highest signal amplitude but the lowest modulation ratio as it was proved in section 2.5.1

• Crystal Orientation: The application of the electron beam induced electric field to the z-axis requires the use of x or y-cut $LiNbO_3$ crystal and in that case the residual birefringence degrades the polarization purity. Remember, in order to maximize the intensity modulation the incoming polarization has to be 45^0 angle with respect the crystal axis (see Eq. 2.16 on page 18). Since the EO signal is a polarization dependent signal, degrading the polarization purity translates to wasting perfectly good photons that simply don't arrive at the crystal with the right polarization, because the analyzer would block them upon exiting the crystal.

Chapter 4

An All Optical Scheme to Detect Charged Particle Beams

4.1 Introduction

In the previous chapter a free-space electro-optical sensor was described and its results were presented along with a discussion of its limitations. Our attention was focused on the disadvantages of the design which can be addressed as follows:

• Bandwidth: For picosecond and sub-picosecond temporal measurements the use of an electronic readout system is not an option. In the literature, the use of advanced optical techniques such as frequency-resolved optical gating (FROG) or spectral phase interferometry are widely used for direct electric field temporal reconstruction. Our choice was the use of a 2ps or/and a 0.5ps resolution Streak Camera (SC) as a detection readout system.

• Method: For dynamic range limited detection systems like the advanced optical techniques described above, the use of near zero optical bias point electro-optic modulation is optimum, since it can deliver the highest modulation ratio possible as we discussed in section 2.5.2 on page 22.

• Crystal Orientation: The choice of near zero optical bias point as an EO modulation method demands that we should have a very good extinction ratio (σ^2) which in turn means that we need high polarization purity. This is because the maximum modulation ratio was found to be inversely proportional to the extinction ratio (see Eq. 2.35 on page 24), so the smaller (better) the σ^2 the bigger the modulation. Therefore, applying the electric field on the x-axis of a z-cut $LiNbO_3$ crystal is the optimum

choice for the setup above, since both the x and y-axis of $LiNbO_3$ have the same index of refraction[29], and no residual birefringence is present to degrade the extinction ratio. Also, the application of the external field along the x-axis causes a rotation by 45^0 of the index ellipsoid about the z-axis (see the derivation of Eq. A.32 on page 132) so the input polarization has to be along x-axis.

4.2 Streak Camera

Although we call it a "camera", a streak camera is quite different from the video and still cameras that we load with film to take pictures. The streak camera is a device to measure ultra-fast light phenomena and delivers intensity vs. time vs. position (or wavelength) information. Its name dates back to the early days of the high speed rotating drum cameras which would "streak" reflected light onto film.

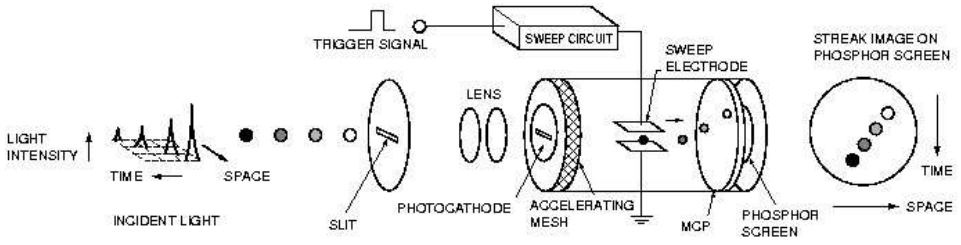

Figure 1: Operating principle of the streak tube.

Fig. 1 shows the operating principle of the streak camera. The light being measured passes through a slit and is formed by the optics into a slit image on the photocathode of the streak tube. The incident light on the photocathode is converted into a number of electrons proportional to the intensity of the light, converting the light image into a electron image. Then high voltage (HV) electrodes accelerate the created electrons toward the deflection field. In the deflection field, a high speed sweep

voltage is applied to a pair of deflection plates at the instant the electron image is passing.

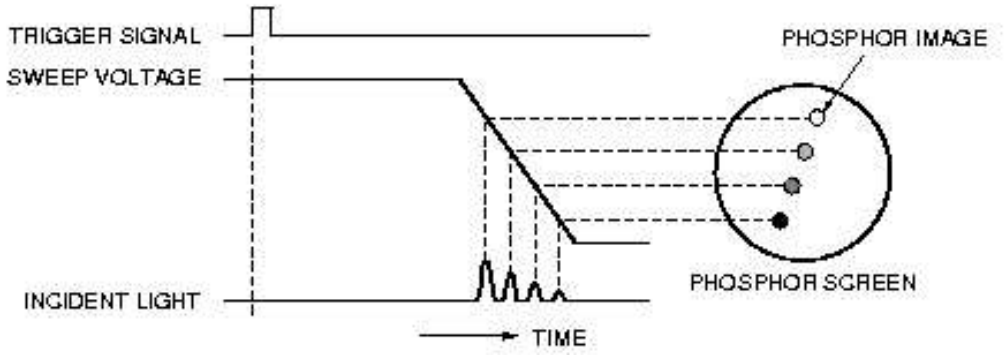

Figure 2: Operation timing during the high speed sweep from the deflection plates.

As you can see with more detail in Fig. 2, during the high speed sweep the electrons which arrive at slightly different times are deflected by slightly different angles in the vertical direction, from top to bottom. It is critical that the high voltage (sweep voltage) applied to the deflection plates is synchronized to the incident light.

The vertical electron image is now directed to the micro-channel plates (MCP) which is an electron multiplier consisting of many thin glass capillaries (channels) with internal diameters ranging from 10 to 20 μm, bundled together to form a disk-shaped plate with a thickness of 0.5 to 1mm (see Fig. 3). The internal walls of each individual channel are coated with a secondary electron emitting material, so that as the electrons come flying through the channels, they bump against the walls, and the repeated impact causes them to multiply in number with a gain of as high as 10^4 for each electron. Therefore, the MCP can perform electron multiplication while retaining the 2-dimensional information. After the MCP the deflected and multiplied electron image impacts against the phosphor screen where they are converted again

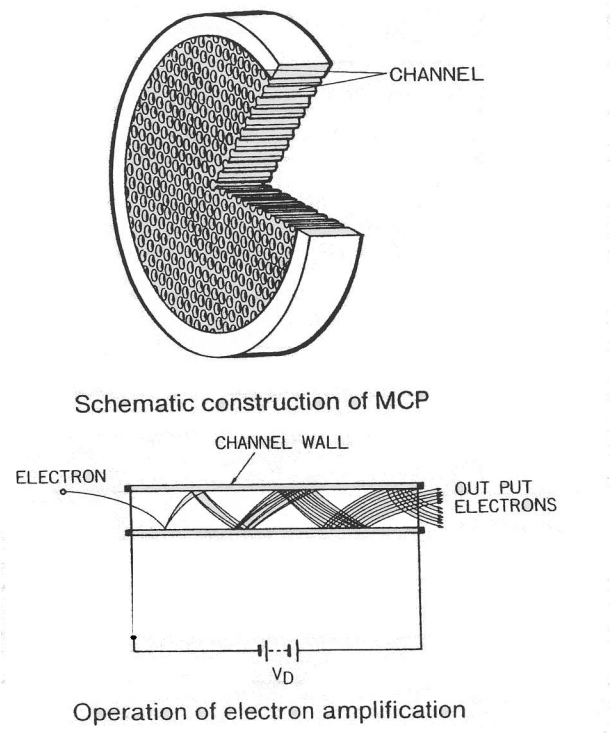

Figure 3: Operation principle of micro-channel plate (MCP).

into light.

On the phosphor screen the vertical axis serves as a time axis since the earliest electrons to arrive are placed in the uppermost position and the horizontal axis of the phosphor screen corresponds to the horizontal location of the incident light. Also the brightness on the phosphor screen is proportional to the intensity of the incident optical pulse.

In order to measure ultra-high speed optical phenomena using a streak camera, a trigger and a readout section are required. The basic configuration needed for the use of a streak camera is shown at Fig. 4. The trigger section controls the crucial timing of the streak sweep. This section has to be adjusted so that the streak sweep

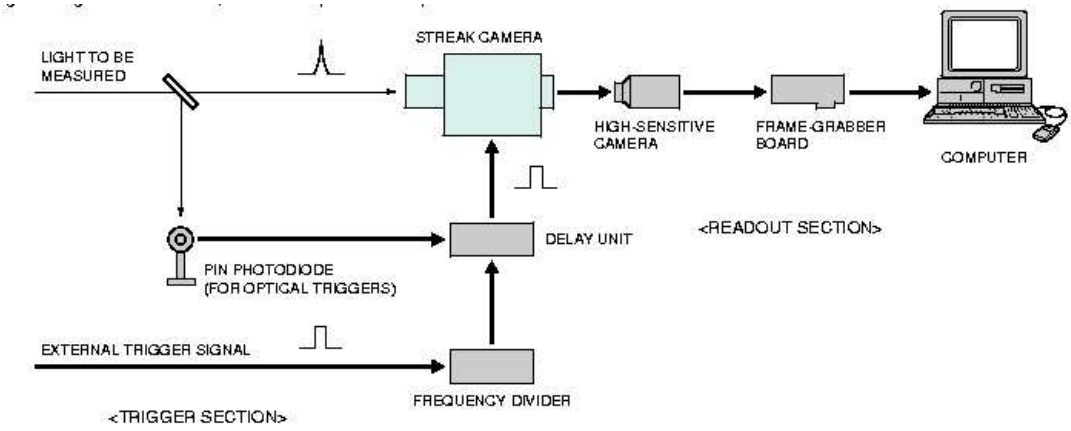

Figure 4: Basic system configuration of streak camera.

is initiated when the light being measured arrives at the streak camera (see Fig. 2). If an external trigger signal is available, then the use of a delay unit is all that is needed. Otherwise, the trigger has to be produced from the light being measured and this is done with the use of a PIN photodiode. The readout section reads and analyzes streak images produced on the phosphor screen, which is on the output side of the streak camera. Because the streak image is faint and disappears in an instant, a high sensitivity camera is used. Analysis of streak images is done by transferring the images through a frame grabber board to a computer.

In our disposal we had a Hamamatsu C1587 streak camera (see Fig. 5) with the following components:

• A N1643 Streak tube with a S20 photocathode which has light response in the range 200-800nm with peak response at 420nm and a maximum quantum efficiency of $\sim$10% and 2-10ps resolution time.

• A M1952 streak unit, which is considered to be a single shot device although it can go up to 1kHz repetition rate. The dynamic range was about 1:100 at the fastest

Figure 5: A Hamamatsu streak camera model C2830 is shown here which is very similar to the C1587 that it was actually used.

sweep range.

A synchroscan FESCA C6860 streak camera from Hamamatsu was also used with a temporal resolution of 500fs (see Fig. 6). This camera, except for the better temporal resolution provided a better dynamic range of 1:1000 and a more sensitive S20 photocathode with the same characteristics as in the C1587 streak camera. Also the synchroscan feature allows a higher signal to noise ratio (S/N).

Synchroscan refers to a high-speed repeated sweep in which a high frequency sine-wave voltage is applied to the deflection plates (see Fig. 7) instead of the ramp voltage applied in the single sweep. By synchronizing the repeated sweep frequencies, streak images can be accumulated (integrated) at a fixed position on the phosphor screen. This allows very faint optical phenomena to be measured with a high S/N.

4.3 Streak Camera Operational Modes and Lab Results

The C1587 Hamamatsu streak camera has 5 different operational modes which are summarized in Table 1. When the SC operates in the focus mode no sweep pulse is

Figure 6: A Hamamatsu streak camera model C6860 with time resolution 500fs.

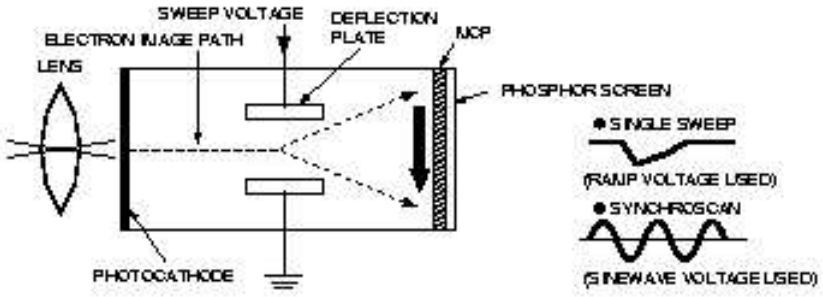

Figure 7: Sweep voltages for single sweep and synchroscan sweep.

applied in the deflection electrodes and that mode can only be used to focus the light at the photocathode and to adjust its brightness. In the normal mode all components of the SC are always on and streak images of light pulses can be viewed. In the Post Blanking or PostBL mode, only the cathode HV electron accelerating mesh is always on while the MCP is gated on for a non adjustable period of time. Gate A is the first operational mode where all components are gated on during the sweep (a pre-trigger of several hundred nanoseconds is required). Gate B has the extra feature of re-sweep

Gating Mode	*Cathode HV*	*Microchannel Plate (MCP)*	*Sweep Pulse*	*Re-Sweep Pulse*
Focus	Always ON	Always ON	No	No
Normal	Always ON	Always ON	Yes	No
Post Blanking	Always ON	Gated ON	Yes	No
Gate A	Gated ON	Gated ON	Yes	No
Gate B	Gated ON	Gated ON	Yes	Yes

Table 1: Summary of SC operational Modes. In the case of Gate B the amount of ON time is adjustable both for the cathode HV and the MCP.

where a long sweep pulse (0.1-10 ms), of opposite direction, is applied after the main sweep pulse for the sole purpose of removing the electrons remained in the SC.

The gating of the components just before the sweep from the deflection plates and the re-sweep are the two main features that enable us to measure light pulses that ride on dc light. The dc light continuously creates electrons at the photocathode and since for the normal and post blanking mode the cathode HV accelerating mesh is always ON, an electronic cloud fills the SC tube which creates internal scattering with the incoming light pulse. This is known as the *space-charge effect* and the result is that light with a dc to signal ratio of 1:1 cannot be measured (see Fig. 8). It takes a mere $\frac{dc}{signal} = \frac{1}{27}$ ratio for the streak image to be visible.

But when the SC operates at Gate A or especially at Gate B mode the electron cloud inside the tube is minimized because the cathode HV and the MCP are operational only just before the pulse arrives. Also in Gate B mode the re-sweep pulse

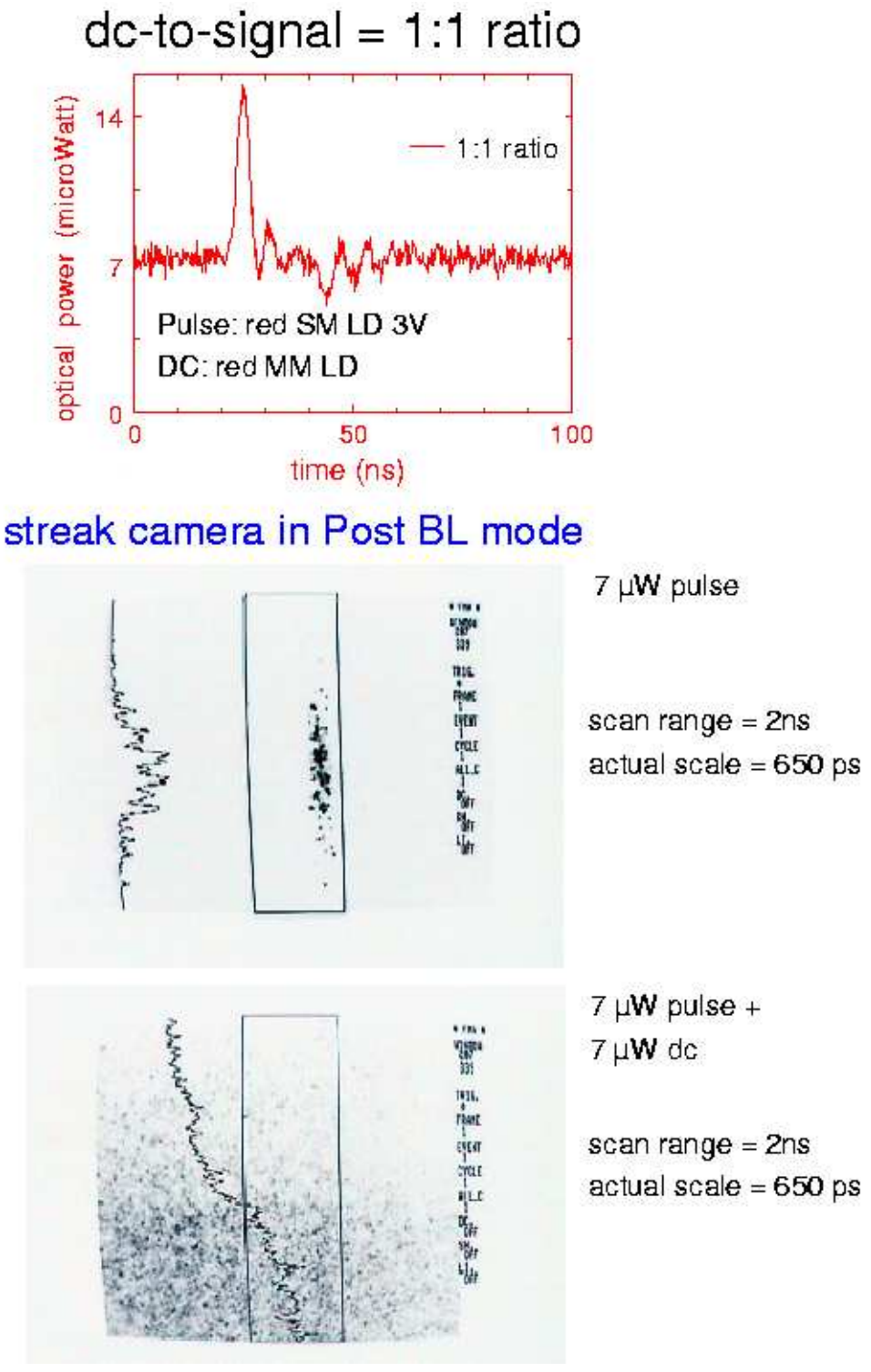

Figure 8: A light pulse of $\sim 8\mu$W is riding on a 7μW dc red light. The streak image of the light pulse alone when the SC operates in Post Blanking mode is clear but when the dc is added along with the pulse a electron cloud is covering the image.

clears the remaining electrons inside the tube and the difference is clear and can be seen at Fig. 9. The results prove that a light signal with a $\frac{dc}{signal} = \frac{4}{1}$ ratio can be viewed in the streak camera.

However, the typical light output when the electric field is applied on the z-axis of an $LiNbO_3$ EO sensor is about 5mW, which is a huge number of photons that will destroy the photocathode of the streak camera tube upon incidence. Even if we choose to ignore that fact, we can afford to have about $\sim 1000\ e^-$ per resolution element of the CCD camera before saturation effects occur[55]. For 514nm light ($E_{514nm} = 4\,10^{-19}\,J/photon$) assuming that

- For a quantum efficiency of 5% for the photocathode we have 6 10^{14} photoelectrons/sec
- For a moderate MCP gain of 100 we have 6 10^{16} photoelectrons/sec
- For a 380ps window we have 24 10^6 photoelectrons
- The CCD camera has a total 5x12 vertical channels

then we have $\sim 400\,10^3$ photoelectrons/channel which is a huge factor above the threshold for saturation effects at the CCD camera. Thus the dc light level has to be as low as possible and the zero bias electro-optical technique is optimal for use with the streak camera.

4.4 Experimental Arrangement

A high vacuum compatible electro-optic sensor was constructed using discrete optical components. All optical elements are located outside the vacuum providing capability for instant adjustments, and light is guided in and out of the vacuum from air using windows. The optical elements are aligned on a aluminum bar which is mounted on a standard $2\frac{3}{4}$ inch vacuum flange, on the side that is outside the vacuum.

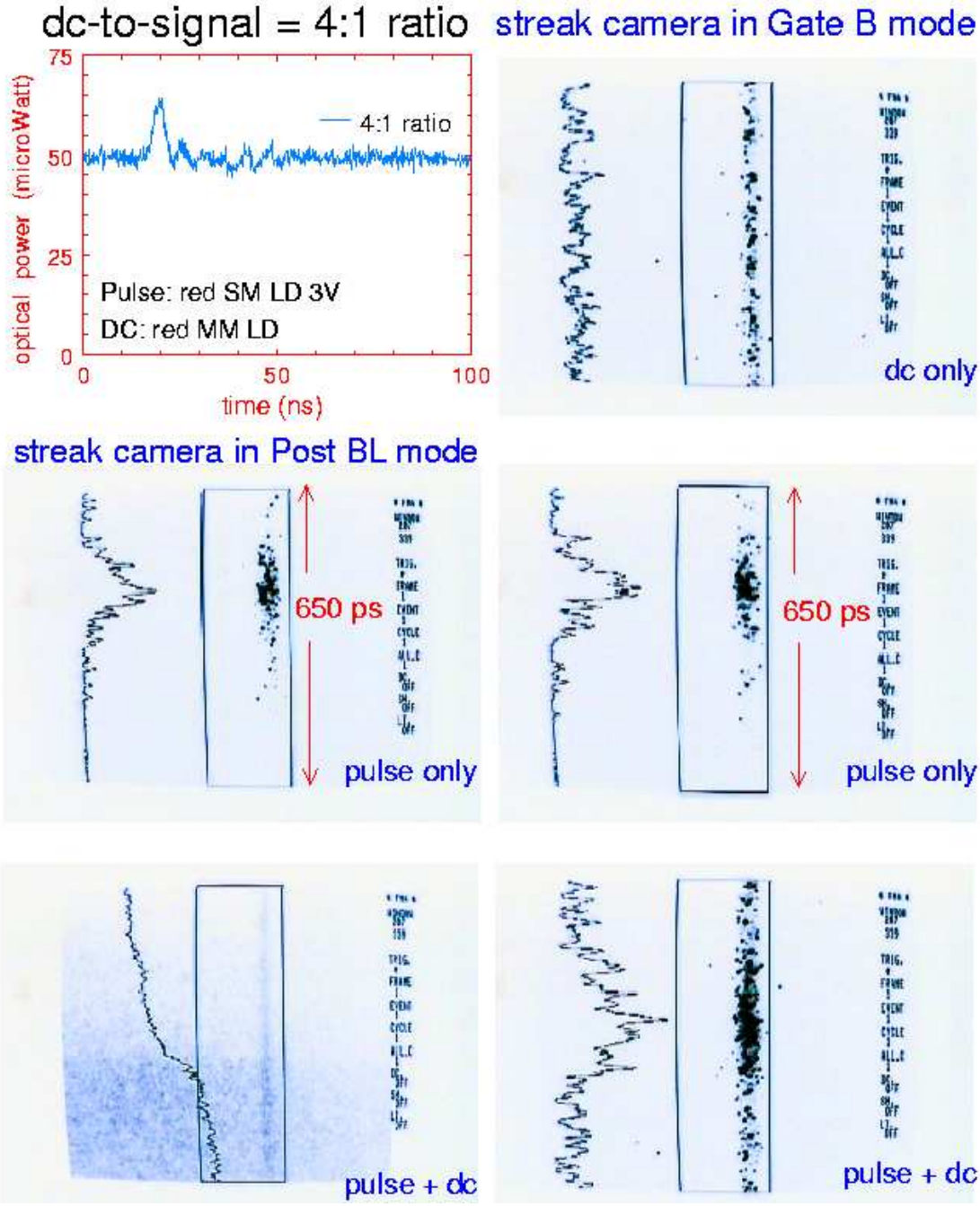

Figure 9: A light pulse of $\sim$ 12μW is riding on a 50μW dc red light a ratio of dc:signal=4:1. In PostBL mode the streak image is clear only when the pulse arrives alone. Otherwise the electronic cloud overwhelms the tube. On the contrary in Gate B mode its presence is clear.

Two custom made circular holes with a glass window on top of them, provided the way for input and output of the light beam. On the vacuum side of the flange, another aluminum bar is mounted which holds the ceramic housing of the EO crystal and an corner-cube that returns the light.

As you can see in more detail in Fig. 10, when the laser light exits the fiber it is collimated by a 20x microscope objective lens which sits on an x-y station for easier adjustment of the collimation. Next comes the polarizer that defines the polarization direction of the light and provides high polarization purity. The light is guided in the vacuum and on the EO crystal using a 90^0 right-angle prism through the first window hole. The $LiNbO_3$ EO crystal is sitting on a ceramic base to avoid inducing wakefields that affect the EO signal. Next a corner-cube was used to guide the light out of the vacuum through the second circular window hole of the flange and onto the 90^0 right-angle prism which is aligned on the same line as the optical elements. The $\lambda/4$ or QWP plate is next along with an analyzer to transform the phase modulation to intensity modulation. And finally a 10x microscope objective lens is used to couple the light into a graded index multimode fiber.

The total light transmission of the setup was 15% of the input power. The transmittance could be improved but in order to keep the dimensions of the EO setup compact the lens telescope technique[56] could not be used. Also there are many surfaces of optical elements at the setup and most of them were uncoated (except window, prisms and microscope objectives) because we were switching the laser light wavelength back and forth, from 1320nm to 514nm, and there is no coating that could accommodate both of them. Most of the light was lost in the polarizer, $LiNbO_3$ crystal and analyzer.

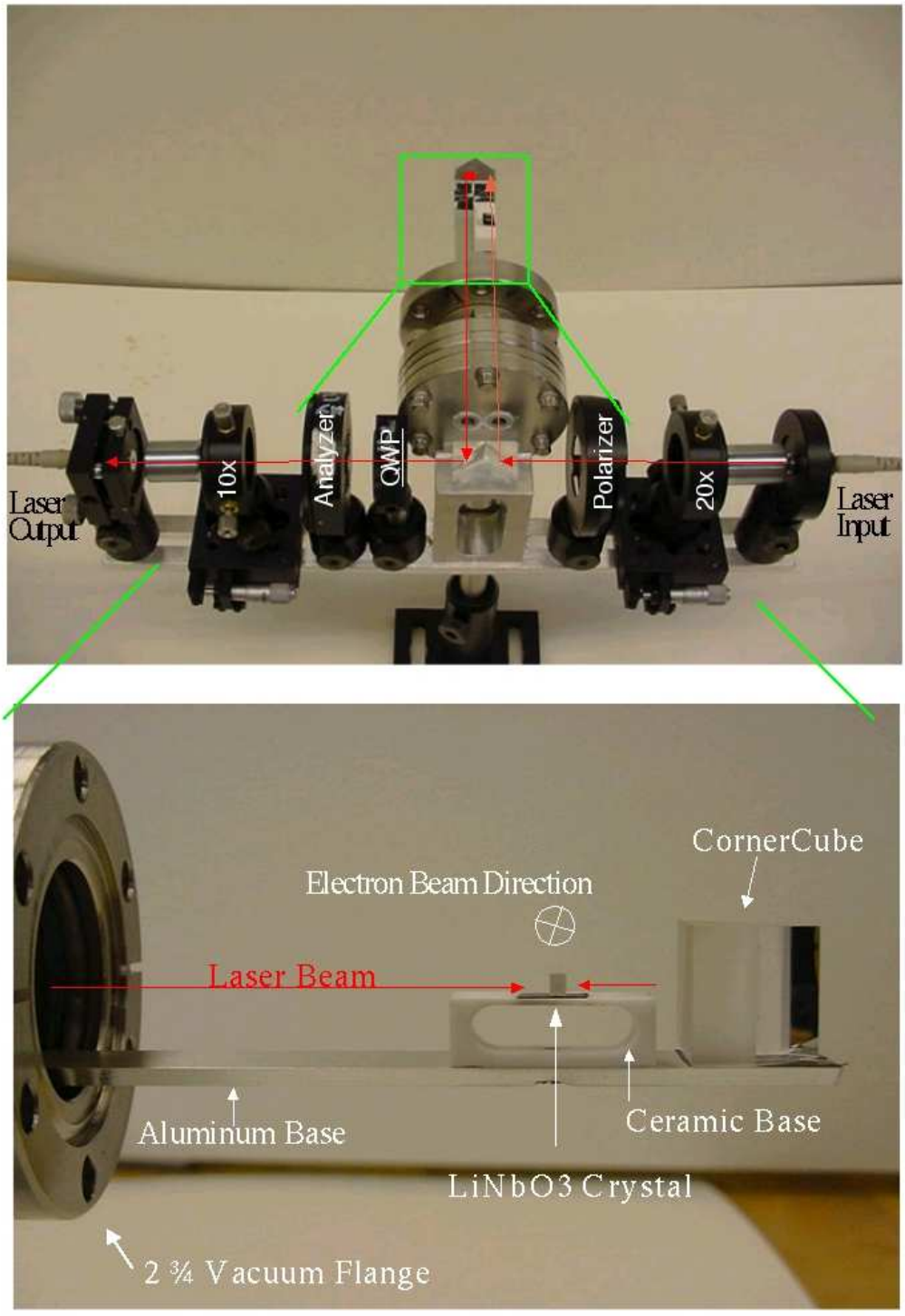

Figure 10: A high vacuum compatible EO sensor designed for high polarization purity. The setup fits in a standard $2\frac{3}{4}$ inch 6-way cross.

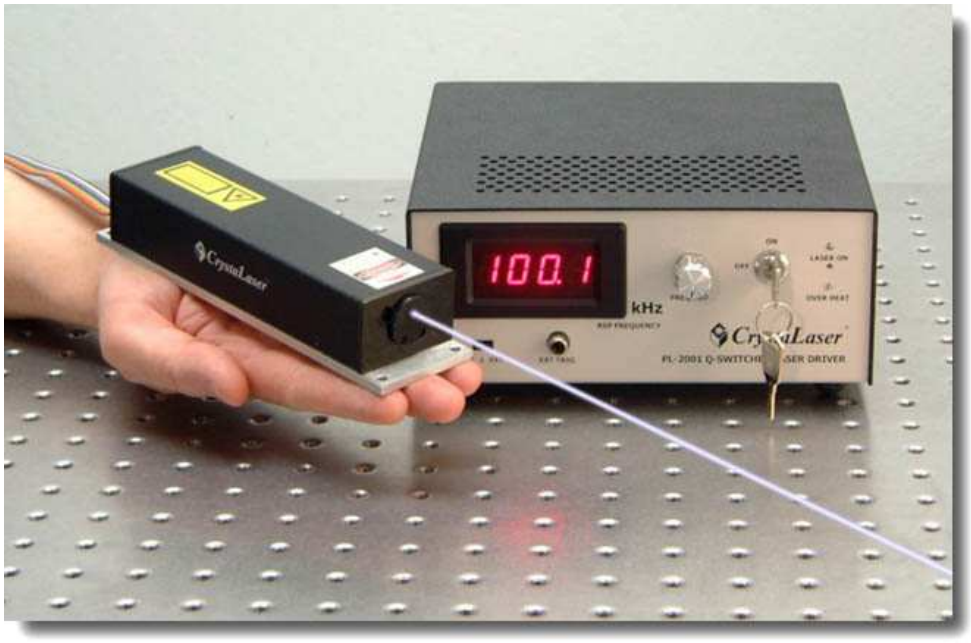

Figure 11: The QG-532-200 is a compact, diode-pumped, solid-state, Q-switched laser from CrystaLaser.

For a light source we used a compact, diode-pumped, solid-state, Q-switched, pulsed laser with fiber coupling output, rented from CrystaLaser (see Fig. 11) . The laser provided a 532nm laser beam with 10μJ of energy per pulse at 1Hz repetition rate capable of maximum 200mW of optical power at 50kHz. There is 100-200ns delay between trigger and the Gaussian profile pulse output with $\sim$20ns jitter. The pulse duration was $\sim$20ns with a faster rise than fall.

The size of the $LiNbO_3$ crystal was 3×3×2 mm (X×Y×Z) with the x-axis aligned azimuthally, the z-axis being the direction of laser beam propagation and y-axis being parallel to the electron beam propagation direction as you can see in Fig. 12. In other words, this EO sensor exploits the transverse EO effect with the electric field applied at the x-axis where the maximum signal modulation is expected (see section 2.5.2).

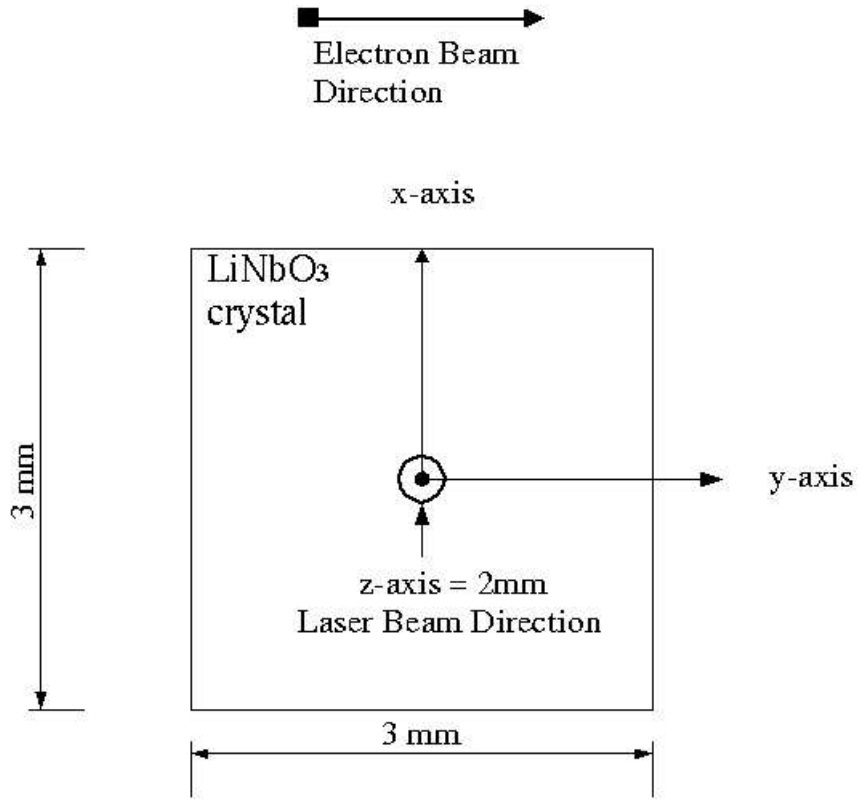

Figure 12: The $LiNbO_3$ crystal orientation for the streak camera experiment. The electric field is applied on the x-axis and the laser beam propagates on the z-axis. This the transverse EO effect.

To maximize the modulation, the analyzer was crossed with the polarizer, and the $\frac{\lambda}{4}$-plate was adjusted to minimize the light transmission after the analyzer. And this is called near zero optical bias EO amplitude modulation.

The polarization purity of the setup was high and the extinction ratio of the setup was $\sigma^2 \leq 5\,10^{-4}$, which didn't change with the addition of the $LiNbO_3$ crystal, because there is no residual birefringence. This enables us to take full advantage of the near zero optical bias amplitude modulation, for which maximum modulation is inversely proportional to the the extinction ratio as you can see in Eq. 2.35 on page

24. So the smaller the extinction ratio, the higher the signal modulation.

The EO setup as described above was tested in the lab using 1GHz photodiode (New Focus 1611) and a 500MHz Oscilloscope (Tektronix) instead of the streak camera. The electric field that was applied along the x-axis was $\frac{430V}{2.5mm} = 172\,\frac{kV}{m}$ with a risetime of 1ns. A small misalignment between polarizer and analyzer was introduced to linearize the EO signal, and that was arranged so it would double the minimum transmission. The EO signal was viewed in both the single shot and the 100 pulse average collection mode as can be seen in Fig. 13, and signals on both sides of the transmission function were recorded which caused an inversion of the EO signal (see Fig. 13(b)).

4.5 Results

The very first thing we did, before we performed measurements with the streak camera, was to observe the signal in the presence of the electron beam, and when the electron was blocked.

As it can be seen in Fig. 14, in the presence of the electron beam a clear signal is observed with 50% modulation in single shot mode (solid red line), whereas when the electron beam is blocked (RF still operating) the signal disappears (dotted blue line). This establishes, beyond any reasonable doubt, that the electron beam induces this signal.

The oscilloscope measurements also showed that the modulation is not exactly constant at 50%. We usually got a modulation in the range of 20-30%, for a 2mm distance of the electron beam from the crystal, but extreme cases of ∼2000% modulation were also observed occasionally as the Fig. 15 shows. The analysis of section

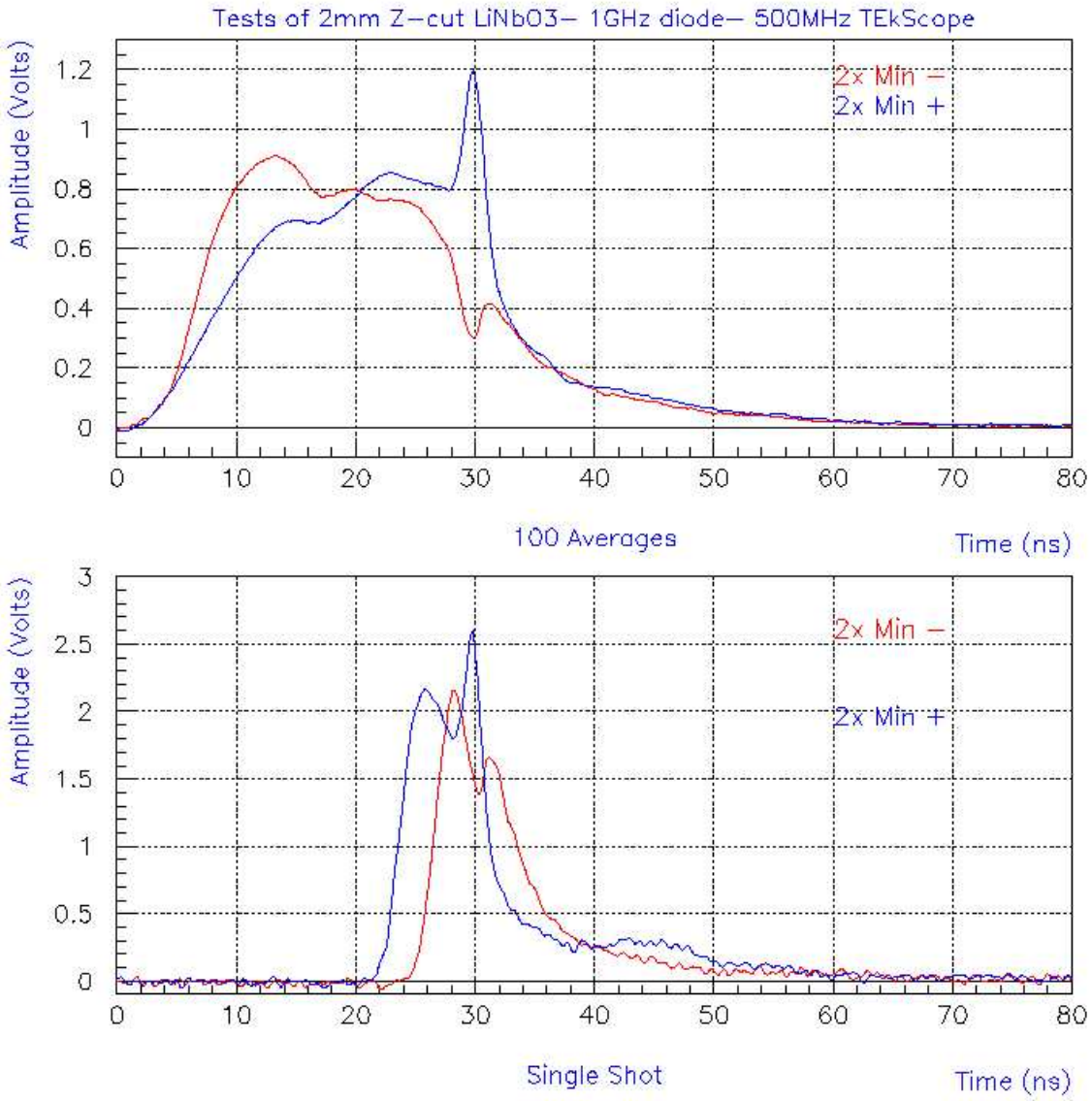

Figure 13: Lab tests on the new EO setup using the pulsed laser. The EO effect was viewed in both single shot and 100 average mode. The electric field used was 172 $\frac{kV}{m}$ and a small misalignment between polarizer and analyzer was introduced (to linearize the EO signal) which doubled the minimum light transmission.

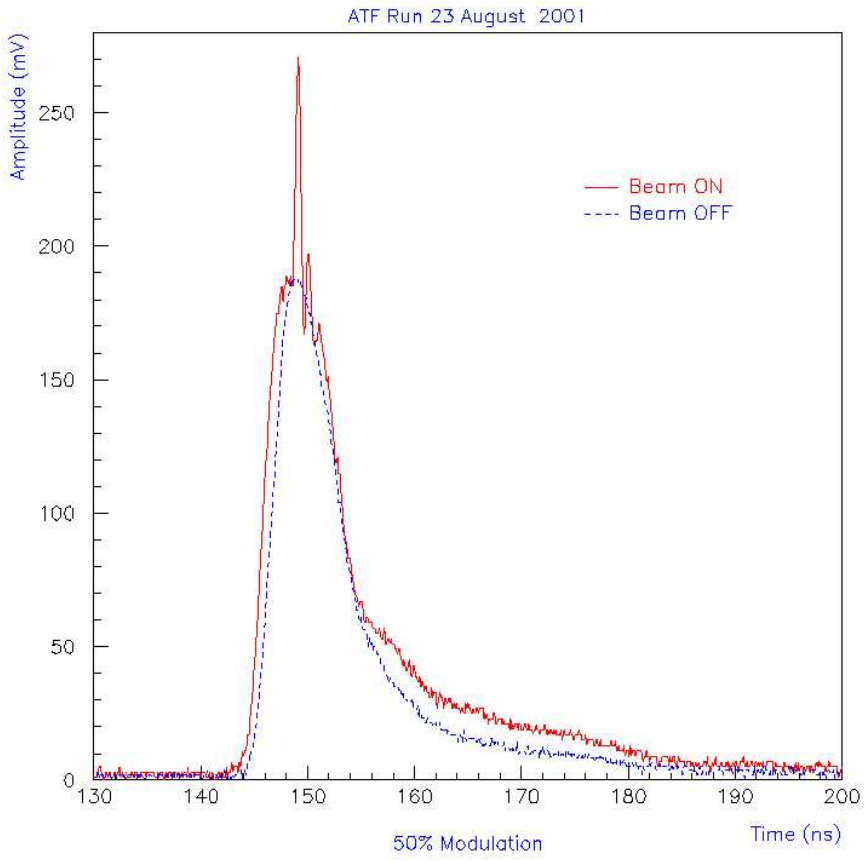

Figure 14: Oscilloscope single shot traces with the electron beam present (solid red line) and without the electron beam (dotted blue line). The intensity modulation was 50%.

2.5.2, which covers the zero bias EO intensity modulation we applied in this experiment cannot explain such a big modulation. What was expected is a modulation of about 10%, for the electron beam 2mm away from the crystal. Such a huge modulation of ∼2000% is an unexpected and unexplained observation as far as the EO effect is concerned.

Next we needed to verify the origin of the signal in the Streak Camera traces. For that purpose we changed the trigger delay of the streak camera using an SRS (Stanford) delay unit. If the signal was induced from the electron beam, then its

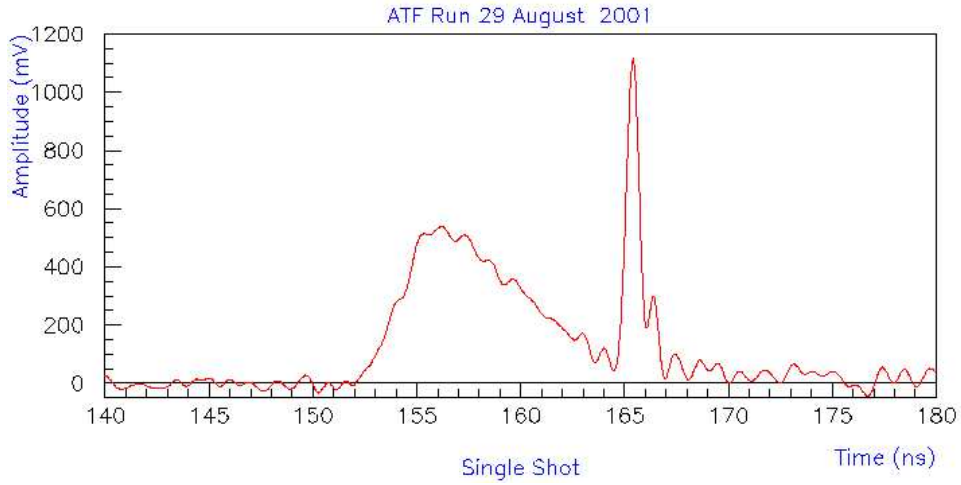

Figure 15: Single shot oscilloscope trace of an extreme case of ∼2000% modulation

arrival time is constant. Changing the SC trigger delay should result in changing the SC time window view. This means that our signal should move in the trace by the same amount, unless it is a noise originating from the camera it self, like the space-charge effect discussed in section 4.3. In that case the signal should follow the camera's view.

Thus, we recorded 100 single shot traces while stepping the trigger delay by 500ps each time. Then the single shot traces were averaged and subtracted from each other. Since the signal is present in both traces, the subtracted trace has two signals: one positive and one negative. The results can be seen in Fig. 16(a) for the case of two signals 1ns apart and in Fig. 16(b) for two signals 500ps apart. The results showed that the signal followed the delay as expected from the assumption that our signal is induced by the electron beam. To further establish our signal we repeated the previous check we did with the oscilloscope where we blocked the electron beam and try to find our signal. In Fig. 17 both traces are the average of 100 single shot, where

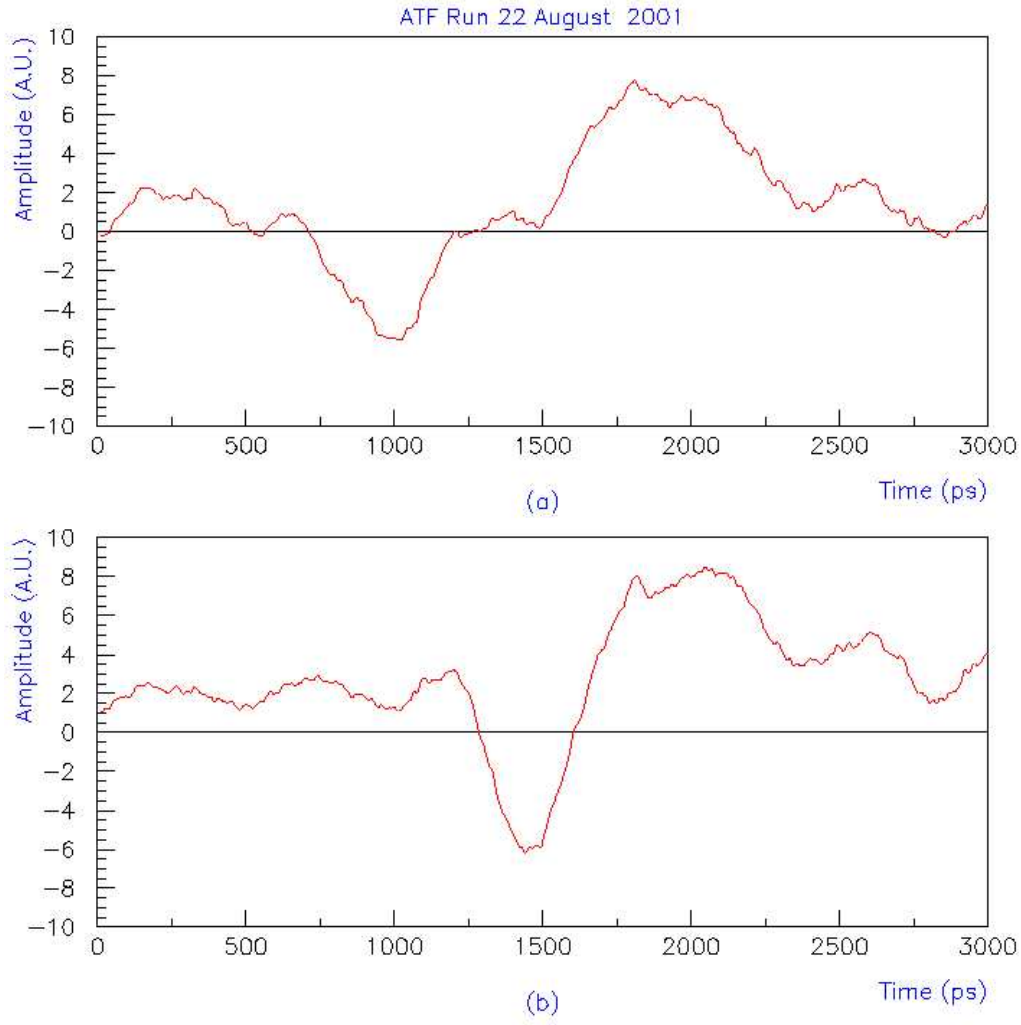

Figure 16: Streak Camera measurements where two signals (average of 100 single shot) with different time triggering delays were subtracted from each other to give a positive and a negative signal. Figure (a) A delay of 1ns was used (b) A 500ps delay was used.

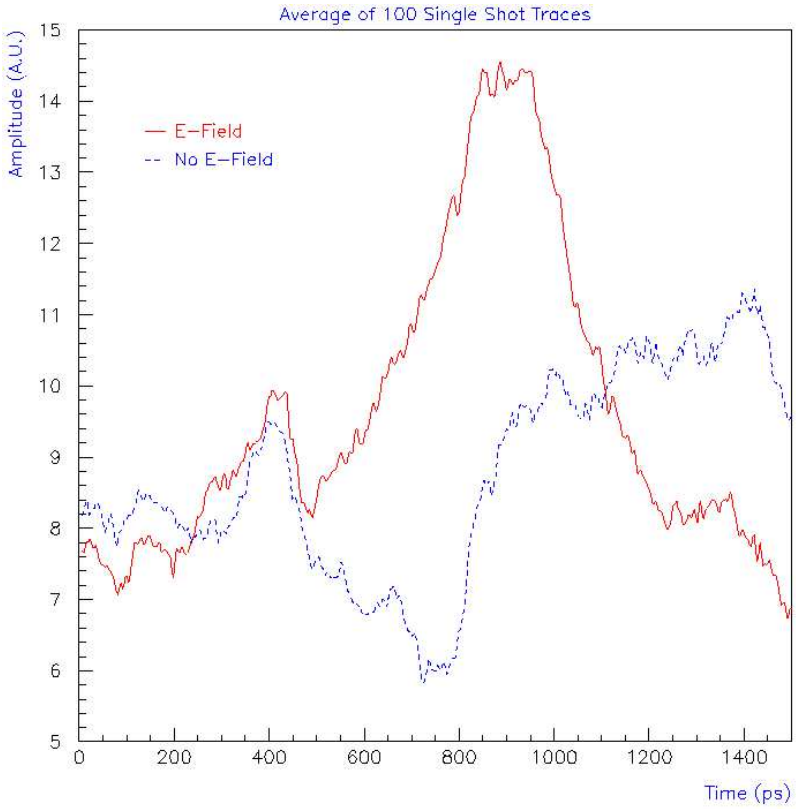

Figure 17: Streak camera average traces (of 100 single shot) in the presence of the electric field from the electron beam (solid red line) and with the electron beam blocked (dotted blue line) while the RF gun was running. The negative deep in the dotted blue trace (electron beam blocked) is due to a spatial inefficiency of the used streak camera's photocathode caused by years of use.

the solid red line is the trace recorded in the presence of the electron beam and the dotted blue line is the trace recorded when the electron beam is blocked while the RF electron gun is operational. This verifies the oscilloscope observations, that the signal is not present when the electron beam is blocked.

The averaged signals shown in Fig. 16 have a duration of 500ps which is much bigger than the 15ps duration of the electron beam. The fact that they are averaged, may have something to do with this since the jitter of a long delay from the delay

box contributes.

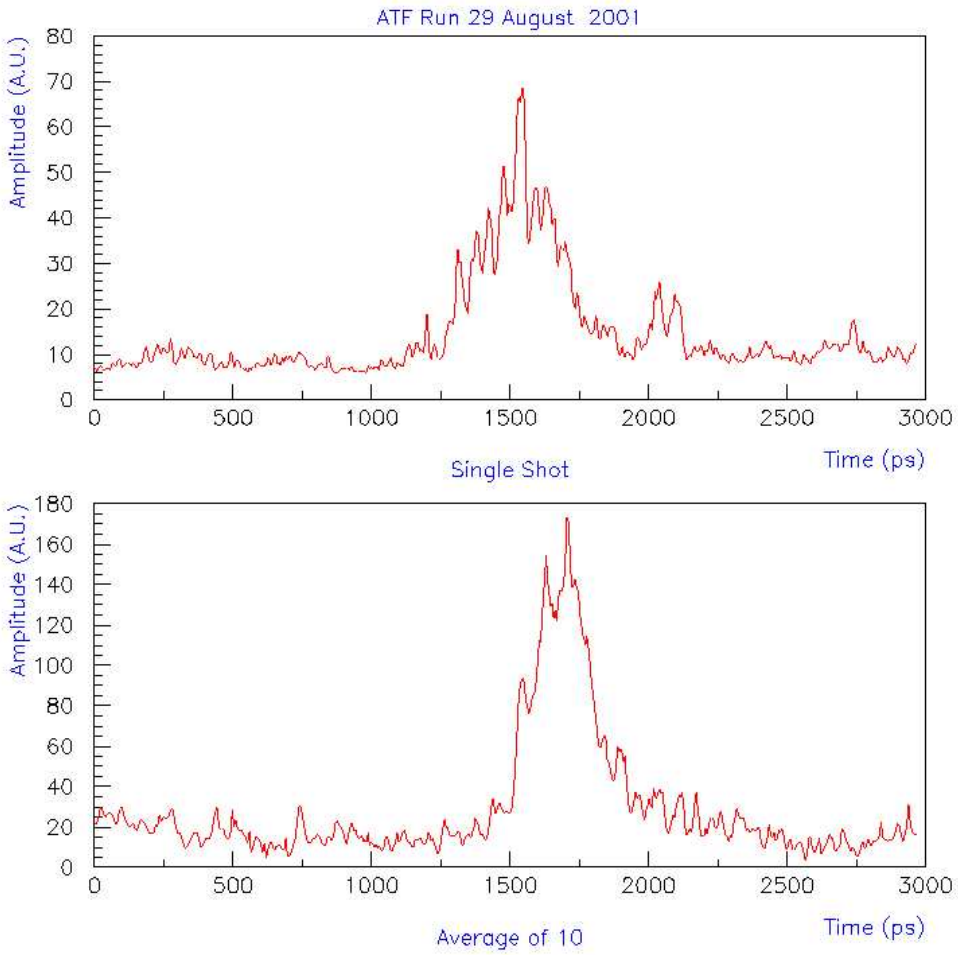

Figure 18: FESCA C6860 femptosecond streak camera single shot signal (Top) and 10 single shot average (Bottom).

Next, single shot traces were recorded using the synchroscan FESCA C6860 streak camera (Fig. 18(top)). A feature of this streak camera is that it can lock the trigger to the RF electron gun frequency. This produces an average collection of traces without any jitter. A average trace of 10 single shots (10 second) is shown in Fig. 18(bottom) and in a 500ps window in Fig. 19.

Single shot traces were also recorded using the picosecond C2830 streak camera.

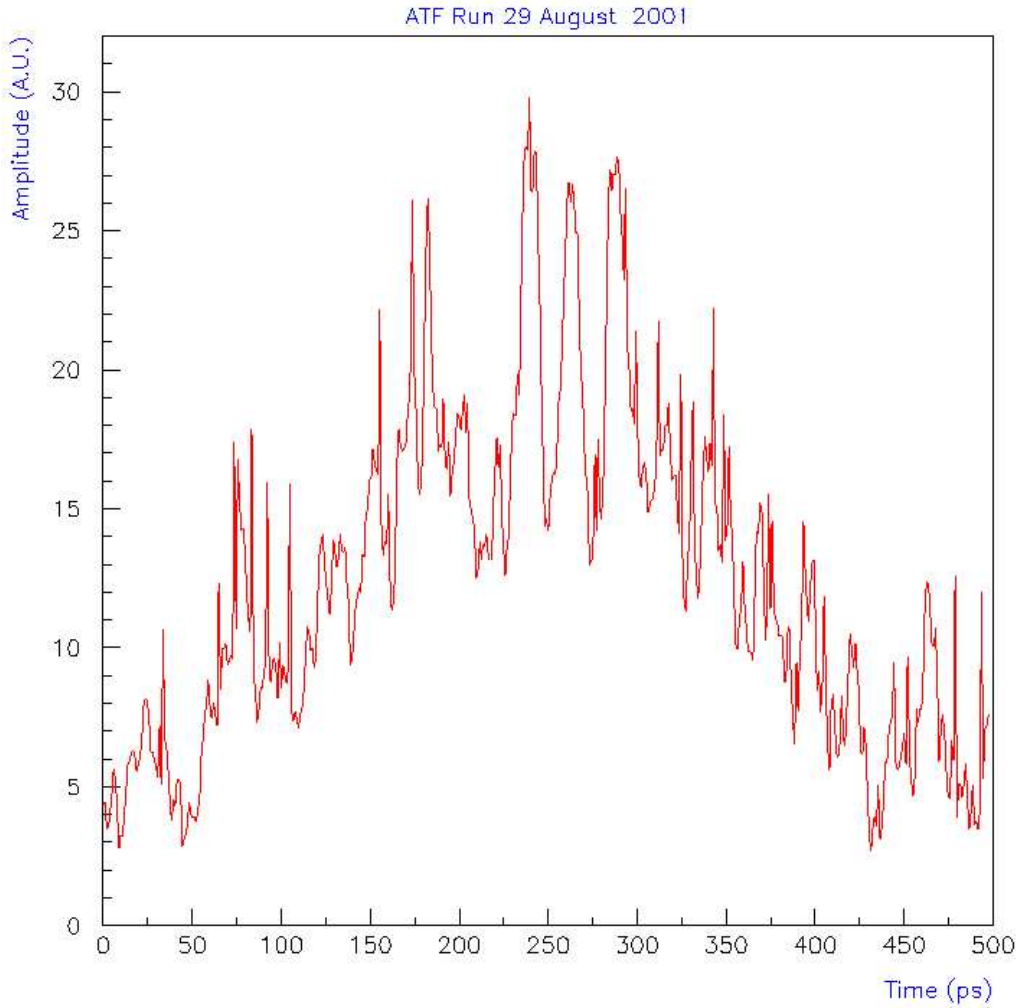

Figure 19: A streak camera trace (FESCA C6860) of 10 single shot average in a 500ps window

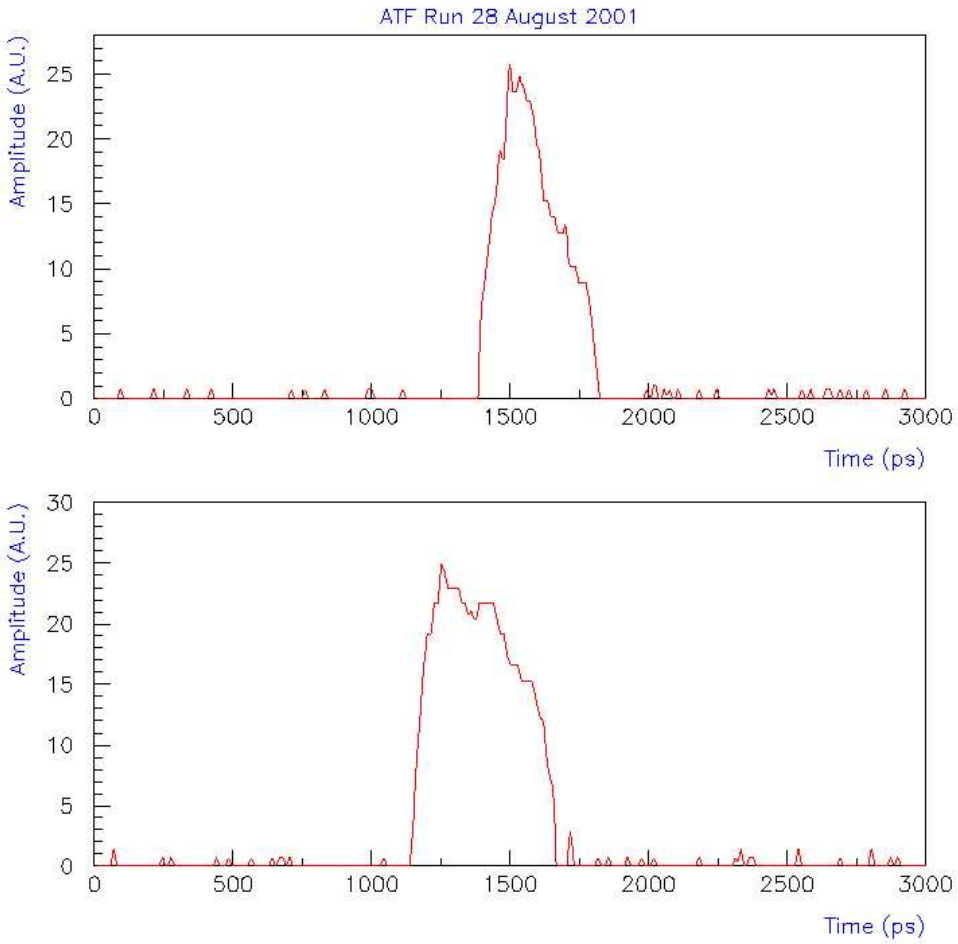

Figure 20: Two single shot streak camera traces (picosecond C2830) in a 3ns window. The presence of jitter is obvious and causes the shift of the traces.

The were recorded in a 3ns time window as shown in Fig. **??** or in a 612ps window shown in Fig. 21.

The duration of all the single shot streak camera traces is also about 500ps, just as in the average traces, which raises the question: Is our signal EO in nature?

To answer that question, a test was performed which aimed to check the linearity of the signal. The analyzer was misaligned by $+5^0$ to -5^0 with respect to the minimum extinction angle of 90^0. As the results show (Fig. 22) both the 85^0 signal (solid red

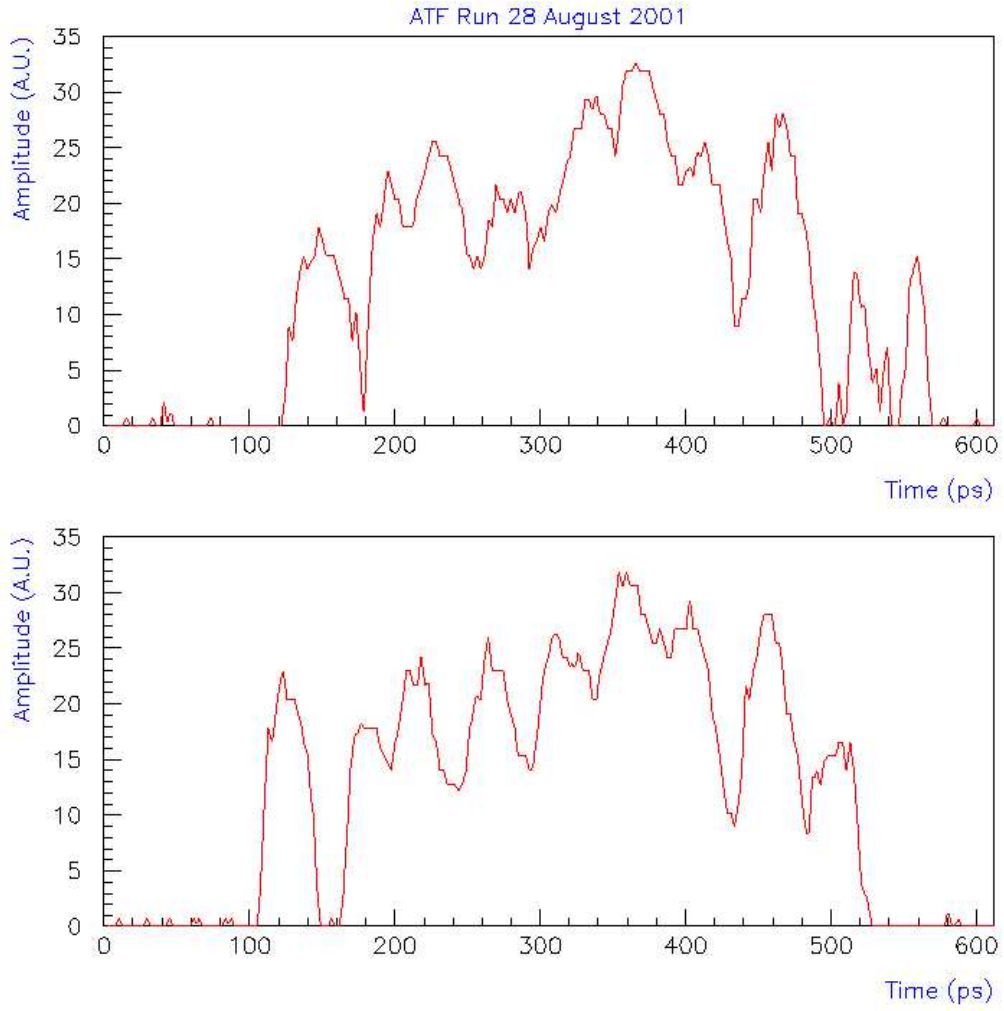

Figure 21: Two single shot streak camera traces (picosecond C2830) in a 612ps window.

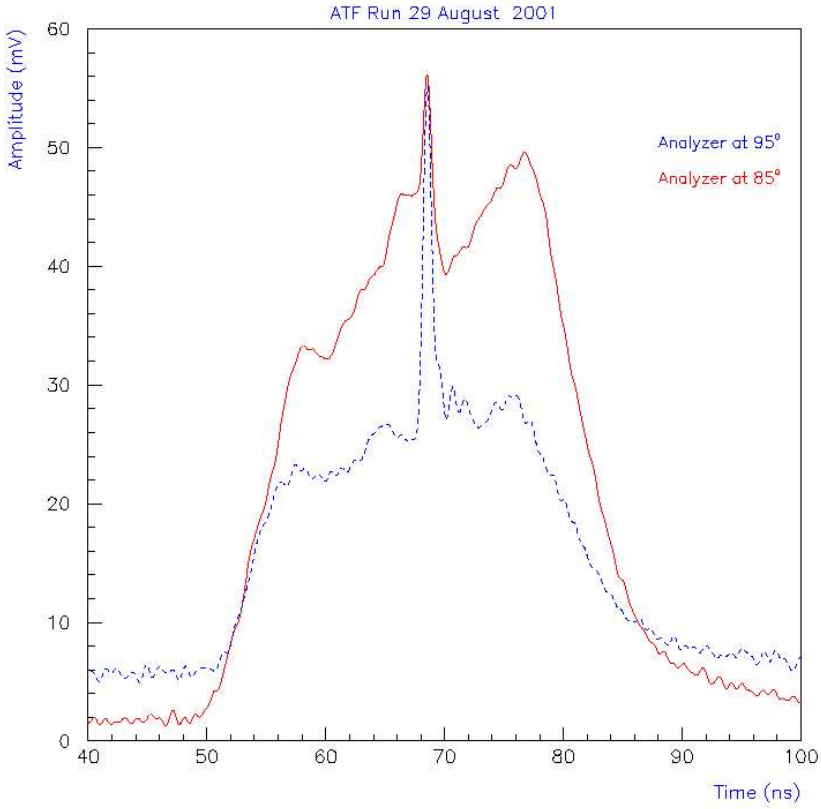

Figure 22: To test the linearity of the signal, the analyzer was set first at 95^0 (dotted blue curve) and then at 85^0 (solid red curve). The trace is an average of 50 single shot.

curve) and the 95^0 signal (dotted blue curve) are positive, not what one would expect from the linear EO effect as demonstrated with the previous EO setup, and from the theory described in Fig. 14(b). Since the signal has a quadratic dependence on the electric field, the linear electro-optic effect is ruled out, as is the quadratic electro-optic effect since it can not induce such a big modulation like the one we observe. Higher order, even dependences, are ruled out for the same reason.

Therefore, the model which involves a electric field with oscillating frequencies, inside a Gaussian envelope, that can reproduce an EO signal with shapes like the one

in Fig. 21 is improbable, since it cannot explain:

• the quadratic electric field dependence or the absence of electric field dependence,

• the 2000% modulation,

• previous experiments with similar optical setup which in the same electron beam conditions did not observe these frequencies.

Another model is that the observed electric fields are "wakefields", that is, fields that are created on the vacuum aluminum pipes or in the surface of the crystal because of the sudden change in the boundary conditions of the charged particle electric field. This model is also improbable, since it cannot explain:

• the absence of an EO signal from the passage of the electron beam,

• the intensity of high frequencies (look at 21.3GHz peak in Fig. 23) which due to dampening should have been low but instead appear the highest of all frequencies

• the 2000% modulation,

• previous experiments with similar optical setup which in the same electron beam conditions did not observe these frequencies.

We realize now, that the signal is not of EO nature but the fact that it disappears when there is no electric-field, means that some other polarization effect must be present to produce the intensity modulation. This effect will have to be much bigger than the existing EO effect in order to be dominant over it. The existence of the EO effect is verified both from the lab tests shown in Fig. 13 and the well known EO theory described analytically in section A.3.

Earlier, in section 2.8, we realized that in optical media which are piezoelectric when an electric field is applied, sound waves can be piezoelectrically generated on

the surface and inside the medium. This can modulate the index of refraction, creating a diffraction grating (see Fig. 11). Then Bragg diffraction occurs, which results (under conditions which are described in section 2.12) in a diffracted light beam with polarization orthogonal to the undiffracted (original) light beam. In the presence of a QWP plate, aligned with the undiffracted light beam, intensity modulation occurs which profiles the sound field.

Looking closely at our experiment, we realize that $LiNbO_3$ is piezoelectric and numerous experiments have reported measurement of sound waves up to 10GHz in $LiNbO_3$[40, 43]. In our experiment, the electron-beam-induced electric field is applied to X-axis of the crystal, and as one can see in Fig. 13 3 acoustic waves are generated and propagate in the X direction. However, only the shear waves induce a change in the index of refraction (look at $\phi = 0^0$), specifically the S_1 and S_2 shear waves. Therefore, we do have a diffraction grating along X-axis which satisfies the Bragg polarization effect conditions (described in section 2.12) applied to the case of a shear wave propagating in z-cut $LiNbO_3$ crystal. The intensity modulation induced from this method is

$$I = \frac{\pi\, n_0^2\, (p_{11} - p_{12})\, e\, C}{h\, c} \int S(\mathbf{r})\, I_0(\mathbf{r})\, \mathrm{d}\tau_{\mathbf{r}} \tag{4.1}$$

where C is a constant which depends on the quantum efficiency of the photocathode and the electron amplification of the MCP. Thus, the signal is just an image of the sound wave in the illuminated region of the crystal, where the light beam is incident and doesn't depend on the electric field that generated the sound wave, whatsoever. That explains a number of properties of our signal:

• The behavior of the signal to the change of the electric field polarity as shown in Fig. 22. According to Eq. (4.1) the light exiting the analyzer doesn't depend directly

on the applied electric field, and its polarity shouldn't change when you rotate the analyzer $\pm 5^0$ about the minimum.

• The huge modulation of ∼2000% we observe. In the presence of the strain-optic effect, the electro-optic effect is just a mere correction. Specifically in $LiNbO_3$[58]:

$$\Delta\left(\frac{1}{n^2}\right)_{PE} = p_{ij}S_j \sim 10^{-2}10^{-5} \sim 10^{-7}$$
$$\Delta\left(\frac{1}{n^2}\right)_{EO} = r_{ij}E_j \sim 10^{-11}10^{2} \sim 10^{-9}$$

which proves that the photoelastic effect is about 100 times stronger than the electro-optic effect. Then the expected 10% EO modulation becomes in the order of 1000% for the case of photoelastic effect, which explains the observed modulation. In section 2.10 you can find an analytic description of the EO effect correction to the strain-optic coefficients.

• It explains the structure of the signal. Looking at the high detail, streak camera, single shot traces shown in Fig. 19 and 21, the presence of a wave is clear. In fact, as Eq. (4.1) shows, the exiting light is just a moving amplitude image of the sound field in the focus region. In other words the signal is just the sound wave image inside the region of the crystal where light propagates.

• It can, in part, explain the ∼450ps duration of the signal. When the shear sound waves S_1 and S_2 are piezoelectrically generated on the surface and inside the $LiNbO_3$ crystal, they propagate its X-axis. Since they induce a change in the index of diffraction in their course (look) a photoelastic signal will be induced at the lighted region of the crystal. The signal will be present as long as the sound waves are present inside the crystal. In other words, the signal duration depends on the attenuation of the sound waves and since the both have different attenuation and speeds S_2 plays an

important role although its index of refraction is smaller than S_1 (look at table 3).

The Fourier transform of the signals seen in Fig. 21 shows (look in Fig. 23) that the highest frequencies of the induced sound waves are 15.2 and 21.3GHz. Following the reasoning of section 2.13, these sound waves will be present in the crystal for

$$21.3GHzX - Fast\ Shear \Rightarrow \sim 216 \pm 10\%\ ps = 194 - 238\, ps$$

$$21.3GHzX - Slow\ Shear \Rightarrow \sim 254 \pm 10\%\ ps = 219 - 279\, ps$$

$$15.2GHzX - Fast\ Shear \Rightarrow \sim 425 \pm 10\%\ ps = 383 - 467\, ps$$

$$15.2GHzX - Slow\ Shear \Rightarrow \sim 498 \pm 10\%\ ps = 448 - 548\, ps$$

Reviewing the signals collected with the streak cameras, shown in Fig. 19 and 21, the sound wave theory can explain the build-up and decay of the signals, and their duration of ∼450ps. That happens if we take into account only the two highest, in intensity, frequencies and ignoring the rest lower in intensity frequencies which are not the same for both signals.

The only way we can be certain that any or combination of the above models fully describe our data we need more funds for more experiments. The only thing we can be certain with the present experiments is the discovery of unexpected crystal response which translate to something new which rarely happens in science these days.

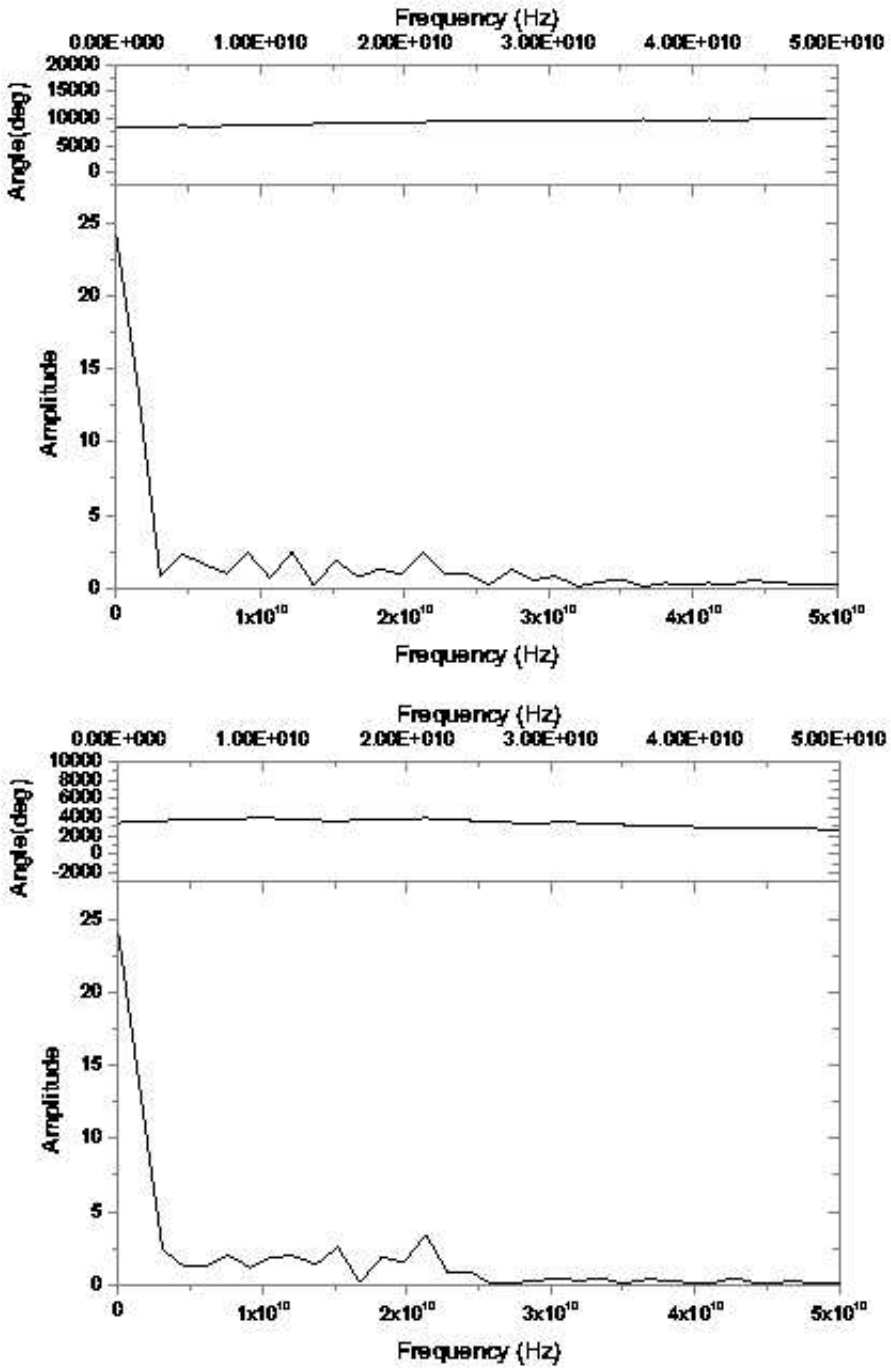

Figure 23: The Fourier transform of the signals viewed in Fig. 21 respectively. It shows that the sound waves frequencies are 15.2GHz and 21.3GHz. The Fourier transform was obtained using the Origin 6.1 commercial program.

Chapter 5

Discussion and Conclusions

5.1 Summary

In May of 1998, we performed the *first* electro-optic detection of a charged particle beam (of ∼15ps duration), at ATF facility of BNL, using a commercially available EO modulator used in telecommunications. The *transverse* EO modulator geometry was used, where the electron beam direction is perpendicular to the crystal and the light propagation direction, as one can see in Fig. 2. The observed signal, shown in Fig. 7, had a risetime of ∼120ps limited not by electronics but from the metallic housing of the modulator which induced strong electric fields at the passage of the electron beam (wakefields). The same observations were repeated at LEAF facility of BNL, but this time the electron beam propagated in air instead of high vacuum.

Since then, a custom-made, free-space, high-vacuum compatible, electro-optic (EO) modulator was constructed using discrete and market available optical components. In its first version, light was guided in and out of the vacuum using polarization maintaining (PM) fibers with collimators on one end. This allowed us to have all optical components in the users room instead of the restricted experimental room. The transverse EO geometry was used where the electric field is applied in the z-axis of a $LiNbO_3$ crystal. The 50% bias amplitude modulation technique was applied, because it is optimum for this arrangement (see section 2.5.1). The residual birefringence present in this arrangement degraded our extinction ratio down to

$\sim 10^{-2}$. By performing a series of tests we were able to verify the EO nature of our signal and its properties, such as:

• The polarity of the signal depends linearly with the sign of the charge or the direction of the applied electric field, as one can see in Fig. 14

• The amplitude of the signal also depends linearly on the electric field amplitude as one can see in Fig. 16

• The $\frac{1}{r}$ dependence of the signal to the distance of the charged particle beam from the $LiNbO_3$ crystal optical path was also verified, as one can see in Fig. 18.

The observed signal had a ∼70ps risetime (look at Fig. 20) which, as the tests showed, was limited by the electronics used for the detection of the optical pulse. The modulation (MD)of our signal, defined as AC amplitude over DC amplitude, was ∼1% for a 0.5nC beam, 2mm away from the crystal. The smallest signal observed was at ∼75pC electron beam charge, which corresponds to $\sim 5\,10^8$ electrons.

In the same series of experiments, an electro-optic slow component was observed when the electron beam impinged on the $LiNbO_3$ crystal with a long decay time of ∼100ns. The signal polarity depends on the position of the charged particle beam relative to the optical path, as one can see in Fig. 19. This signal arrives at the same time the EO effect, as expected, and since it is ∼100 times bigger it can be used for calibration purposes.

In the second version of the free-space, high-vacuum compatible, electro-optic (EO) modulator, the light was guided in and out of the vacuum using optical windows and discrete optical components. The extinction ratio of the setup was very good, $\leq 5\,10^{-4}$, which enabled us to use the zero bias amplitude modulation technique which produces a factor of 10 higher modulation than the 50% bias amplitude modulation

technique used with the first setup (see Section 2.5.2). High modulation was required, because as you can see in Fig. 9, tests showed that the lowest modulation the streak camera can detect is ∼15%, and the zero bias technique can bring us in that range. However, the signal amplitude was much smaller, and we had to use a Q-switched pulsed laser to supply the necessary photons for direct optical observation of the signal to streak camera. Thus we were aiming for the first, all optical, non-destructive, EO detection of charged particle beam.

The optimum geometry for use with zero bias amplitude modulation is to apply the electric field in the X-axis of a z-cut $LiNbO_3$ crystal (see Section 2.5.2) and that is what was used. Although lab tests showed a promising EO signals (see Fig. 13) when the experiment was performed in ATF facility, we saw signals that were not of EO nature. It is conceivable that the slow risetime of the lab applied electric field pulse (∼1ns) did not stimulate the piezoelectric effect in the same way that the fast ATF electron pulse did.

The signal observed had unexpected properties such as:

• The ∼2000% modulation observed, shown in Fig. 15, was ∼100 times more than the one expected from the EO effect,

• The polarity of the signal didn't change when the direction of the electric field changed, as seen in Fig. 22,

• The shape of the signal, seen in Fig. 21,

• The ∼450ps duration of the signal, which is much bigger than the duration of the applied electric field.

These properties can be addressed when we take into account that in a z-cut $LiNbO_3$ crystal, the piezoelectric effect is present. Its direct effect is very weak,

and in the presence of other effects, like the EO effect, is not visible. However, the piezoelectric effect is also the source of generation of sound waves in media as the Eq. 2.61 demonstrates. The sound waves are generated on the surface as well as inside the crystal the moment the electric field is applied. These sound waves change the index of refraction of the medium in which they propagate through the photoelastic effect (see Section 2.9), and as a result a diffraction grating is effectively created (look at Fig. 11). Since the photoelastic effect is typically $\sim$100 times stronger than the EO effect, then no EO signal is expected to be observed.

As studies have shown (see Section 2.11) in a z-cut $LiNbO_3$ with the electric field applied to its X-axis one longitudinal and two shear waves are generated and propagate in the X-axis direction of the crystal. But only the shear waves induce changes in the index of refraction. Therefore, the shear waves are responsible for the Bragg polarization effect as described in Section 2.12. The polarization of the diffracted light beam, which co-propagates with the undiffracted, is rotated 90^0 from the undiffracted thus causing a rotation of the light polarization. Effectively the signal output depends on the sound wave and not directly on the electric field. This effect can explain all the unexpected properties of the observed signals but the only way we can be certain of its presence is to perform more "controlled" experiments with the same setup.

5.2 Conclusions

The results described in this thesis demonstrated beyond any reasonable doubt that the electro-optic effect can be used for non-destructive detection and profile monitor of charged particle beams. Due to the inherent ultra-fast response of the EO effect to the applied electric field, temporal resolutions of a few tenths of femptosecond

can be achieved[6, 7]. This temporal resolution is needed since with the advance of particle accelerators and FEL techniques the bunch duration has dropped to the femptosecond time scale. The EO effect can be used to construct a real-time feedback system for beam bunch adjustments due to its non-destructive property. In sort the EO effect properties are:

- femptosecond time resolution technique,
- linear response to the applied electric field which can be used for profiling a beam bunch,
- it can be used in many beamline positions since it is non-invasive,
- as an optical technique and it has all the advantages of such: low noise, small number of expensive read-out systems, excellent electromagnetic isolation, large frequency response, e.t.c.

On the other hand the Bragg polarization effect doesn't directly depend on the applied electric field and although it is $\sim$100 times bigger than the EO effect it can be used only for detection of a charged particle beam and not for profiling. With careful consideration the generated sound wave can be selected to give very fast signal duration (even in the order of sub-picosecond). That is very promising on the front of single particle detection were as we will see the EO technique can not be used.

5.3 Single Particle Detection

Using an electro-optic sensor to detect single particles is a thesis dissertation by itself. This section is dedicated to a simple theoretical investigation to see if the EO effect can be used for single particle detection.

For a relativistic single electron, 2mm away from a y-cut $LiNbO_3$ crystal (where the Lorentz contracted electron Coulomb field, is applied to z-axis) we expect from

Eq. (3.7) a retardation of $\Gamma \approx 10^{-10} rad$ using the transverse EO effect with the electron 2mm away from the crystal and a 532nm laser. The signal to noise ratio (SNR), in the case of shot noise limited detection, is given by[60]

$$SNR = \Gamma \sqrt{\frac{P\,T\,q_p}{2\,\hbar\,\omega}} \sqrt{\frac{\Gamma_0^2}{\sigma^2 + \Gamma_0^2}} \tag{5.1}$$

where P is the laser power just before the analyzer, T the inverse of the detection system bandwidth (i.e. the time electric field is present), $q_p \approx 0.6$ the quantum efficiency of the photodiode,m $\hbar\omega \approx 0.9eV$ the energy of the laser photon, and Γ_0 the bias we introduce to linearize and amplify the effect. When $\Gamma_0^2 \gg \sigma^2$ the equation reduces to

$$SNR = \Gamma \sqrt{\frac{P\,T\,q_p}{2\,\hbar\,\omega}} \tag{5.2}$$

Now for a SNR=1 and for a $\sim 10\mu$m length of $LiNbO_3$ crystal which will give us $\sim$100fs time resolution, we need P $\approx 0.5\ 10^{15}$ Watt of optical power inside the crystal. This a huge amount of optical power, and even if we could provide it, the $LiNbO_3$ crystal could not sustain. Thus, single particle detection is not possible using the EO effect at the present but using a pulse laser of $\sim 50\mu$J we can see a charged particle beam of $\sim 10^6$ particles.

There is a great interest in research for better EO materials because of their wide use in the field of telecommunications, and already there are on the market polymers like DAST with 10 times better EO properties than $LiNbO_3$. It is expected that this will improve more in the next few years. Nevertheless, to use the EO Effect for single particle detection requires about 6 orders of magnitude improvement, which is unlikely to reached at any time soon. But using this technique as a readout system for gaseous detectors (like Micromegas[57]), which can achieve a single charged particle

amplification factor of $\sim 10^5$, is under investigation.

Appendix A

Electro-optical analysis of $LiNbO_3$ crystal

The index ellipsoid in the presence of an electric field applied on a $LiNbO_3$ crystal changes size and sometimes orientation. All possible cases will be studied in this appendix for $LiNbO_3$, since it is by far the most used EO crystal.

A.1 $LiNbO_3$ Case I : $\vec{E} = (0, 0, E_z)$

Suppose $\vec{E} = (0, 0, E_z)$, meaning that the E-field is applied along the z-axis, then the general equation of its index ellipsoid (2.14) becomes

$$[\frac{1}{n_x^2} + r_{13}\, E_z]x^2 + [\frac{1}{n_y^2} + r_{13}\, E_z]y^2 + [\frac{1}{n_z^2} + r_{33}\, E_z]z^2 = 1 \tag{A.1}$$

Since no mixed terms appear, the principal axes of the new ellipsoid are not rotated. The electric field changed only the length of the axes and their new values are

$$\begin{aligned} n_x = n_0(1 + n_0^2 r_{13}\, E_z)^{-\frac{1}{2}} &\simeq n_0 - \frac{1}{2} n_0^3 r_{13}\, E_z \\ n_y &= n_0 - \frac{1}{2} n_0^3 r_{13}\, E_z \\ n_z &= n_e - \frac{1}{2} n_e^3 r_{33}\, E_z \end{aligned}$$

• In the case of a light beam propagating along the x or y axis (Fig. 1(b)), the induced birefringence seen by it is

$$\Delta n_{induced} = \Delta n_{x,y} - \Delta n_z = \frac{1}{2}(n_e^3 r_{33} - n_0^3 r_{13})\, E_z \tag{A.2}$$

and the retardation induced is

$$\Gamma_{x,y-cut} = \frac{\pi}{\lambda}\, E_z\, l_x\, (n_e^3 r_{33} - n_0^3 r_{13}) \tag{A.3}$$

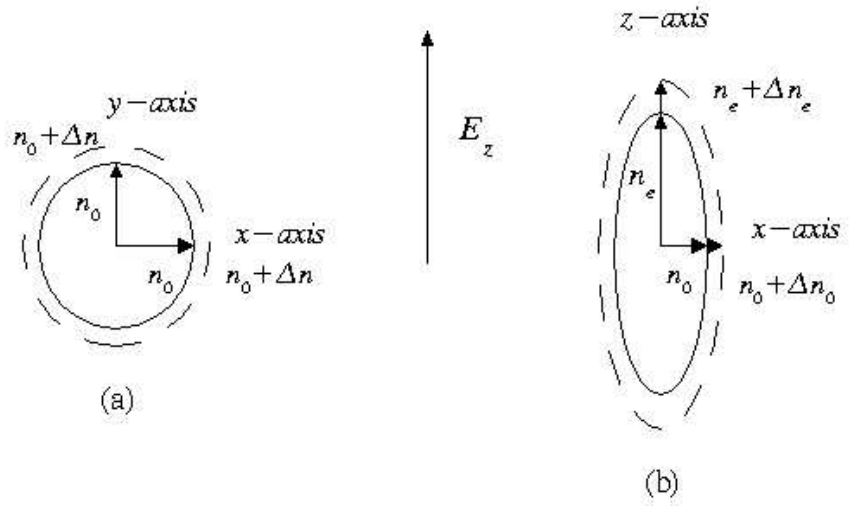

Figure 1: The index ellipsoid change due to an applied electric field in the z-axis.

Testing the above setup in the lab, one applies a voltage at two parallel plates that sandwich the crystal and the electric field is applied normal to the direction of propagation of light. This is called the *transverse electro-optic effect* and is presented graphically in Fig. 2.

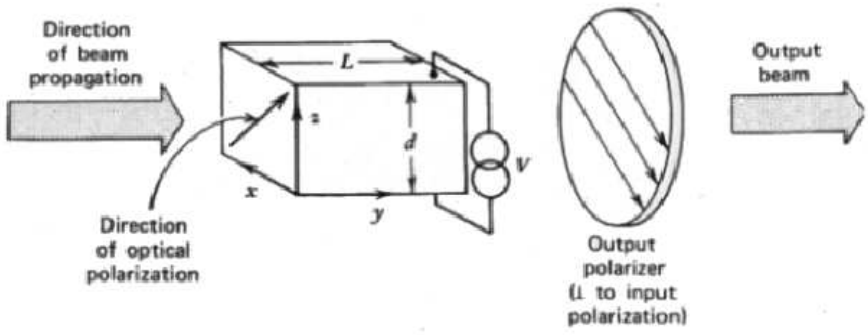

Figure 2: Transverse EO effect; Electric field is applied normal to the direction of optical beam propagation.

In this case, the existence of the dielectric between the two plates doesn't change

the electric field because the power supply of the voltage generator will provide the current (charge) needed to sustain a constant voltage and electric field intensity. With fringing neglected, the electric field is equal to $E_z = E_0 = \frac{V}{d}$ where V is the voltage and d is the spacing of the two plates.

When we use an EO setup to detect the electric field of charged particle beams the charge (current) is fixed instead of the voltage. Subsequently the presence of the dielectric, in this case, will reduce the electric field ($E_z = \frac{E_0}{\varepsilon_r}$) and the retardation by the dielectric constant factor.

• In the case of a light beam propagating along the z axis, then both orthogonal components will experience the same phase change, and no retardation due to the applied electric field will be acquired(see Fig. 1(a)).

Wavelength in nm	Effective Crystal Length in mm	Laboratory Retardation in mrad	Beam Retardation in mrad
at 1320nm	5mm	Γ_{LAB}=133.0	Γ_{BEAM}=4.8
at 1320nm	2mm	Γ_{LAB}=53.2	Γ_{BEAM}=1.9
at 514.5nm	5mm	Γ_{LAB}=392.6	Γ_{BEAM}=14.0
at 514.5nm	2mm	Γ_{LAB}=157.0	Γ_{BEAM}=5.6

Table 1: Retardation Examples for 57.1kV/m applied electric field $\vec{E} = (0, 0, E_z)$ on a x,y-cut $LiNbO_3$ crystal

A.2 $LiNbO_3$ Case II : $\vec{E} = (0, E_y, 0)$

If the electric field $\vec{E} = (0, E_y, 0)$ is along the y-axis, then the equation of the index ellipsoid is:

$$[\frac{1}{n_x^2} - r_{22}\, E_y]x^2 + [\frac{1}{n_y^2} + r_{22}\, E_y]y^2 + [\frac{1}{n_z^2}]z^2 + 2yzr_{51}\, E_y = 1 \tag{A.4}$$

The equation above shows that the presence of an electric field parallel to the y-axis causes length changes in the x,y directions and a rotation of the ellipsoid about x-axis (introduced by the mixed term of Eq. (A.4)). In this case, the crystal becomes biaxial, since all axes have different indices of refraction.

In order to make Eq. (A.4) an ellipse again, we need to introduce a rotation of ϕ around the x-axis using the follow rotation matrices

$$\alpha_{ij}(\phi) = \begin{vmatrix} 1 & 0 & 0 \\ 0 & \cos(\phi) & \sin(\phi) \\ 0 & -\sin(\phi) & \cos(\phi) \end{vmatrix}, \quad \alpha_{ij}^{-1}(\phi) = \begin{vmatrix} 1 & 0 & 0 \\ 0 & \cos(\phi) & -\sin(\phi) \\ 0 & \sin(\phi) & \cos(\phi) \end{vmatrix} \tag{A.5}$$

where the old coordinates $\vec{A}$ become $\vec{A}'$ in the new frame, and they are related with the rotation matrix as follows

$$A_i' = a_{ij}\, A_j, \quad A_i = a_{ij}^{-1} A_j^{-1} \tag{A.6}$$

Thus, the old coordinate system relates with the new one as follows

$$\begin{aligned} x &= x' \\ y &= y' \cos\phi - z' \sin\phi \\ z &= y' \sin\phi + z' \cos\phi \end{aligned} \tag{A.7}$$

and when we substitute Eq. (A.8) to Eq. (A.4) we have

$$[\frac{1}{n_0^2} - r_{22}\, E_y]\, x^2 + [\frac{\cos^2\phi}{n_0^2} + r_{22}\, E_y\, \cos^2\phi + \frac{\sin^2\phi}{n_e^2} + 2\, r_{51}\, E_y\, \cos\phi \cdot \sin\phi]\, y^2$$

$$+[\frac{\sin^2\phi}{n_0^2} + r_{22}\, E_y\, \sin^2\phi + \frac{\cos^2\phi}{n_e^2} - 2\, r_{51}\, E_y\, \cos\phi \cdot \sin\phi]\, z^2 \tag{A.8}$$

$$+[-2\frac{\cos\phi \cdot \sin\phi}{n_0^2} - 2\, \cos\phi \cdot \sin\phi\, r_{22}\, E_y + 2\, r_{51}\, E_y\, (\cos^2\phi - \sin^2\phi)]\, y \cdot z = 1$$

where x, y, z are the new axes.

In order to diagonalize the above matrix and return to elliptic form we need to make the cross term factor $(y \cdot z)$ zero and that means we need a rotation around the x-axis by

$$2\,\cos\phi\cdot\sin\phi\,(\frac{1}{n_e^2}-\frac{1}{n_0^2}-r_{22}\,E_y)+2\,r_{51}\,E_y\,(\cos^2\phi-\sin^2\phi)=0\Rightarrow$$

$$tan2\phi=\frac{2\,r_{51}\,E_y}{\frac{1}{n_0^2}-\frac{1}{n_e^2}+r_{22}\,E_y} \tag{A.9}$$

So when there is electric field applied parallel to the y-axis of $LiNbO_3$ crystal a field dependent rotation of the index ellipsoid around x-axis is created.

The general equation of the new index ellipsoid in the presence of electric field in the y-axis is

$$\begin{aligned}&[\frac{1}{n_0^2}-r_{22}\,E_y]\,x^2+[\frac{\cos^2\phi}{n_0^2}+r_{22}\,E_y\,\cos^2\phi+\frac{\sin^2\phi}{n_e^2}+2\,r_{51}\,E_y\,\cos\phi\cdot\sin\phi]\,y^2\\&+[\frac{\sin^2\phi}{n_0^2}+r_{22}\,E_y\,\sin^2\phi+\frac{\cos^2\phi}{n_e^2}-2\,r_{51}\,E_y\,\cos\phi\cdot\sin\phi]\,z^2=1\end{aligned} \tag{A.10}$$

In the case of y-cut $LiNbO_3$ crystal and an electric field of 57.1 kV/m the rotation of the index ellipsoid around x-axis is

$$tan2\phi=129.2\mu rad\Rightarrow\sin\phi\simeq\phi=3.7\cdot10^{-3}Degrees=64.6\mu rad,\ \cos\phi\simeq1 \tag{A.11}$$

which is very small and all the $\sin^2\phi$ contributions can be ignored. The index of refraction changes when an electric field is applied along the y-axis are

$$\begin{aligned}n_x&=n_0+\frac{1}{2}n_0^3r_{22}\,E_y\\n_y&=n_0-\frac{1}{2}n_0^3(r_{22}\,+2\,r_{51}\,\cdot\sin\phi)\,E_y\\n_z&=n_e+n_e^3r_{51}\,\cdot\sin\phi\,E_y\end{aligned} \tag{A.12}$$

When the electric field is applied along the optical propagation path inside the crystal (Fig. 3), the electro-optic effect is called *longitudinal*.

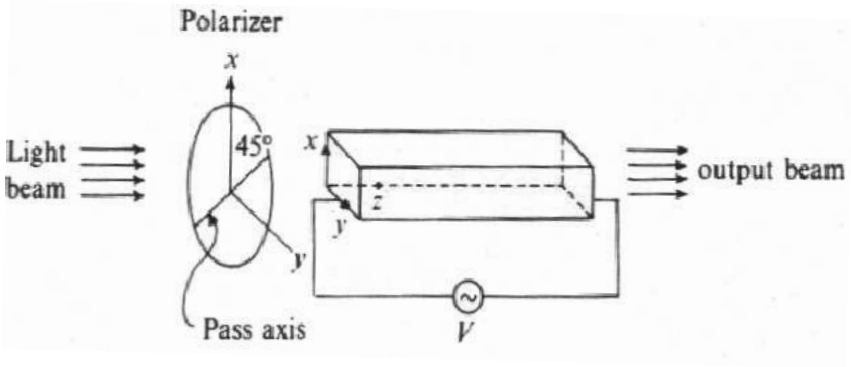

Figure 3: Electric field is applied in the direction of optical beam propagation.

• In the case of a y-cut crystal where the light propagates in the y-axis direction we have

(A.13)

$$\Delta n_{induced} = \Delta n_x - \Delta n_z = \frac{1}{2}(n_0^3 r_{22} - 2\, n_e^3 r_{51} \cdot \sin\phi)\, E_y \simeq \frac{1}{2}(n_0^3 r_{22} - 2\, n_e^3 r_{51} \cdot \phi)\, E_y$$

and the retardation created is

$$\Gamma_{y-cut} = \pi \frac{E_y \ell_y}{\lambda}(n_0^3 r_{22} - 2\, n_e^3 r_{51} \cdot \phi) \tag{A.14}$$

Numerical examples for this EO setup are given in Table 2

• In the case where light propagates along the z-axis (z-cut crystal) and if again we ignore the small $\sin^2\phi$ terms, then we have

$$\Delta n_{induced} = \Delta n_y - \Delta n_x = (n_0^3 r_{22} + n_0^3 r_{51} \cdot \sin\phi)\, E_y \simeq (n_0^3 r_{22} + n_0^3 r_{51} \cdot \phi)\, E_y \tag{A.15}$$

and the retardation created is

$$\Gamma_{z-cut} = 2\pi \frac{E_y \ell_y}{\lambda}(n_0^3 r_{22} + n_0^3 r_{51} \cdot \phi) \tag{A.16}$$

Wavelength in nm	Effective Crystal Length in mm	Laboratory Retardation in mrad	Beam Retardation in μrad
at 1320nm	5mm	Γ_{LAB}=25.1	Γ_{BEAM}=583
at 1320nm	2mm	Γ_{LAB}=10	Γ_{BEAM}=233
at 514.5nm	5mm	Γ_{LAB}=75.6	Γ_{BEAM}=1.8 mrad
at 514.5nm	2mm	Γ_{LAB}=30.2	Γ_{BEAM}=703

Table 2: Retardation Examples for 57.1kV/m applied electric field $\vec{E} = (0, E_y, 0)$ on a y-cut $LiNbO_3$ crystal

Wavelength in nm	Effective Crystal Length in mm	Laboratory Retardation in mrad	Beam Retardation in mrad
at 1320nm	5mm	Γ_{LAB}=53	Γ_{BEAM}=1.2
at 1320nm	2mm	Γ_{LAB}=21.2	Γ_{BEAM}=0.5
at 514.5nm	5mm	Γ_{LAB}=154.5	Γ_{BEAM}=3.6
at 514.5nm	2mm	Γ_{LAB}=62	Γ_{BEAM}=1.4

Table 3: Retardation Examples for 57.1kV/m applied electric field $\vec{E} = (0, E_y, 0)$ on a z-cut $LiNbO_3$ crystal

Numerical examples for this EO setup are given on Table 3

- In the case where light propagates the x-axis (x-cut crystal) and if we ignore again the small $\sin^2\phi$ contribution, then we have

$$\Delta n_{induced} = \Delta n_y - \Delta n_z = -\frac{1}{2}[2(n_e^3 + n_0^3)\, r_{51} \cdot \sin\phi + n_0^3\, r_{22}]\, E_y \tag{A.17}$$

and the induced retardation is

$$\Gamma_{x-cut} = -\pi \frac{E_y \ell_y}{\lambda}[2(n_e^3 + n_0^3)\, r_{51} \cdot \phi + n_0^3\, r_{22}] \tag{A.18}$$

Numerical examples for this EO setup are given on Table 4

Wavelength in nm	Effective Crystal Length in mm	Laboratory Retardation in mrad	Beam Retardation in μrad
at 1320nm	5mm	Γ_{LAB}=26	Γ_{BEAM}=604
at 1320nm	2mm	Γ_{LAB}=10.4	Γ_{BEAM}=242
at 514.5nm	5mm	Γ_{LAB}=75.8	Γ_{BEAM}=1.8mrad
at 514.5nm	2mm	Γ_{LAB}=30.3	Γ_{BEAM}=705

Table 4: Retardation Examples for 57.1kV/m applied electric field $\vec{E} = (0, E_y, 0)$ on a z-cut $LiNbO_3$ crystal

A.3 $LiNbO_3$ Case III: $\vec{E} = (E_x, 0, 0)$

If the electric field is $\vec{E} = (E_x, 0, 0)$ along the X-axis, then the general equation of index ellipsoid 2.14 becomes:

$$[\frac{1}{n_0^2}]x^2 + [\frac{1}{n_0^2}]y^2 + [\frac{1}{n_e^2}]z^2 + 2xz\, r_{51}\, E_x - 2xy\, r_{22}\, E_x = 1 \tag{A.19}$$

The above equation is equivalent with the following matrix:

$$\begin{vmatrix} \frac{1}{n_0^2} & -r_{22}\, E_x & r_{51}\, E_x \\ -r_{22}\, E_x & \frac{1}{n_0^2} & 0 \\ r_{51}\, E_x & 0 & \frac{1}{n_e^2} \end{vmatrix} \tag{A.20}$$

and diagonalizing this matrix is equivalent to rotating the axes of Eq. (A.19).

• In the case, that light propagates the x-axis (x-cut crystal) direction, we need to determine the ellipse formed by the intersection of the plane x=0 (in general the plane that contains the origin and is normal to the direction of propagation) and the ellipsoid. One can easily conclude from (A.19) that there is no induced retardation.

• In the case that light propagates in the y-axis (y-cut crystal) direction then the Eq. (A.19) becomes

$$[\frac{1}{n_0^2}]\, x^2 + [\frac{1}{n_e^2}]\, z^2 + 2\, xz\, r_{51}\, E_x \;=\; 1 \tag{A.21}$$

In order to eliminate the mixed term a rotation about the y-axis has to be introduced and the new axes are related with the old ones as follows

$$\begin{aligned} x &= x' \cos\phi - z' \sin\phi \\ y &= y' \\ z &= x' \sin\phi + z' \cos\phi \end{aligned} \tag{A.22}$$

When we substitute Eq. (A.23) into Eq. (A.21) we have

$$[\frac{\cos^2\phi}{n_0^2} + \frac{\sin^2\phi}{n_e^2} + \sin 2\phi \cdot r_{51}\, E_x]\, x^2 + [\frac{\cos^2\phi}{n_e^2} + \frac{\sin^2\phi}{n_0^2} - \sin 2\phi \cdot r_{51}\, E_x]\, z^2 = 1 \tag{A.23}$$

with the rotation angle being equal to

$$tan2\phi = \frac{2\, r_{51}\, E_x}{\frac{1}{n_0^2} - \frac{1}{n_e^2}} \tag{A.24}$$

So, when the field is applied parallel to x-axis there is a field dependent rotation of the index ellipsoid around the y-axis.

In the case of 57.1 kV/m electric field on x-axis the angle of rotation of the index ellipsoid around the y-axis is:

$$tan2\phi = 129.2\mu rad \Rightarrow \sin\phi \simeq \phi = 3.7 \cdot 10^{-3} Degrees = 64.6\mu rad,\ \cos\phi \simeq 1 \tag{A.25}$$

If we ignore the small $\sin^2\phi$ contribution the induced birefringence is

$$\Delta n_{induced} = \Delta n_x - \Delta n_z = -\frac{1}{2}(n_e^3 + n_0^3)\, r_{51}\, E_x\, \sin 2\phi \tag{A.26}$$

and the induced retardation is

$$\Gamma_{y-cut} = -\pi \frac{E_x \ell_x}{\lambda} [(n_e^3 + n_0^3) \cdot r_{51} \cdot \sin 2\phi] \tag{A.27}$$

Numerical examples for this EO setup are given on Table 5

Wavelength in nm	Effective Crystal Length in mm	Laboratory Retardation in μrad	Beam Retardation in μrad
at 1320nm	5mm	Γ_{LAB}=33.6	Γ_{BEAM}=0.78
at 1320nm	2mm	Γ_{LAB}=13.5	Γ_{BEAM}=0.31
at 514.5nm	5mm	Γ_{LAB}=98.4	Γ_{BEAM}=2.3
at 514.5nm	2mm	Γ_{LAB}=39.4	Γ_{BEAM}=0.92

Table 5: Retardation Examples for 57.1kV/m applied electric field $\vec{E} = (E_x, 0, 0)$ on a y-cut $LiNbO_3$ crystal

- In the case that light propagates in the z-axis (z-cut crystal) direction then Eq. (A.19) becomes

$$[\frac{1}{n_0^2}]\, x^2 + [\frac{1}{n_0^2}]\, y^2 - 2xy\, r_{22}\, E_x = 1 \tag{A.28}$$

Again a rotation about the z-axis has to be introduced in order to eliminate the mixed term. The rotation matrix is

$$\alpha_{ij}^{-1}(\phi) = \begin{vmatrix} \cos(\phi) & -\sin(\phi) & 0 \\ \sin(\phi) & \cos(\phi) & 0 \\ 0 & 0 & 1 \end{vmatrix} \tag{A.29}$$

and the new axis are related with the old ones as follows

$$\begin{aligned} x &= x' \cos\phi - y' \sin\phi \\ y &= x' \sin\phi + y' \cos\phi \\ z &= z' \end{aligned} \tag{A.30}$$

Replacing Eq. (A.31) to Eq. (A.28) gives

$$[\frac{1}{n_0^2} - r_{22}\, E_x \cdot \sin 2\phi]\, x^2 + [\frac{1}{n_0^2} + r_{22}\, E_x \cdot \sin 2\phi]\, y^2 = 1 \tag{A.31}$$

with the rotation angle around z-axis being equal to

$$1 - 2\sin^2\phi = 0 \Rightarrow \sin^2\phi = \frac{1}{2} \Rightarrow \phi = 45^0 \tag{A.32}$$

In this case the rotation of the index ellipsoid 45^0 about the z-axis is independent of the strength of the applied electric field. Thus Eq. (A.31) becomes

$$[\frac{1}{n_0^2} - r_{22}\,E_x]\,x^2 + [\frac{1}{n_0^2} + r_{22}\,E_x]\,y^2 = 1 \tag{A.33}$$

The induced birefringence is

$$\Delta n_{induced} = \Delta n_x - \Delta n_z = n_0^3\,r_{22}\,E_x \tag{A.34}$$

and the induced retardation is

$$\Gamma_{z-cut} = 2\pi\frac{E_x\ell_z}{\lambda}n_0^3 r_{22} \tag{A.35}$$

Numerical examples for this EO setup are given on Table 6

Wavelength in nm	Effective Crystal Length in mm	Laboratory Retardation in mrad	Beam Retardation in mrad
at 1320nm	5mm	Γ_{LAB}=52.0	Γ_{BEAM}=1.2
at 1320nm	2mm	Γ_{LAB}=20.8	Γ_{BEAM}=0.48
at 514.5nm	5mm	Γ_{LAB}=151.3	Γ_{BEAM}=3.5
at 514.5nm	2mm	Γ_{LAB}=60.5	Γ_{BEAM}=1.4

Table 6: Retardation Examples for 57.1kV/m applied electric field $\vec{E} = (E_x, 0, 0)$ on a z-cut $LiNbO_3$ crystal

Appendix B

Jones Matrices

Many sophisticated birefringent optical systems, like an electro-optic modulator, involve the passage of the light through a series of polarizers and retardation plates. Although the calculations for the effect on the light of one optical element is not difficult[58] the same calculation for many of them can be cumbersome. The Jones calculus[59] is a powerful 2x2 matrix method in which the state of polarization of a plane wave is represented by a two-component vector, in terms of its complex amplitudes as a column vector:

$$J = \begin{pmatrix} A_x\, e^{i\delta_x} \\ A_y\, e^{i\delta_y} \end{pmatrix} \tag{B.1}$$

The Jones vector is a complex vector, and it contains complete information about the amplitudes and the phases of the electric field vector component. The electric field is chosen to define the state of polarization because in most optical media, physical interactions with wave involve the electric field. Since we are only interested in the polarization state of the wave, it is convenient to use the normalized Jones vector which satisfies the condition that

$$J^* \cdot J = 1 \tag{B.2}$$

where the asterisk (*) denotes complex conjugation.

Each optical element can be represented by a 2x2 matrix. Therefore, you can obtain the overall matrix for any optical system by multiplying all matrices for the

elements and the polarization state of the transmitted light is computed by multiplying the vector representing the input light beam by the overall matrix. First the mathematical formulation of the Jones matrix method is presented without derivation and then we apply it to our electro-optical system.

B.1 Summary of Jones Matrices

Jones Vectors		
Polarization State	*Complex Vector*	*Normalized Vector*
Linearly polarized wave along $\hat{x}$-axis	$\begin{pmatrix} A_x\, e^{i\delta_x} \\ 0 \end{pmatrix}$	$\begin{pmatrix} 1 \\ 0 \end{pmatrix}$
Linearly polarized wave along $\hat{y}$-axis	$\begin{pmatrix} 0 \\ A_y\, e^{i\delta_y} \end{pmatrix}$	$\begin{pmatrix} 0 \\ 1 \end{pmatrix}$
Lin. pol. wave in an angle θ in respect $\hat{x}$-axis	$\begin{pmatrix} A_x\, e^{i\delta} \\ A_y\, e^{i\delta} \end{pmatrix}$	$\begin{pmatrix} cos\theta \\ sin\theta \end{pmatrix}$
Right-hand circularly polarized wave	$\begin{pmatrix} A_x\, e^{i\delta} \\ A_y\, e^{i\delta+\frac{\pi}{2}} \end{pmatrix}$	$\frac{1}{\sqrt{2}} \begin{pmatrix} 1 \\ -i \end{pmatrix}$
Left-hand circularly polarized wave	$\begin{pmatrix} A_x\, e^{i\delta} \\ A_y\, e^{i\delta-\frac{\pi}{2}} \end{pmatrix}$	$\frac{1}{\sqrt{2}} \begin{pmatrix} 1 \\ i \end{pmatrix}$
Elliptically polarized wave	$\begin{pmatrix} A_x\, e^{i\delta_x} \\ A_y\, e^{i\delta_y} \end{pmatrix}$	$\begin{pmatrix} cos\theta \\ sin\theta\, e^{i\delta} \end{pmatrix}$

Table 1: The polarization state of light using complex and normalized Jones vectors.

Jones Matrices		
Optical Element	θ=0	*General Case*
Ideal Polarizer	$\begin{bmatrix} 1 & 0 \\ 0 & 0 \end{bmatrix}$	$\begin{bmatrix} cos^2\theta & cos\theta \cdot sin\theta \\ cos\theta \cdot sin\theta & sin^2\theta \end{bmatrix}$
$\frac{\lambda}{4}$ with fast axis at θ^0	$\begin{bmatrix} 1 & 0 \\ 0 & -i \end{bmatrix}$	$\begin{bmatrix} cos^2\theta - isin^2\theta & cos\theta \cdot sin\theta\,(1+i) \\ cos\theta \cdot sin\theta\,(1+i) & sin^2\theta - icos^2\theta \end{bmatrix}$
$\frac{\lambda}{2}$ with fast axis at θ^0	$\begin{bmatrix} 1 & 0 \\ 0 & -1 \end{bmatrix}$	$\begin{bmatrix} cos2\theta & sin2\theta \\ sin2\theta & -cos2\theta \end{bmatrix}$
Introd. a phase delay ϕ^0, with fast axis at θ	$\begin{bmatrix} 1 & 0 \\ 0 & e^{-i\phi} \end{bmatrix}$	$\begin{bmatrix} cos^2\theta + sin^2\theta\, e^{-i\phi} & cos\theta \cdot sin\theta\,(1-e^{-i\phi}) \\ cos\theta \cdot sin\theta\,(1-e^{-i\phi}) & sin^2\theta + cos^2\theta\, e^{-i\phi} \end{bmatrix}$

Table 2: A summary of Jones matrices for the most widely used optical elements. The matrices for the general case are obtained from those for θ=0 by using rotation matrices[60].

B.2 Applying Jones matrices for the case of EO sensor

The simplest case of an EO sensor is the series of a polarizer, EO crystal and an crossed analyzer (which is a crossed polarizer). This setup is enough to produce an intensity modulation as described in section 2.5. Now the polarizer can be described with Jones matrix for $\theta = 0$ (look in Table 2 first line) while the analyzer Jones matrix is obtained from the same formula but for $\theta = 90^0$. The EO sensor can be described as a plate that introduces a phase delay Γ with the fast axis at angle θ and that Jones matrix is shown at Table 2 last line.

To find the overall matrix for an EO optical system where there is a small misalignment angle α between polarizer and analyzer (not completely crossed) we need

to multiply the following matrices:

$$\begin{bmatrix} 0 & 0 \\ 0 & 1 \end{bmatrix} \begin{bmatrix} cos\alpha & sin\alpha \\ -sin\alpha & cos\alpha \end{bmatrix} \begin{bmatrix} cos^2\theta + sin^2\theta\, e^{-i\Gamma} & cos\theta \cdot sin\theta\,(1 - e^{-i\Gamma}) \\ cos\theta \cdot sin\theta\,(1 - e^{-i\Gamma}) & sin^2\theta + cos^2\theta\, e^{-i\Gamma} \end{bmatrix} \begin{bmatrix} 1 & 0 \\ 0 & 0 \end{bmatrix}$$

The fact that the angle α and the retardation Γ is small means

$$cos\alpha \simeq 1,\ sin\alpha \simeq \alpha\ and\ e^{-i\Gamma} \simeq 1 - i\Gamma$$

and the overall matrix is:

$$\begin{bmatrix} 0 & 0 \\ 0 & 1 \end{bmatrix} \begin{bmatrix} 1 & \alpha \\ -\alpha & 1 \end{bmatrix} \begin{bmatrix} cos^2\theta + sin^2\theta\,(1 - i\Gamma) & i\Gamma\, cos\theta \cdot sin\theta \\ i\Gamma\, cos\theta \cdot sin\theta & sin^2\theta + (1 - i\Gamma)\, cos^2\theta \end{bmatrix} \begin{bmatrix} 1 & 0 \\ 0 & 0 \end{bmatrix}$$

$$= \begin{bmatrix} 0 & 0 \\ -\alpha & 1 \end{bmatrix} \begin{bmatrix} cos^2\theta + sin^2\theta\,(1 - i\Gamma) & i\Gamma\, cos\theta \cdot sin\theta \\ i\Gamma\, cos\theta \cdot sin\theta & sin^2\theta + (1 - i\Gamma)\, cos^2\theta \end{bmatrix} \begin{bmatrix} 1 & 0 \\ 0 & 0 \end{bmatrix}$$

$$= \begin{bmatrix} 0 & 0 \\ i\Gamma\, cos\theta \cdot sin\theta - \alpha + i\Gamma\alpha sin^2\theta & 1 - i\alpha\Gamma cos\theta \cdot sin\theta - i\Gamma\, cos^2\theta \end{bmatrix} \begin{bmatrix} 1 & 0 \\ 0 & 0 \end{bmatrix}$$

$$= \begin{bmatrix} 0 & 0 \\ i\Gamma\, cos\theta \cdot sin\theta - \alpha + i\Gamma\alpha sin^2\theta & 0 \end{bmatrix} \tag{B.3}$$

The polarization state of the transmitted light is computed by multiplying the vector representing the input light beam by the overall matrix (Eq. B.3). Usually the input is a linear polarized light at an angle θ with respect the axis of the crystal and final polarization state is:

$$\begin{bmatrix} 0 & 0 \\ i\Gamma\, cos\theta \cdot sin\theta - \alpha + i\Gamma\alpha sin^2\theta & 0 \end{bmatrix} \begin{bmatrix} A_x\, e^{i\delta} \\ A_y\, e^{i\delta} \end{bmatrix}$$

$$= A_x\, e^{i\delta} \begin{bmatrix} 0 \\ i\Gamma\, cos\theta \cdot sin\theta - \alpha + i\Gamma\alpha sin^2\theta \end{bmatrix} \tag{B.4}$$

The intensity of the transmitted light exiting the analyzer is:

$$I = |A_x|^2 \left[\alpha^2 + \alpha^2\,\Gamma^2\, sin^4\theta + \Gamma^2\, cos^2\theta\, sin^2\theta + 2\alpha\,\Gamma^2\, sin^3\theta\, cos\theta\right]$$

$$\Rightarrow I = I_o \left[\alpha^2 + \Gamma^2\,(\alpha^2\, sin^4\theta + cos^2\theta\, sin^2\theta + 2\alpha\, sin^3\theta\, cos\theta)\right]$$

$$\Rightarrow I = I_o \left[\alpha^2 + \Gamma^2\, sin^2\theta\,(cos\theta + \alpha\, sin\theta)^2\right] \tag{B.5}$$

For the derivation of the above equation for the transmitted light the ideal polarizer Jones matrices were used whereas in reality no such thing exists. Some light always exits the analyzer and that amount depends on the optical quality of the system known as extinction ratio σ^2. Thus another dc term has to be added to the equation above to become:

$$\Rightarrow I = I_o \left[\sigma^2 + \alpha^2 + \Gamma^2\, sin^2\theta\,(cos\theta + \alpha\, sin\theta)^2\right] \tag{B.6}$$

To check if the result presented is correct we examine the case for α=0 and we get:

$$I = I_o \left[\Gamma^2\, sin^2\theta\, cos^2\theta\right] \tag{B.7}$$

while from chapter 2, section 2.5 for the same case theory predicted (Eq. 2.16) that

$$I = I_o\, sin^2(2\theta) \cdot sin^2\frac{\Gamma}{2} \simeq I_o\,(2\, cos\theta \cdot sin\theta)^2 \cdot \left(\frac{\Gamma}{2}\right)^2$$

$$\Rightarrow I = I_o \left[\Gamma^2\, sin^2\theta \cdot cos^2\theta\right] \tag{B.8}$$

Both equations B.7 and B.8 are the same and the result presented in equation B.6 is correct.

Appendix C

Polarization Maintaining Fiber

Optical fibers are circular dielectric waveguides that can transport optical energy and information. They have a central core surrounded by a cladding with slightly lower (by ∼1%) refractive index. Since the core has a higher index of refraction than the cladding, light will be confined to the core provided that the angular condition for total internal reflection is met.

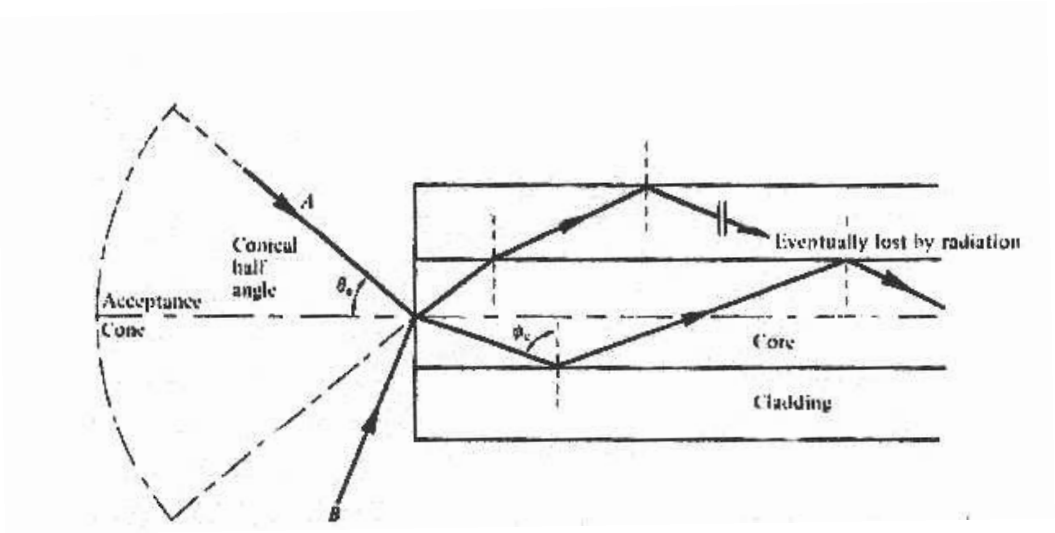

Figure 1: The acceptance angle θ_a when launching light into an optical fiber.

If the fiber core is large enough, it can support many simultaneous guided modes and this is what is called a multi-mode fiber. A mode refers to the spatial power distribution of light guided within the fiber.

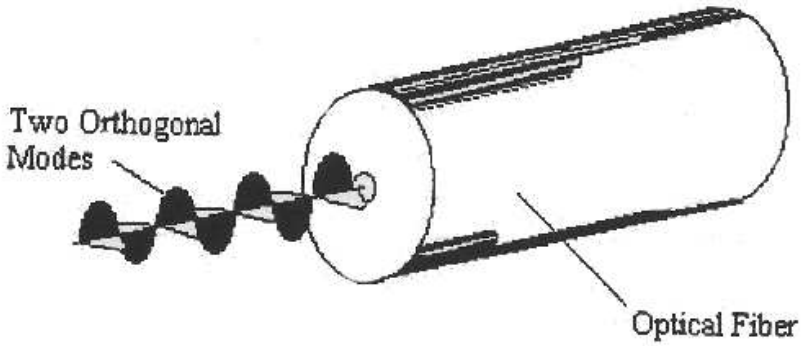

Figure 2: A mode with two orthogonal polarized components entering a fiber.

The fundamental mode which propagates in a single-mode fiber is a degenerate combination of two orthogonally polarized components as you can see in Fig. 2. In a conventional single-mode fiber, these components travel with the same velocity and so environmental disturbances, like changes in fiber position or temperature, can cause energy to couple from one component to the other, resulting a final output polarization that varies with time. To address this problem, several manufactures have developed polarization maintaining (PM) fibers. These fibers work by inducing a birefringence within the fiber core.

Birefringence means that there is a difference in the propagation constant of light traveling through the fiber for two perpendicular polarizations. This birefringence breaks the circular symmetry in an optical fiber, creating two principal transmission axes within the fiber, known respectively as the fast and slow axis of the fiber. As a result the two components travel at different velocities and so prevents the inadvertent transfer of optical power from one to the other. The higher the birefringence, the greater is this velocity difference and the more strongly will the fiber preserve polarization. Commercially available PM fibers will maintain polarization isolation

over 30dB (1000:1) between the two axes. Birefringence is created within a fiber either by forming a non-circular fiber core (shape induced birefringence) or by inducing constant stresses within the fiber with stress applying parts (stress induced birefringence) so that any external stress, within reasonable limits, would not affect the polarization. For examples of commercially available PM fibers look at Fig. 3.

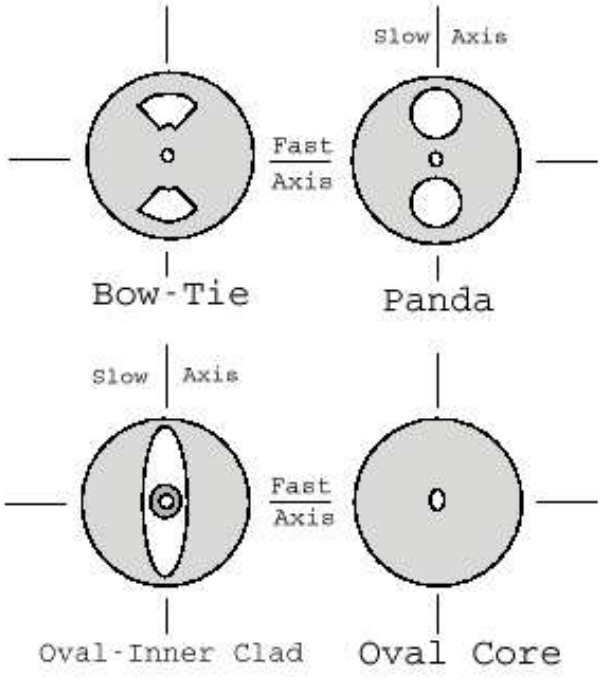

Figure 3: Examples of commercially available polarization maintaining fibers either with shape induced birefringence (Oval Core) or stress induced birefringence (Bow-Tie, Panda, Oval-inner Cladding).

Provided the input light into a PM fiber is linearly polarized and oriented along one of these two axes, then the output light from the fiber will remain linearly polarized and aligned with the principal axis even when subject to external press. How well a PM fiber maintains polarization depends on the input launch conditions into the fiber. The most important factor is the angular alignment between the polarization

axis of the light with one of the axis of the fiber.

Assume that we have a perfectly polarized input light beam into a ideal PM fiber, misaligned by an angle θ. Because of this misalignment, a small amount of light will be transmitted to the other axis and this will degrade the extinction ratio (ER) of the output beam as follows

$$ER \leq 10 \ log(tan^2\theta)$$

Under certain conditions a PM fiber can act as a polarizer so care in the design of an experiment is needed. Each single mode fiber, like the PM fiber, has a cut-off wavelength which is the shortest wavelength at which single mode propagation will occur within the fiber. Each axis of a PM fiber has a different fundamental mode cut-off wavelength. The cut-off wavelength of the fast axis is shorter than that of the slow axis. For operational wavelengths between the two cut-off wavelengths, light will be propagated by the slow axis and attenuated by the fast axis. There are available polarizing fibers that are designed to maximize this effect so they can be used as in-line polarizers.

Appendix D

Multimode Fibers

The multimode fibers have large enough core (typically $50\mu m$, but multimode fibers with core up to $600\mu m$ do exist) that when a light pulse is coupled into a multimode fiber its power is distributed among all modes. The number of modes propagated depends on the core size and numerical aperture (NA). As the core size and the NA increases the number of modes increases.

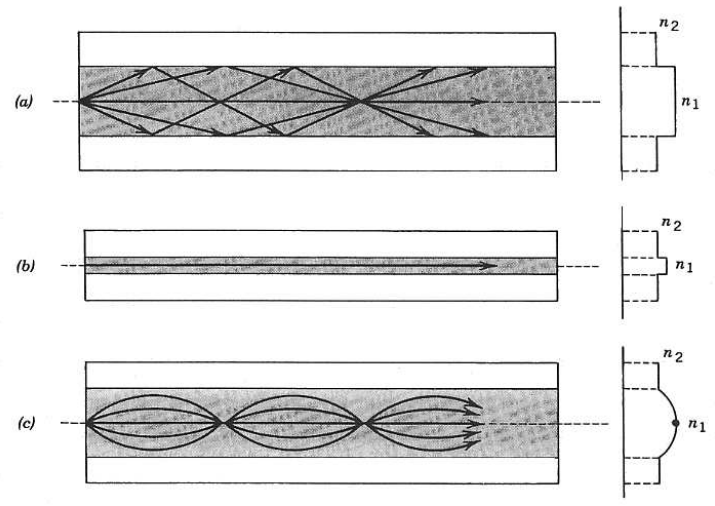

Figure 1: Geometry, refractive index profile, and typical rays in: (a) a multimode step index fiber (typical core diameter $50\mu m$), (b) a single mode fiber (typical core diameter $5\mu m$), and (c) a multimode graded index fiber (typical core diameter $50\mu m$).

As you can see in Fig. 1 besides the single mode fiber (look Fig. 1(b)) there are two kinds of multimode fibers depending on their refractive index profile. The most common one is the step index fiber which has a refractive index profile that resembles

a step and hence the name. As you can see at Fig. 1(a), each mode travels with different group velocity inside the fiber and as result when a short pulse of light

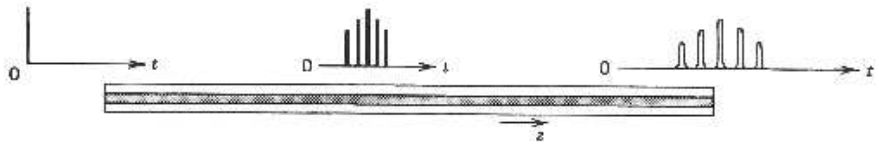

Figure 2: Pulse spreading caused by modal dispersion.

travels through this fiber its power is dispersed in time so that the pulse spreads into a wider time interval (look at Fig. 2). This phenomenon is called modal dispersion.

Another kind of multimode fiber is the graded-index fiber whose core has a variable refractive index, as you can see at Fig. 1(c), which is highest in the center and degrading gradually to its lowest value at the cladding. Thus, the group velocity of light is therefore minimum at the center and increases gradually with the radial distance. But modes (rays) at the center travel the shorter distance at the smallest group velocity and modes at big angles travel longer distances mostly in a medium where the group velocity is high. Thus, the disparities in distances are compensated by opposite disparities in group velocities. Index grating, after all, is an ingenious method for reducing the pulse spreading caused by the differences in the group velocities of the modes of a multimode fiber.

D.1 Modal Dispersion

The modal dispersion is the dominant cause of pulse spreading in multimode fibers. The difference in velocity of extreme modes determines the magnitude of

pulse spreading as follows[61]:

$$\sigma_\tau = \frac{L}{\upsilon_{g\,(min)}} - \frac{L}{\upsilon_{g\,(max)}} \tag{D.1}$$

where L is the fiber length and υ_g is the mode group velocity. For the step index multimode fibers this approximated to the following, very widely used, formula:

$$\sigma_\tau \approx \frac{n_{clad}\,\Delta}{2c}\,L \tag{D.2}$$

where c is the speed of light and Δ is the normalized index difference which is equal to

$$\Delta = \frac{n_{core}^2 - n_{clad}^2}{2\,n_{core}^2} \approx \frac{n_{core} - n_{clad}}{n_{core}} \tag{D.3}$$

The approximation in Eq. D.3, arises from assuming that n_{core} is very close in value to n_{clad} which is almost always true. For the graded index multimode fiber the approximation to the pulse spreading rate (Eq. D.1) is

$$\sigma_\tau \approx \frac{N_{core}\,\Delta^2}{4c}\,L \tag{D.4}$$

where N_{core} is the core index of refraction at r=0. It is evident that the graded index multimode fiber provides a reduction in pulse spreading rate over a step index fiber having the same Δ, by a factor of $\Delta/2$.

For a typical step index multimode fiber $\Delta = 0.01$ and $n_{clad} = 1.46$ resulting a pulse broadening rate of

$$\frac{\sigma_\tau}{L} = 24\,\frac{ns}{km} \tag{D.5}$$

while for the same fiber but graded index, the pulse broadening rate is

$$\frac{\sigma_\tau}{L} = 122\,\frac{ps}{km} \tag{D.6}$$

References

[1] D. X. Wang *et al.*, "A noninvasive bunch length monitor for femptsecond electron bunches", Appl. Phys. Lett. **70**, 529-531 (1997).

[2] P. Kung, H.Lihn, H.Wiedemann, D.Bocek, "Generation and measurement of 50-fs (rms) electron pulses", Phys. Rev. Lett. **73**, n.7, 967 (1994).

[3] Y. Shibata *et al.*, "Diagnostics of an electron beam of a linear accelerator using coherent transition radiation", Phys. Rev. E **50**, n.2, 1479 (1994).

[4] K. N. Ricci and T. I. Smith, "Longitudinal electron beam and free electron laser microbunch measurements using off-phase rf acceleration", Phys. Rev. ST Accel. Beams vol.**3**, 032801 (2000).

[5] A. H. Lumpkin *et al.*, "Optical techniques for electron-beam characterizations on the APS SASE FEL project", Nucl. Instrum. Methods Phys. Res., Sect. A **429**, 336 (1999).

[6] Q. Wu and X.-C. Zhang, "Free-space electro-optics sampling of mid-infrared pulses", Appl. Phys. Lett. **71(10)**, 1285 (1997).

[7] A. Leitenstorfer *et al.*, "Detectors and sources for ultrabroadband electro-optic sampling: Experiment and theory", Appl. Phys. Lett. **74(11)**, 1516-1518 (1999).

[8] Q. Wu and X.-C. Zhang, "Free-space electro-optic sampling of terahertz beams", Appl. Phys. Lett. **67(24)**, 3523-3525 (1995).

[9] J. A. Valdamanis, G. Mourou and C. W. Gabel, "Picosecond electro-optic sampling system", Appl. Phys. Lett. **41**, 211-212 (1982).

[10] J. A. Valdamanis, G. Mourou and C. W. Gabel, "Subpicosecond electrical sampling", IEEE Journal of Quantum Electronics, **QE-19**, 664-667 (1983).

[11] Y. K. Semertzidis, XXVII International Conference on High Energy Physics, gls0918 (1994).

[12] M. Geitz, K. Hanke, and A.C. Melissinos, "Bunch length measurements at TTFL using optical techniques", Technical report, DESY, 1997. Internal report TESLA collaboration.

[13] X. Yan *et al.*, "Subpicosecond Electro-optic Measurement of Relativistic Electron Pulses", Phys. Rev. Lett. **85(16)**, 3404-3407 (2000).

[14] Y. K. Semertzidis *et al.*, "First Electro-optical detection of charged particles", Proceedings of the PAC'99, p. 490, New York (1999).

[15] Y. K. Semertzidis *et al.*, "Electro-optical detection of charged particles", Nuclear Instruments and Methods in Physics Research **A 452(3)**, 396-400 (2000).

[16] T. Tsang *et al.*, "Electro-optical measurements of picosecond bunch length of a 45MeV electron beam", Journal of Applied Physics **89(9)**, 4921-4926 (2001).

[17] G. M. H. Knippels *et al.*, "Generation and Complete Electric-Field Characterization of Intense Ultrashort Tunable Far-Infrared Laser Pulses", Phys. Rev. Lett. **83(8)**, 1578-1581 (1999).

[18] D. Oepts *et al.*, "Picosecond electron-bunch length measurement using an electro-optic sensor", Proceed. of the 21st Intern. FEL Conference, **II-57**, DESY, Hamburg, Germany (1999).

[19] X. Yan *et al.*, "Sub-picosecond electro-optic measurement of relativistic electron pulses", Phys. Rev. Lett. **85(16)**, 3404-3407 (2000).

[20] M. J. Fitch *et al.*, "Electro-optic Measurement of the Wake Fields of a Relativistic Electron Beam", Phys. Rev. Lett. **87:034801** (2001).

[21] P. J. Channell, "Use of Kerr cells to measure RF fields", Technical report, Los Alamos National Lab, Accelerator theory note, AT-6:ATN-82-1 (1982).

[22] K. P. Leung, L. H. Yu and I. Ben-Zvi, "RF phase stabilization of RF photocathode gun through electro-optical monitoring", Proc. SPIE - Int. Soc. Opt. Eng. 2013, p. 147-153 (1993). Also BNL-49276.

[23] A. Yariv, *Quantum electronics*, 3^{rd} ed. (Wiley, New York, 1989)p.298-308.

[24] J. Kerr, Phi. Mag. **50**, 337, 446 (1875).

[25] F. Pockels, *Abhandl. Ges. Göttingen Math.-Phizik. Kl.* **39**, 1, (1894).

[26] J. F. Nye, *Physical properties of crystals, their representation by tensors and matrices*, (Oxford, Clarendon Press, 1957) p.241-243.

[27] J. F. Nye, *Physical properties of crystals, their representation by tensors and matrices*, (Oxford, Clarendon Press, 1957)

[28] I. P. Kaminow and W. D. Johnston, " Quantitative determination of sources of the electro-optic effect in $LiNbO_3$ and $LiTaO_3$", Phys. Review, **160(3)**, 519-522 (1967).

[29] U. Schlarb and K. Betzler, "Refractive indices of lithium niobate as a function of temperature, wavelength, and composotion: A generalized fit", Physical Review B **48(21)**, 15613 (1993).

[30] P. Debye and F. W. Sears, "On the scattering of light by supersonics waves", Proc. Nat. Academy of Science vol.**18**, 409-414 (1932).

[31] R. Lucas and P. Biguard, "Nouvelles proprietes optiques des liquides soumis a des ondes ultra-sonores", C. R. Acad. Sci., vol. **194**, 2132-2134 (1932).

[32] A. Korpel, *Selected papers on Acousto-Optics*, (SPIE Optical Engineering Press, Bellingham, Wash., USA, 1990)

[33] S. M. Rytow, "Ligthbeugung an ultraschallwellen", Phys. Z. Sowjetunion, vol.**8**, 626-643 (1935).

[34] W. R. Klein, B. D. Cook and W. G. Mayer, "Light diffraction by ultrasonic gratings", Acustica vol. **15**, 57-74 (1965).

[35] W. R. Klein and B. D. Cook, "Unified approach to ultrasonic light diffraction", IEEE Transactions on Sonics and Ultrasonics, vol. **SU-14(3)**, 123-134 (1967).

[36] R. Wolfe, *Applied solid state science*, (Academic Press, NY, 1972).

[37] J. Sapriel, *Acousto-Optics*, (Wiley, New York, 1979)

[38] D. F. Nelson and M. Lax, Phys. Rev. Lett. **24**, 379 (1970).

[39] Cs. Kuti, "Orientation dependence of piezoelectrically induced strain-optic response of optic axis $LiNbO_3$ samples", Journal of Modern Optics, vol. **39(12)**, 2541-2546 (1992).

[40] Bajak I.L. *et al.*, "Attenuation of acoustic waves in lithium niobate", J. Acoust. Soc. Am. **69(3)**, 689-695 (March 1981).

[41] R. Weil and D. Halido, "Resonant piezoelectro-optic light modulation", J. Appl. Phys., vol. **45**, 2258-2265 (1974).

[42] Cs. Kuti *et al.*, "High-efficiency diffraction modulation of light by strain-optic effect of piezoelectrically induced standing acoustic waves in bulk $LiNbO_3$ crystal", Microwave and Optical Technology Letters, vol. **3(6)**, 193-195 (1990).

[43] L. Turi *et al.*, "Piezoelectrically induced diffraction modulation of light", IEEE Journal of Quantum Electronics, vol. **26(7)**, 1234-1240 (1990).

[44] R. W. Dixon, "Acoustic diffraction of light in anisotropic media", IEEE J. Quantum Electron. **QE-3(2)**, 85-93 (1967).

[45] V. I. Balakshy and J. A. Hassan, "Polarization effects in acousto-optic interaction", Optical Engineering, vol. **32(4)**, 746-751 (1993).

[46] R. Wolfe, "Applied solid state science:Advances in materials and device research", vol. 3, 148-153 (Academic Press, NY, 1972).

[47] P. Kwiek and R. Reibold, "Light diffraction by ultrasonic-waves for normal and Bragg incidence", Acustica, vol. **77(4)**, 193-200 (1992).

[48] A. Koprel *et al.*, "Bragg diffraction sampling of a sound field", J. Acoustical Society of America, vol. **51(5)**, 1582-1592 (1972).

[49] J. D. Jackson *Classical Electrodynamics*, 3^{rd} ed. (Wiley, New York, 1999)p.560-561.

[50] P. R. Bevington *Data Reduction and Error Analysis for the Physical Sciences*, 2^{nd} ed. (WCB/McGraw-Hill, USA, 1992) p.198-201.

[51] P. R. Bevington *Data Reduction and Error Analysis for the Physical Sciences*, 2^{nd} ed. (WCB/McGraw-Hill, USA, 1992) p.258-259.

[52] E. W. Taylor, "Geminate recombination behaviour of a X-ray irradiated single-mode $LiNbO_3$:Ti waveguide operating at 1300nm", J. Opt. Commun. **9**, 64 (1988).

[53] A. Neyer, "Integrated-optic devices in lithium niobate: Technology and applications", SPIE Vol. 1274 *Electro-Optic and Magneto-optic materials II* page 2 (1990). TA1750.E26x.1990

[54] S. Yamada and M. Minakata, "DC drift phenomena in $LiNbO_3$ optical waveguide devices", Jap. Journal of Appl. Phys.**20(4)**, 733-737 (1981).

[55] Bill Cieslak, private communation, Hamamatsu Corp., 03/30/00.

[56] H. Kogeluik and T. Li, Proc. IEEE **54**, 1312 (1966).

[57] Y. Giomataris *et al.*, " MICROMEGAS: a high-granularity position-sensitive gaseous detector for high particle-flux enviroments", Nuc. Instr. Meth. **A376(1)**, 29-35 (1996).

[58] A. Yariv and P. Yeh, *Optical waves in crystals*, (Wiley, New York, 1984)p.121-154.

[59] R. C. Jones, "New calculus for the treatment of optical systems", Journal of Opt. Soc. Am. **31**, 488 (1941).

[60] Y. K. Semertzidis, "Coherent production of light pseudoscalars (axions) inside a magnetic field with a polarized laser beam", Ph.D Thesis, Rochester, NY (1990).

[61] J. A. Buck, *Fundamentals of optical fibers*, (Wiley, New York, 1995)p.122-164.